공학박사학위논문

Solution-Processable Li and Na Superionic Conductors for All-Solid-State Batteries

용액공정이 가능한 리튬 및 소듐 고체전해질을 이용한 전고체전지

2017년 2월

서울대학교 대학원

화학생물공학부

박 건 호

ABSTRACT

Solution-Processable Li and Na Superionic Conductors for All-Solid-State Batteries

Kern Ho Park

Department of Chemical and Biological Engineering

The Graduated School

Seoul National University

Bulk-type all-solid-state lithium batteries using sulfide solid electrolytes are considered a very promising solution for tackling the safety challenges associated with conventional lithium-ion batteries. However, further development of solid electrolytes is imperative in order to improve their ionic contacts with active materials, conductivity, scalability of synthesis protocols, and air-stability. A solution-based synthesis process can provide a breakthrough in the architecture and fabrication of composite structures. This study show that a new, highly conductive (4.1×10^{-4} S cm^{-1} at 30^{o}C), highly ductile, and dry-air-stable glass $0.4LiI\text{-}0.6Li_4SnS_4$ is prepared at 200^{o}C using a scalable method that employs a homogeneous methanol solution. Comprehensive diagnostic analyses reveal that lowering the crystallinity and

incorporating large and highly polarizable iodide ions into Li_4SnS_4 improve the ductility and conductivity. Importantly, the solution process enables the wetting of any exposed surface of the active materials with highly conductive solidified electrolytes ($0.4LiI\text{-}0.6Li_4SnS_4$), resulting in considerable improvements in electrochemical performances of these electrodes over conventional mixture electrodes.

Even though sodium-ion batteries (NIBs), which is another important class of battery type, have been developed extensively due to the advantage of low cost, development of all-solid-state Na batteries (ASNBs) has remained challenging because of relatively low ionic conductivity of Na-ion conductor. Na_3SbS_4 show high conductivity of 1.1×10^{-3} S cm^{-1} which is one of the most promising result so far. Furthermore it remain its structure after dissolving to water or methanol with moderate ionic conductivities. Consequently, sodium-ion conductive coating layers were casted to active material successfully. The results hold great promise for practical all-solid-state technology as well as provide insights into discovering broad classes of solution-processable superionic conductors.

Keywords: Ionic conductor, All-solid-state batteries, Solid electrolyte, Solution Process

Li-ion batteries, Na-ion batteries

Student Number: 2011-22916

Table of Contents

LIST OF FIGURES

LIST OF TABLES

1. INTRODUCTION

Since Sony Corporation commercialized the first products featuring lithium-ion batteries (LIBs) in the early 1990s,[1] LIBs have begun to emerge as the most promising power source for portable electronic devices.[2-5] The most important advantage of LIBs is their high energy density, which originates from their high voltage of ~4 V.[2-5] Since the electrochemical window typical of aqueous liquid electrolytes (LEs) impedes LIBs reaching such a high voltage, the development of organic LEs was the basis of the success of the LIB.[2-5] The state-of-the-art organic LEs consist of a lithium salt, such as $LiPF_6$, dissolved in a mixture of linear and cyclic alkyl carbonates, exhibiting an ionic conductivity of ~10^{-2} S cm^{-1} at room temperature (RT).[2,5] However, the intrinsic nature of organic LEs poses serious safety concerns regarding their flammability and possible leakages.[2-8] The safety of LIBs is of prime concern because they are considered a potential candidate for large-scale energy storage applications in devices such as electric vehicles (EVs) and energy storage systems. [2-9] All-solid-state lithium batteries (ASLBs) using inorganic solid electrolytes (SE) are considered as an ideal alternative to ultimately realize safe LIBs.[6,9] Their broad operating temperature range is also an important benefit from the point of view of energy storage applications (ESS).[8,10-12] Additionally, SEs offer two significant advantages over LEs. First, only the cation, Li^+ is mobile. Thus, its transport number is 1. Second, Li^+ ions at the electrode/SE interface are not subject

to de-solvation, with positive effects on the charge transport, which explains the appreciable amount of activation energy and the related kinetic properties typical of LE cells.[5,13,14] Considering these two features, it is reasonable that batteries using SEs may outperform batteries using LEs, if the ionic conductivity is the same.[14]

Thin film ASLBs using LiPON ($Li_{3.3}PO_{3.9}B_{0.17}$) as the SE are well-known commercialized batteries showing excellent performance.[15,16] However, the use of thin film ASLBs is restricted to small-scale applications, such as smart cards and microelectronic devices, due to the highly expensive vacuum deposition process required for their fabrication.[15-17] Recently great attention has been paid to a bulk-type (or composite-type) ASLB suitable not only for portable electronic devices, but also for large-scale applications.[6,9,18] A critical feature of the bulk-type ASLB is its composite electrode structure, in which the active materials, SE powders, and the conductive materials, such as carbon, exist as particulate mixtures. Bulk-type ASLBs do not need any expensive vacuum deposition process to be fabricated, which is promising for large-scale applications. In the bulk-type ASLBs, SE particles replace the LE typical of conventional LIBs. The thick composite-structured electrode in the bulk-type ASLBs is an indication their energy density can be increased, thus making them compete with conventional LIBs. However, this requires highly conductive SEs which exhibit ionic conductivity comparable to that of LES (~10^{-2} S cm^{-1} at RT).

To date, many SEs with conductivities over 10^{-4}-10^{-3} S cm^{-1} at RT have been developed.[6,9,19-26] Among the materials suitable to be used as SEs, oxides [24-26] and sulfides[6,9,19-22] have been extensively investigated for ASLBs.

The perovskite-structured $Li_{3x}La_{2/3-2x}\square_{1/3-2x}TiO_3$ ($0<x<0.16$) (LLT),[24] the NASICON-structured $Li_{1.3}Al_{0.3}Ti_{1.7}(PO_4)_3$[25] and the garnet-structured $Li_7La_3Zr_2O_{12}$ (LLZ)[26] are the most famous oxides used as SE materials. They exhibit conductivities in the range of 10^{-4}-10^{-3} S cm^{-1} at RT, which is acceptable for bulk-type ASLBs, although not ideal. They can be handled in an atmospheric environment, which is another advantage. However, their brittleness poses a critical restriction for the fabrication of bulk-type ASLBs.[18,27,28] Cold pressing of a mixture of active materials with a selected oxide as the SE is not enough to form the favorable two-dimensional contacts necessary for an effective Li^+ ionic conduction throughout the three-dimensional composite electrode structure.[18,27,28] Instead, a sintering process at elevated temperature is necessary.[27,28] This kind of heat treatment generates unwanted interfacial reaction, resulting in the failure of bulk-type ASLBs using one of these oxides as the SE during operations.[27,28] However, several exceptions exist. ASLBs with the phosphate-based material, $Li_3V_2(PO_4)_3$, used as the electrode, and the phosphate-based material, $Li_{1.5}Al_{0.5}Ge_{1.5}(PO_4)_3$, used as the SE by sintering via the spark plasma method, gave a performance of ~100 mAh (g of $Li_3V_2(PO_4)_3)^{-1}$.[29] The addition of Li_3BO_3 and Al_2O_3 to Ca- and Nb-doped LLZ could reduce the sintering temperature to 790°C and the $LiCoO_2$/Li battery could work.[30] However, the cycle test for the $Li_3V_2(PO_4)_3$ ALB was conducted at a very low C-rate (C/20-C/40) at the temperature of 80°C.[27,28] Also, the $LiCoO_2$ ASLB using the Ca- and Nb-doped LLZ

sintered with Li_3BO_3 and Al_2O_3 showed a very low discharge capacity of 78 mAh g^{-1} at very low C-rate (~C/100).[30]

The most important advantage of sulfide SEs over oxide SEs is that the former can be easily deformed, simply by cold pressing[7,18] The research group of Tatsumisago reported that Li_2S-P_2S_5 SE materials display Young's moduli between the one typical of oxide ceramics and the one typical of organic polymers.[18] The unwanted interfacial reaction between the electrode materials and the SEs occurring during the fabrication process, may consequently be avoided. This encourages a more extensive investigation on sulfide SEs for ASLBs.[7,10-12]

Most efforts on the development of SEs thus far have placed a strong emphasis on the high ionic conductivity of the SEs.[6,9,20,31,32] However, there is a huge discrepancy between the high ionic conductivities of sulfide SEs and the below-par performance of bulk-type ASLBs,[33-35] which originates from the limited ionic contact between the active materials and SEs.[6,7,33,36] For example, cold-pressed composite electrodes have exhibited porosities as high as 20-30%, reflecting poor surface coverage of SEs on the active materials.[35] Therefore, the fabrication of composite electrodes with more intimate ionic contacts should be a prime objective for future development.[18,33,35] However, this development has been inhibited by the drawbacks associated with the conventional protocols of synthesizing sulfide SEs, such as solid-state reactions[6,31] and mechanochemical methods.[9,20]

An alternative architecture of SEs for composite electrodes was demonstrated by depositing a SE ($80Li_2S$-$20P_2S_5$) thin film on active materials by pulsed laser

deposition.[18,37] In theory, direct SE coating on active materials can solve the problem of poor ionic contact in bulk-type ASLBs, thus increasing the power and energy densities at the electrode and cell levels.[37,38] However, the vacuum deposition method might be prohibitive for commercialization. In contrast, a scalable solution-based coating method could provide the necessary breakthrough for developing better sulfide SEs and ASLBs. It was reported that Thio-LISICON ($Li_{3.25}Ge_{0.25}P_{0.75}S_4$) showing 1.82×10^{-4} S cm^{-1} can be prepared by using anhydrous hydrazine.[39] However, the use of extremely dangerous anhydrous hydrazine excludes interests for further development. Liang and co-workers reported the synthesis of β-Li_3PS_4 with an ionic conductivity of 1.6×10^{-4} S cm^{-1} by using tetrahydrofuran[40] and $Li_7P_2S_8I$ with an ionic conductivity of 6.3×10^{-4} S cm^{-1} by using acetonitrile.[41] In both cases, however, the solutions are neither homogeneous nor environmentally friendly. The Tatsumisago group reported that N-methylformamide (b.p. = 182.6°C) can dissolve Li_3PS_4 (LPS) to form a homogeneous solution, and LPS with a conductivity of 2.6×10^{-6} S cm^{-1} can be recrystallized.[42] The same group later showed that argyrodite Li_6PS_5Cl with an ionic conductivity of 1.4×10^{-5} S cm^{-1} can be prepared by using ethanol.[43] It is also worth mentioning that Li_4SnS_4 with an ionic conductivity of 7×10^{-5} S cm^{-1} was prepared at 320°C from aqueous solution, where water was used to obtain a high-purity crystalline phase.[44] A major challenge in developing solution-processable sulfide SEs is the simultaneous fulfillment of all the following requirements: forming a homogeneous solution for the coatable process, using nontoxic and safe solvents with low boiling points, and ensuring sufficiently high

ionic conductivities (>10^{-4} S cm^{-1}). Another critical issue regarding sulfide SEs is their instability in air.[45] As substituted Li_4SnS_4 exhibiting stability in air and high conductivity (1.39×10^{-3} S cm^{-1}) was recently prepared by a solid-state reaction at 450°C.[22] However, the application of this SE may be hindered owing to the use of arsenic, which is extremely toxic.

In other hands, sodium-ion batteries (NIBs) could be more competitive for a large-scale application such as energy storage system (ESS) for efficient electric grid than LIBs.[3,46-48] Moreover, solidification of electrolytes in batteries avoids serious safety which is essential issue to guarantee the reliability of ESS. In this regard, all-solid-state sodium-ion batteries (ASNBs) are good candidates for use in ESS.[7] However, the development of ASNBs was remains challenging in two aspects. First, relatively low ionic conductivity of sodium ionic conductor compare to that of lithium ionic conductor. The search for sulfide sodium superionic conductors was initiated by the development of cubic Na_3PS_4 (NPS), which showed a conductivity of 4.6×10^{-4} S cm^{-1}, a value that is much higher than that of the tetragonal phase.[7,49] By forming a solid solution with Na_4SiS_4 ($94Na_3PS_4$-$6Na_4SiS_4$), the conductivity of NPS was further increased to 7.4×10^{-4} S cm^{-1}.[50] An even higher conductivity of 1.16×10^{-3} S cm^{-1} was achieved by replacing sulfur in NPS with selenium (Na_3PSe_4). This enhancement is explained by lattice expansion while retaining the same cubic structure and the presence of highly polarizable selenium.[51] It was anticipated that Na_3SbS_4 might also show high conductivity considering the similar size of SbS_4^{3-} with respect to PSe_4^{3-}.[52] Very recently, another type of sodium-ion conductor was reported, $Na_{10}SnP_2S_{12}$, which

showed a conductivity of 4.0×10^{-4} S cm^{-1}.[53] Overall, only a few sulfide sodium-ion SEs have been developed. Thus, there is much room for further improvement in composition and structure by design of materials. Furthermore, no solution processable sulfide sodium-ion SE materials are known, which is related to the unavailability of solvents that can dissolve SEs without irreversible or side reaction.[35]

Consequently, the highly ionic conductive SEs, especially, which can be formed through solution casting process are desirable to achieve breakthrough for a high performance all-solid-state lithium or sodium batteries. The air-stability is another requirement for easier handling. Herein, new class of superionic conductors based on tin or antimony were investigated to fulfill these commitment.

2. BACKGROUND

2.1. Basic Principles of Electrochemical Cells

The charge separation arise at the interface of electrode and electrolytes when it immersed in. Electric field introduced is determined by followed relation.

$$\mathrm{E} = \frac{\mathrm{F}}{\mathrm{q}} = \frac{q}{4\pi\varepsilon\varepsilon_0 r^2}$$

Here, q is a charge of an electron (1.6×10-19 C), ε is a dielectric constant, ε_0 is dielectric constant at vacuum (8.85×10^{-19} C^2 N^{-1} m^{-2}), and r is a distance of charge separation. The magnitude of electric field is 2×10^7 V m^{-1} assuming r is 1 nm, thus, the potential difference is 20 mV. Considering this value comes from unit charge, relatively huge potential difference arise from very little amount of charge separation.

Electrode potential during electrochemical reaction can be measured using reference electrode. In principle, the reference electrode have to be ideal non-polarizable electrode whose electric potential does not change with current flow due to negligible charge transfer resistance, R_{ct}. For example, NHE (Normal Hydrogen Electrode), SCE (Saturated Calomel electrode, $Hg/Hg_2Cl_2(s)$, KCl (4.2 *M*, saturated)) for aqueous electrolyte, and $Pt/FeCp_2$, Ag/Ag^+ electrode for non-aqueous electrolyte can be used as a reference electrode.

The standard electromotive force (*emf*, E^0_{cell}) of the electrochemical cell with two half-cell is,

$$E^0_{cell} = E^0_{RHS} - E^0_{LHS}, \Delta G^0 = -nFE^0_{cell}$$

where E^0_{RHS} is the standard electrode potential with higher standard reduction potential and E^0_{LHS} is with lower.

The emf of galvanic cells with infinite of combination could be determined using prior relation. For example, the cells with copper and zinc can be constructed.

$$Zn^{2+} + 2e \rightarrow Zn, E^0_{RHS} = 0.34\ V\ (vs.\ NHE)$$
$$Cu^{2+} + 2e \rightarrow Cu, E^0_{RHS} = -0.76\ V\ (vs.\ NHE)$$

The emf of cell is calculated to 1.1 V (0.34-(-0.76) V). However, the concentration of ions vary continuously with current, which affects emf.

$$E^c_{eq} = E^0_{Cu/Cu^{2+}} + \frac{RT}{2F} \ln a_{Cu^{2+}}$$
$$E^a_{eq} = E^0_{Zn/Zn^{2+}} + \frac{RT}{2F} \ln a_{Zn^{2+}}$$
$$E_{cell} = E^c_{eq} - E^a_{eq} = \left(E^0_{Cu/Cu^{2+}} - E^0_{Zn/Zn^{2+}}\right) + \frac{RT}{2F} \ln \frac{a_{Cu^{2+}}}{a_{Zn^{2+}}}$$

Discharging the cell, the concentration of Zn^{2+} is increasing and Cu^{2+} is decreasing respectively. Therefore, the emf of cell decline.

The experimental value of working voltage (E_{wk}) is affected by not only thermodynamically determined E^0_{cell} but also kinetic parameter such as the voltage drop of electrode.

$$E_{\mathrm{wk}} = E_{\mathrm{cell}} - \eta_{\mathrm{a}} - \eta_{\mathrm{c}} - iR_{\mathrm{total}}$$

η_{a} and η_{c} come from kinetically induced overpotential in the electrodes. R_{total} is total resistance of other components such as electrolyte, separator and electric wire. In short, both thermodynamics (E_{cell}) and kinetics affect the working voltage.

2.2. Overview of Bulk-type Inorganic All-solid-state Batteries

2.2.1. Conductivity of Ionic Conductor

The high ionic conductivity of SEs, compared with that of LEs (~10^{-2} S cm^{-1}), is the prerequisite for the employment of high-energy ASLBs at ambient temperature. The main constraints on the material design of SEs can be summarized as follows. First, the larger and the more polarizable the ions, the more preferable they are for achieving higher ionic conductivity.[19] It is known as a general trend that the isovalent substitution of oxygen with the larger and more polarizable sulfur tends to increase the conductivity of the compound.[19] Second, the creation of an interfacial vacancy caused by aliovalent substitution can strongly affect the ionic conductivity.[19] In 2001, Kanno and co-workers reported the thio-lithium superionic conductor (thio-LISICON, $Li_{3.25}Ge_{0.25}P_{0.75}S_4$), which was the first crystalline ionic conductor having a high ionic conductivity (2.2×10^{-3} Scm^{-1} at 25°C) and a high decomposition potential.[19] Recently, the same group published a work on $Li_{10}GeP_2S_{12}$ (LGPS, 1.2×10^{-2} S cm^{-1} at RT).[6] Even though thio-LISICON and LGPS do not present an identical structure, both are based on the concept of aliovalent substitution: both have the same chemical formula, $Li_{4-x}Ge_{1-x}P_xS_4$, with x=3/4 for thio-LISICON and x=2/3 for LGPS. The extremely high conductivity of LGPS triggered an explosion of interest in this field. The *ab initio* calculation of LGPS by Ceder and co-workers claimed ionic conductivities of 4×10^{-2} S

cm^{-1} in the c-direction and 9×10^{-4} S cm^{-1} in the ab plane.[54] The calculated overall conductivity[54] of 9×10^{-3} S cm^{-1} agrees well with the experimental value (1.2×10^{-2} S cm^{-1}).[6] This result suggests that the ionic conduction in LGPS occurs in three dimensions, rather than in one dimensions. The isotropy of ionic conduction in LGPS was also confirmed by the structure investigation performed using single-crystal X-ray analysis.[55] The theoretical approach for the $Li_{10\pm1}MP_2X_{12}$ family (where M=Ge, Si, Sn, Al, or P, and X=O, S, or Se) anticipated that the isovalent substitution of germanium into cheaper elements, including silicon or tin, would have small effects on the ionic conductivity of the compound.[56] The high conductivity of 4×10^{-3} S cm^{-1} at 27°C, obtained experimentally using $Li_{10}SnP_2S_{12}$, is in line with the aforementioned theoretical calculations.[57] The aliovalent substitution of tin with arsenic in Li_4SnS_4[44] to give $Li_{4-x}Sn_{1-x}As_xS_4$, where x=0.125, was also demonstrated to significantly increase the conductivity of the compound from 7.1×10^{-5} S cm^{-1} to 1.39×10^{-3} S cm^{-1} at 25°C.[22]

$Li_2S{\cdot}P_2S_5$ glass-ceramics are another important class among the sulfides used for SEs. Crystallization of $Li_2S{\cdot}P_2S_5$ glassy powders at elevated temperatures improved the conductivities of the obtained compounds, giving values of $\sim10^{-3}$ S cm^{-1}.[20,58-63] The glass-ceramic powders were obtained by the heat treatment of glassy powders prepared from mechanical milling or melt-quenching methods.[20,58,59,61,62,64] The compound $xLi_2S{\cdot}(100\text{-}x)P_2S_5$ with x=70.0-80.0 has been extensively studied.[20,58,59,61,62,64] Particularly stoichiometric $Li_7P_3S_{11}$ (or $70Li_2S{\cdot}30P_2S_5$) and

Li_7PS_{11-z} exhibited the highest conductivities at 25°C: 4.2×10^{-3} S cm^{-1} and 5.4×10^{-3} S cm^{-1}, respectively.[62,63] It should be noted that the contribution to the resistance given by the grain boundaries becomes more important for highly conductive materials. Recently, the conductivity of $Li_7P_3S_{11}$ was measured after optimizing the heat treatment of the SE pellet, so that the grain boundary resistance could be minimized by densitification, allowing the conductivity to reach 1.7×10^{-2} S cm^{-1} at RT, a value even higher than that of LGPS (1.2×10^{-2} S cm^{-1}).[9] Glass-ceramic SEs doped by germanium were also studied.[65] Advantages of the glass-ceramic SEs over the crystalline ones might include their relatively lower heat-treatment temperature. Crystallization of glassy sulfides occurs at ~200-300°C, which is, in turn, the temperature for preparation of the glass-ceramic SEs.[20,58,59,61,62,64] In contrast, the crystalline SEs are prepared at ~450-600°C.[6,19,22,31,57,66,67]

Glassy sulfides were studied extensively before the crystalline (e.g., thio-LISICON and LGPS) and glass-ceramic materials were reported. Glassy sulfides for SEs include $Li_2S{\cdot}P_2S_5$,[68] $Li_2S{\cdot}SiS_2{\cdot}Li_3N$,[69] $Li_2S{\cdot}P_2S_5{\cdot}LiI$,[70] $Li_2S{\cdot}SiS_2{\cdot}LiI$,[71,72] $Li_2S{\cdot}SiS_2{\cdot}Li_xMO_y$,[73] $Li_2S{\cdot}GeS_2$,[74] and $Li_2S{\cdot}B_{2[19]}S_3{\cdot}LiI$,[75] all exhibiting conductivities in the range of ~10^{-4}-10^{-3} S cm^{-1} at RT.

2.2.2. Electrochemical stability of Solid Electrolytes

It is well known that the electrochemical stability of LEs plays a main role in the performance, such as durability, rate capability, and safety, of the LIBs.[2-5] The

importance of the electrolyte electrochemical stability is high, and is therefore also desired in the case of SEs. For example, even though Li_3N exhibits a high ionic conductivity of 10^{-3} S cm^{-1}, its low decomposition potential of ~0.4 V (*vs*. Li/Li^+) impedes its employment in ASLBs.[8] Another example is given by the oxide SEs. The perovskite structured LLT undergoes decomposition is contact with metallic lithium because Ti^{4+} cations are reduced to Ti^{3+}.[24] However, the invention of LLZ, with fixed-valent zirconium in place of titanium, solved this problem.[26]

Although it is not yet well known, sulfide SEs also have limited electrochemical windows. Theoretical calculations carried out for the $Li_{10\pm1}MP_2X_{12}$ family (where M=Ge, Si, Sn, Al, or P, and X=O, S, or Se) provide an insight on the electrochemical stability of various materials used for SEs.[56] The band gap of LGPS was calculated to be 3.6 eV, suggesting a relatively narrow electrochemical window.[56] Germanium in LGPS is believed to be reduced at a low potential,[76] similar to titanium in LLT.[24] Li_2S and P_2S_5 are expected to be formed as a result of decomposition.[56] Recently, Jung and co-workers confirmed that the structure of LGPS is altered even at 0.6 V (*vs*. Li/Li^+), most likely forming an Li_2S phase, which explains the significant degradation in the performance of TiS_2/LGPS/Li-In solid-state batteries.[76] The $Li_2S{\cdot}P_2S_5$-based SEs turned out to be more stable at low voltages than the LGPS-based SEs, as shown in Figure 1. At positive voltage ranges, the onset voltage triggering the oxidative decomposition is ~3.0 V (vs. Li/Li^+).[77-79]

Even though the restricted electrochemical stability can degrade the performance of ASLBs, the electrochemical window itself does not directly limit the operating voltage

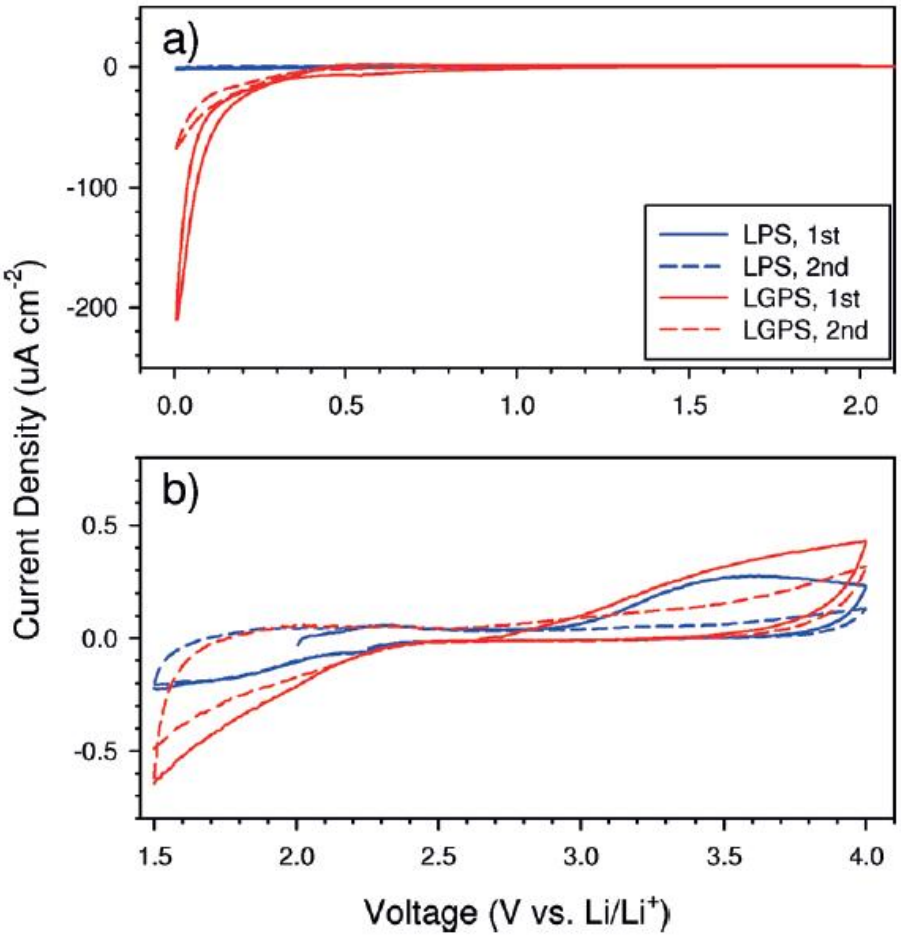

Figure 1. Cyclic voltammograms of Ti/Li_3PS_4/Li-In and Ti/LGPS/Li-In cells: a) in the negative potential range; and b) in the positive potential range.

range of ASLBs. Graphite has been successfully employed in LIBs, in spite of the decomposition of LEs occurring at <1 V (*vs*. Li/Li^+).[2] In addition to the intrinsic electrochemical stability of the electrolytes, a favorable passivation is important, because it may suppress the continuous process of decomposition.[2] In this context, the engineering of the interface between the active material and the SE is a critical issue in ASLBs.

2.2.3. Electrode Materials for ASSLBs

The success of state-of-the-art LIBs may be attributed not only to the use of suitable electrode materials, but also to the carbonate-based LEs, with their kinetically wide electrochemical windows and their excellent compatibility with the electrode materials.[2-5] For example, fully reversible intercalation-de-intercalation in $LiVS_2$ became possible when using the electrolyte which is commonly used nowadays, 1 *M* $LiPF_6$ in ethyl carbonate:diethyl carbonate (1:1 vol. ratio), whereas the traditional electrolyte used for the studies performed in the 1970s, 1*M* $LiClO_4$ in propylene carbonate, had a detrimental effect on the performance of $LiVS_2$.[80,81] Understanding the phenomena taking place at the interface between the sulfide SEs and the electrode materials is crucial. In addition, new opportunities may arise to reinvestigate the compatibility of already known or innovative electrode materials with the sulfide SEs.

2.2.3.1. Lithium Metal

Lithium metal is supposed to be an ideal anode for all types of lithium secondary batteries, including alternative batteries such as Li-S and Li-air batteries, because of its high theoretical capacity (3862 mAh g^{-1}), the lowest operating potential among all the known anode materials, its metallic nature,, and the fact that it avoids the use of pre-lithiated cathode materials.[82,83] However, a severe safety concern, associated with eventual internal short circuits caused by the dendritic growth of lithium during repeated deposition and dissolution cycles, brought the ban of lithium metal in commercially available LIBs.[84] The ASLB, which is free from flammable components, can take advantage of the use of lithium metal as the anode, maximizing its energy density.

Two issues, however, must be addressed. First, ASLBs also suffer from the internal short circuits caused by abnormal lithium growth. In the experiments carried out using the $Li_2S{\cdot}P_2S_5$ SE pellet shown.[85] It was observed that lithium metal tends to grow in the voids and along the grain boundaries of the SE pellet.[85] Second, the chemical stability of the SEs in contact with lithium metal can be affected by its composition. Jung and co-workers reported that the structure of LGPS is severely altered at low voltage ranges, likely generating a Li_2S phase.[76] The poor chemical stability of the SE in contact with lithium was also found in the As-doped Li_4SnS_4, in which tin acts as a reducing center.[22] Despite of many efforts[22,86] enabling the use of lithium metal as the anode will remain a challenge until significant developments of composition, surface modification, and pelletized microstructure of SEs are made.

2.2.3.2. Lithium Metal Oxide

As for the conventional LIBs using LEs, the layered or spinel Li_xMO_2 (M=Co, Ni, Mn) cathode materials are considered as viable candidates for ASLBs because of their highly reversible intercalation-deintercalation reaction with low dimensional change and high operating potential. To date, many Li_xMO_2 materials, including $LiCoO_2$,[6,10,18,36,66,78,79,86,87] $Li[Ni,Mn,Co]O_2$,[88-91] and $LiMn_2O_4$,[92] have been tested in ASLBs using sulfide SEs. However, the bare Li_xMO_2 showed much lower capacity than the theoretical one, a large amount of irreversible reaction during charging, and a high overpotential.[93] The poor performance of Li_xMO_2 originate from the intrinsically low oxidation onset potential (~3 V *vs*. Li/Li^+) of the sulfide SEs,[77-79] as confirmed by the abnormal sloping plateau starting at ~2.3-2.4 V (*vs*. Li-In).[93] It was observed that the elements originally found in $LiCoO_2$ and $Li_2S{\cdot}P_2S_5$ SE mutually diffuse.[10] The formation of a new interfacial layer, mainly consisting of cobalt and sulfur, was suggested to be the cause of the poor performance.[10]

As already reported by numerous publications regarding oxide cathodes for LIBs containing LEs.[78,79,94-96] surface coating made using various metal oxides, such as $LiNbO_3$,[6,97] $Li_4Ti_5O_{12}$,[36] Li_2SiO_3,[78] Al_2O_3,[98] and $BaTiO_3$,[99] when applied on Li_xMO_2, turned out to be effective for significantly reducing the interfacial resistance in ASLBs, thereby improving their electrochemical performance.[10] The mechanism underlying the observed enhancement can be either the suppression of chemical reactions between the sulfide and the oxide layers, or the shielding effect

provided by the oxide coating against the noble potential of the Li_xMO_2 cathodes.[36,92,97,99-101] It should be emphasized that typically, the coatings with electron-insulating and ion-conducting oxide materials resulted in improvement of performance.[36,92,97,99-101] Enhanced performance of $LiCoO_2$ by electronically conductive coatings with metal sulfides, such as NiS and CoS, were also reported.[102] Ionic conductivity can be achieved by using coating materials that include lithium.[6,36,78,97] However, a good ionic conductivity was also found in a lithium-free tantalum oxide, in which openings in the crystal structure were large enough for Li ions to pass through.[103]

2.2.3.3. Reinvestigated or New Electrode Materials

ASLBs provide a new opportunity to investigate, under a different perspective, electrode materials that were found inappropriate or simply not good enough for conventional LIBs. Lithium intercalation-deintercalation in the layered transition metal chalcogenides was extensively investigated in the early 1970s.[4,104] However, transition metal chalcogenides were abandoned after the emergence of Li_xMO_2, which is lighter and allows operation at higher voltages than sulfides.[2,4] However, the transition metal sulfides may be revisited for ASLBs because of their mild operating voltages (~2-3 V *vs*. Li/Li^+) and potentially good compatibility between different types of sulfides, creating an effective interface.[77,105] In particular TiS_2[105,106] and Li_xTiS_2[107,108] were reported to show good cycling performance in ASLBs, with reversible capacities close to the theoretical one. The Chevrel-phase compound,

$(Cu_x)Mo_6S_{8-y}$, also exhibited excellent cycle life in ASLBs.[11,12] The outstanding performance of TiS_2 and $(Cu_x)Mo_6S_{8-y}$ is associated with their metallic nature, their reversible intercalation/deintercalation, high Li^+ ion diffusivity, and so on.[11,105,106] Lee and co-workers investigated the electrochemical reactivity of pyrite FeS_2 in ASLBs.[109] In the LE cells, FeS_2 exhibited an initial capacity of ~500 mAh g^{-1} at 30°C and a rapid capacity fading.[109] Its performance became even worse at 60°C. The poor performance of FeS_2 is associated with the dissolution of intermediate polysulfide products into the LEs.[109] In sharp contrast, FeS_2 with a sulfide SE reacts reversibly with lithium, showing excellent cycleability. Jung and co-workers reported that $LiTi_2(PS_4)_3$ worked much better in ASLBs than in cells featuring a LE.[77] The poorer performance shown by $LiTi_2(PS_4)_3$ in the previous reports[110] were associated with its dissolution into the LE.[2,77] The amorphous titanium polysulfide prepared by a mechanochemical method is promising for ASLBs, contrary to what was found in the case of LE cells.[111] The aforementioned materials present no only large capacities, overcoming the limit in capacity, typical of conventional cathode materials such as Li_xMO_2, but they are also less subject to dimensional changes compared with the elemental sulfur-based electrodes, thereby becoming alternative promising electrode materials for ASLBs.

3. EXPERIMENTAL

3.1. Material Preparation

Crystalline Li_4SnS_4 powders as precursors for the solution process were prepared by heat-treatment of 2 g of a pelletized stoichiometric mixture of Li_2S (99.9%, Alfa Aesar) and SnS_2 (99.999%, American elements) at 450°C in a quartz ampoule sealed under vacuum. For the solution-based synthesis of LiI-Li_4SnS_4, a stoichiometric amount of the as-prepared Li_4SnS_4 and LiI (99.95%, Alfa Aesar) was dissolved into anhydrous MeOH (99.8%, Sigma-Aldrich) under dry Ar. For typical preparation, 0.36–0.49 *M* solution (concentration for xLiI-(1-x)Li_4SnS_4 or 100 mg (mL of MeOH)$^{-1}$) was used. After the powders were obtained under vacuum at room temperature, further heat-treatment under vacuum at designated temperatures (200°C, 320°C, and 450°C) resulted in the final samples. The solution-processable LiBr-Li_4SnS_4 powders were prepared by using LiBr (99.95%, Alfa Aesar) and Li_4SnS_4 by following the same procedure as that for LiI-Li_4SnS_4. The 0.4LiI-0.6Li_4SnS_4-coated $LiCoO_2$ powder was prepared by the same solution process in the presence of $LiCoO_2$ powders with a HT temperature of 200°C; In order to mitigate undesirable side reactions, 0.3 wt% $LiNbO_3$-coated $LiCoO_2$ powders were used.[6,33,97] The entire preparation procedure was carried out without exposure to air. The LPS (1.0×10^{-3} S cm^{-1} at 30°C) and LGPS (6.0×10^{-3} S cm^{-1} at 30°C) powders were prepared by ball-milling followed by HT at 243°C for 1 h and by solid-state reaction at 550°C, respectively.

Na_3SbS_4 powders were prepared by heat-treatment of stoichiometric mixture of Na_2S (Sigma Aldrich), Sb_2S_3 (99.5%, Sigma Aldrich), and elemental sulfur (99.5%, Alfa Aesar) at different temperatures in a quartz ampoule sealed under vacuum. The Na_3PS_4 (NPS) powders were prepared by mechanochemical milling of stoichiometric mixture of Na_2S and P_2S_5 (99%, Sigma Aldrich) for 10 h, followed by heat-treatment at 270°C for 1 h in a sealed glass ampoule. For the solution-based synthesis of Na_3SbS_4, the as-prepared Na_3SbS_4 powders were fully dissolved into anhydrous MeOH (99.8%, sigma Aldrich) or deionized water under dry Ar. For typical preparation, 0.9 *M* solution was used. After the powders were dried under vacuum at room temperature, further heat-treatment was carried out at different temperatures (100°C, 150°C, 200°C) under vacuum. $NaCrO_2$ powders were prepared by heat-treatment of stoichiometric mixture of Cr_2O_3 (98%, Sigma Aldrich) and Na_2CO_3 (99.5%, Sigma Aldrich) at 900°C for 10 h under Ar. The Na_3SbS_4-coated NCO powders were prepared by following the same MeOH-solution process in the presence of NCO powders with a heat-treatment temperature of 200°C.

3.2. Material Characterization

The TGA profile was obtained from 25°C to 600°C at 0.167°C s^{-1} under N_2 using a SDT Q600 (TA Instrument Corp.). XRD cells containing hermetically sealed LiI-Li_4SnS_4 samples with a beryllium window were mounted on a D8-Bruker Advance diffractometer equipped with Cu Kα radiation (0.154056 nm), and were subjected to measurements at 40 kV and 40 mA using a continuous scanning mode at 0.025° s^{-1}.

The Raman spectra were measured using a Raman spectrometer (Alpha300R, WITec) with a 532-nm He–Ne laser. The HRTEM and EDXS elemental mapping images were obtained using JEM-2100F (JEOL). The HRTEM images were obtained with 200 kV of acceleration voltage and 115 μA of electron beam current. The EDXS elemental mapping images were obtained using 80 mm2 X-Max silicon drift detector (energy resolution = 128 eV) and the INCA software from Oxford Instruments. The abberation-corrected scanning TEM was operated at 200 keV, and the corresponding EDXS elemental maps were acquired using a Bruker solid-state detector. The FESEM images were obtained using the S-4800 (Hitachi Corp.). The cross-sectioned FESEM images and EDXS elemental maps for the 0.4LiI-0.6Li4SnS4-coated $LiCoO_2$ electrode were obtained using a JSM-7000F (JEOL) after polishing the cross-sectioned surface at 5 kV for 13 h with an Ar ion beam (JEOL, SM-0910). The weight fraction of the SE coating layer for the 0.4LiI-0.6Li_4SnS_4-coated $LiCoO_2$ powders was determined by inductively coupled plasma optical emission spectroscopy (ICP-OES) using the 720-ES (Varian Corp.). The SE and composite electrode pellets used for characterization were prepared under a pressure of 370 MPa. The ^{7}Li static NMR measurements were carried out using a Bruker Avance II 500 MHz Solid NMR spectrometer. The spectra were recorded at 194.4 MHz with 45^{o} pulses. The solid-state ^{119}Sn MAS NMR spectra at room temperature was obtained at 186.5 MHz at a rotor frequency of 10 kHz with 4.0 μs of 90^{o} pulses using Bruker Avance II 500 MHz Solid NMR spectrometer. Chemical shifts for ^{7}Li and ^{119}Sn NMR are referenced to 1.0 *M* aqueous LiCl solution and

tetramethyltin, respectively. The Sn K-edge XANES and EXAFS data were obtained on the BL10C beamline (wide-energy XAFS) at the Pohang Light Sources (PLS) under a ring current of 400 mA at 2.5 GeV. Energy calibration was carried out prior to measurement with Sn foil. The LiI-Li_4SnS_4 samples for XANES and EXAFS measurements were hermetically sealed by coating with polyimide film.

SDT Q600 (TA Instrument Corp.) was used for measuring TGA profile up to 400^oC at the heating rate of 4^oC min^{-1} under Ar flow. The Raman spectra were recorded using Raman spectrometer (Alpha300R, WITec) with the He-Ne laser source of wavelength of 532 nm. As the reference samples for Raman results, Sb_2S_3 (99.5%, Sigma Aldrich) and Sb_2S_5 which was prepared by solid-state reaction from a mixture of Sb_2S_3 and elemental sulfur in an ampoule sealed under vacuum at 500^oC were used. The FESEM images were obtained by using S-4800 (Hitachi Corp.). The EDXS elemental mapping was carried out by using JSM-7000F (JEOL). The HRTEM and its corresponding EDXS elemental mapping images were obtained using JEM-2100F (JEOL). The HRTEM images were obtained with 200 kV of acceleration voltage. The FIB-sectioned Na_3SbS_4-coated NCO sample was prepared by using a 30 keV Ga^+ ion beam. The pellets used for the cross-sectional FESEM images and the corresponding EDXS elemental maps in are comprised of the composite electrode layer and SE layer. For the purpose to obtain a mechanically intact pellet, the SE layer was reinforced with a poly(paraphenylene terephthalamide) (PPTA) non-woven scafold. The cross-sectional FESEM images and EDXS elemental maps were obtained using JSM-7000F (JEOL). The Na_3SbS_4-coated NCO electrodes and the mixture electrodes are the same as those

use for the electrochemical characterization. A 5 keV Ar^+ ion beam was used for sectioning using SM-0901 (JEOL). For FESEM, FIB, and HRTEM measurements, exposure of the samples to ambient air in a short period of time was inevitable. The amount of SE (Na_3SbS_4) coated on NCO was measured by inductively coupled plasma optical emission spectroscopy (ICPOES) using the 720-ES (Varian Corp.).

3.3. Electrochemical Characterization

After the LiI-Li_4SnS_4 pellets were prepared by cold-pressing at 370 MPa, the Li-ion conductivity was measured by an AC impedance method using an Iviumstat (IVIUM Technologies Corp.) with symmetric Li-ion blocking c-Al/SE/c-Al cells, in which the carbon coating layers face the SE. All-solid-state cells were fabricated as follows: Composite electrodes were prepared from the LiI-Li_4SnS_4/$LiCoO_2$ mixture or the LiI-Li_4SnS_4-coated $LiCoO_2$. $Li_{0.5}In$ prepared by mixing In (99%, Sigma Aldrich) and Li (FMC Lithium Corp.) powders were used as the counter and reference electrode materials. After the SE layer was formed by pelletizing 150 mg of LPS powders by pressing at 74 MPa, 15 mg of the as-prepared composite electrodes was spread, followed by pressing at 370 MPa. Then, 100 mg of the as-prepared $Li_{0.5}In$ was attached on the other side of SE layer by pressing at 370 MPa. All procedures were performed in a polyaryletheretherketone (PEEK) mould (diameter = 1.3 cm) with two Ti metal rods as current collectors. All processes for preparing the SEs and fabricating the all-solid-state cells were performed in an Ar-filled dry box. Galvanostatic charge–

discharge cycling test was performed at 30°C with current densities of 0.11, 0.22, 0.55, 0.77, and 1.10 mA cm^{-2}. The same current density was applied for charge and discharge. The Nyquist plots for the $LiCoO_2$/Li-In cells were obtained after charging at 0.11 mA cm^{-2} (0.1C) to 30 mA h g^{-1} and resting for more than 3 h. The GITT measurements were carried out with a pulse current of 0.55 mA cm^{-2} for 60 s and rest for 2 h. For the dry-air-stability test, 250 mg of LPS or the 0.4LiI-0.6Li_4SnS_4-coated $LiCoO_2$ powders was kept under a flow of dry air (a mixture of O_2 and N_2 with 21/79 vol. ratio).

After the Na3SbS4 pellets were prepared by cold-pressing at 370 MPa, the ionic conductivity was measured by an AC impedance method using an Iviumstat (IVIUM Technologies Corp.) with symmetric Na-ion blocking Ti/SE/Ti cells.

Electronic conductivity of the SE pellet was measured by four-probe method.[95] All-solid-state Na-ion cells were fabricated as follows: Composite electrodes were prepared from the Na_3SbS_4-coated NCO or Na_3SbS_4/NCO mixture. Na_3Sn prepared by mixing of Na metal (sigma Aldrich) with Sn metal powders (Sigma Aldrich) served as the counter electrode, exhibiting an operating voltage of ~0.1 V (*vs*. Na/Na^+). The SE bilayer was formed by cold-pressing 150 mg of Na_3SbS_4 powders together with 50 mg of NPS powders. 10 mg of the as-prepared electrodes (coated or mixture electrode) were spread on the Na_3SbS_4 side of SE bilayer, followed by pressing at 370 MPa. Then, 50 mg of the as-prepared Na_3Sn was attached on the other side of SE bilayer by pressing at 370 MPa. All the procedures were performed in a polyaryletheretherketone (PEEK) mould (diameter = 13 mm) with two Ti metal rods as current collectors. All processes for fabricating the all-solid-state cells were performed in an Ar-filled dry box.

Galvanostatic charge-discharge measurements were performed at 30^{o}C between 1.2-4.0 V with current density of 50 μA cm^{-2}. The Nyquist plots for the NCO/Na-Sn cells were obtained after charge for 1 h. For the dry-air stability, 100 mg of SE powders were kept under a flow of dry air (a mixture of O_2 and N_2 with 21/79 vol. ratio) for 24 h. The charge-discharge test of NCO/Na cell using liquid electrolyte was obtained by using 2032-type coin cells. The composite electrode was prepared by spreading NCO powders, Super P, and poly(vinylidene fluoride) (PVDF) binder (KF1100, Kureha Inc.) on Al foil. The weight ratios of NCO:Super P:PVDF were 80:10:10. A 1.0 *M* solution of $NaPF_6$ dissolved in a mixture of ethylene carbonate (EC), ethylmethyl carbonate (EMC), and dimethyl carbonate (DMC) (3:4:3 v/v) was used as the electrolyte. Na metal foil was used as both counter and reference electrode. The galvanostatic charge-discharge cycling was carried out 50 μA cm^{-2} between 2.0-3.6 V (*vs*. Na/Na^{+}) at 30^{o}C.

4. RESULTS AND DISCUSSION

4.1. LiI-Li_4SnS_4: Lithium Ionic Conductor

4.1.1. Properties of LiI-Li_4SnS_4

For the synthesis of $xLiI-(1-x)Li_4SnS_4$ ($0.0 < x < 5.0$), solutions were prepared by dissolving both LiI and Li_4SnS_4 together into anhydrous MeOH. Figure 2 shows the homogenous MeOH solution containing fully dissolved LiI and Li4SnS4 (0.46 *M* of a formula unit of $0.4LiI-0.6Li_4SnS_4$, 100 mg mL^{-1}). Powders obtained by drying the as-prepared solution under vacuum at room temperature were subjected to thermogravimetric analysis (TGA) under N_2, as shown in Figure 3. Owing to its low boiling point (64.7°C), MeOH was removed below 160°C, based on which three different heat-treatment (HT) temperatures (200°C, 32°C, and 450°C) were selected. Hereafter, $xLiI-(1-x)Li_4SnS_4$ prepared at a temperature of y (°C) is referred to as "xLiI-(1-x)LSS-y".

Figure 4, 5 show the X-ray diffraction (XRD) patterns and ionic conductivities at 30°C with activation energies for $xLiI-(1-x)Li_4SnS_4$ samples ($0.0 < x < 5.0$) prepared at different temperatures. The sample prepared at 450°C exhibits a pure crystalline Li_4SnS_4.[44] As the HT temperature is decreased to 320°C, the XRD pattern shows lowered crystallinity. Decreasing the HT temperature further to 200°C results in an almost amorphous feature. The ionic conductivities of cold-pressed pellets prepared under 370 MPa were measured using Li-ion blocking c-Al/SE/c-Al cells (c-Al: carbon-

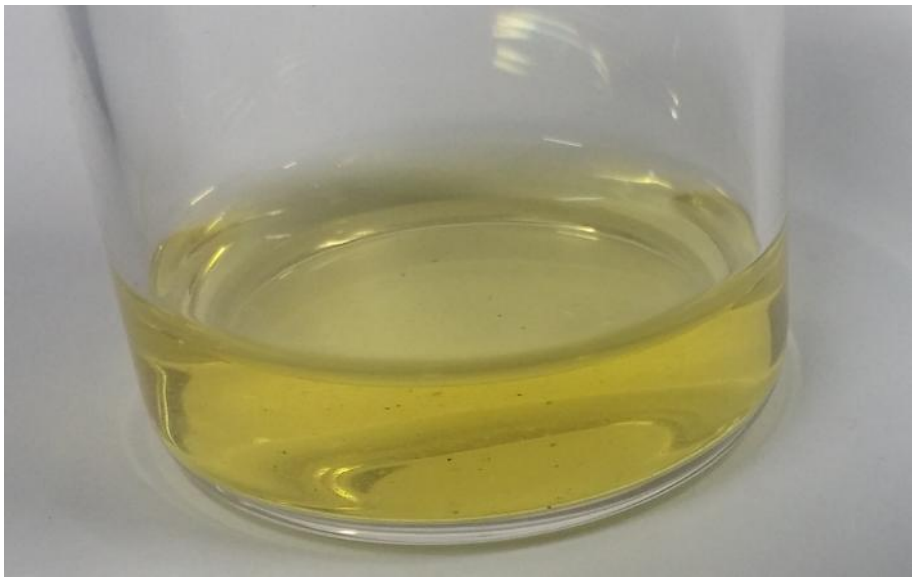

Figure 2. Photograph of LiI- and Li_4SnS_4-dissolved MeOH

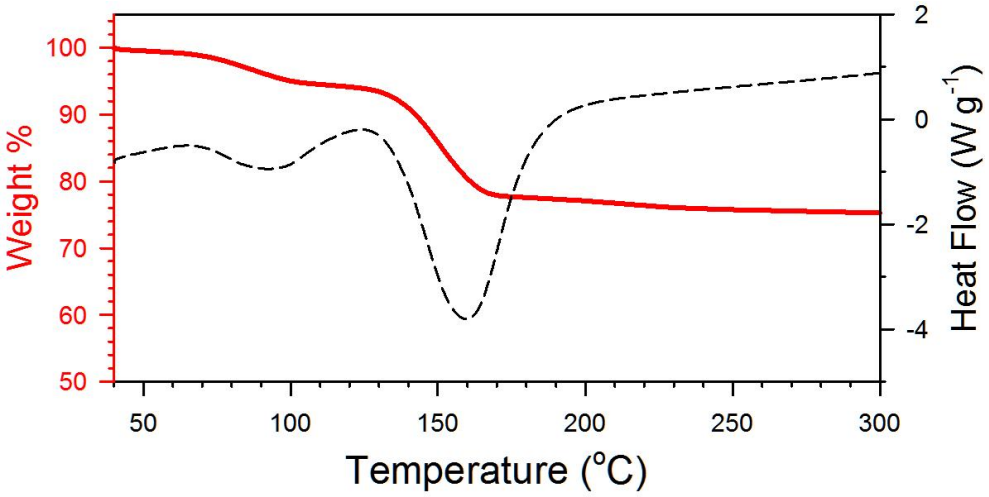

Figure 3. TGA profile under N_2 for the Li_4SnS_4 powders obtained by drying the solution under vacuum at room temperature.

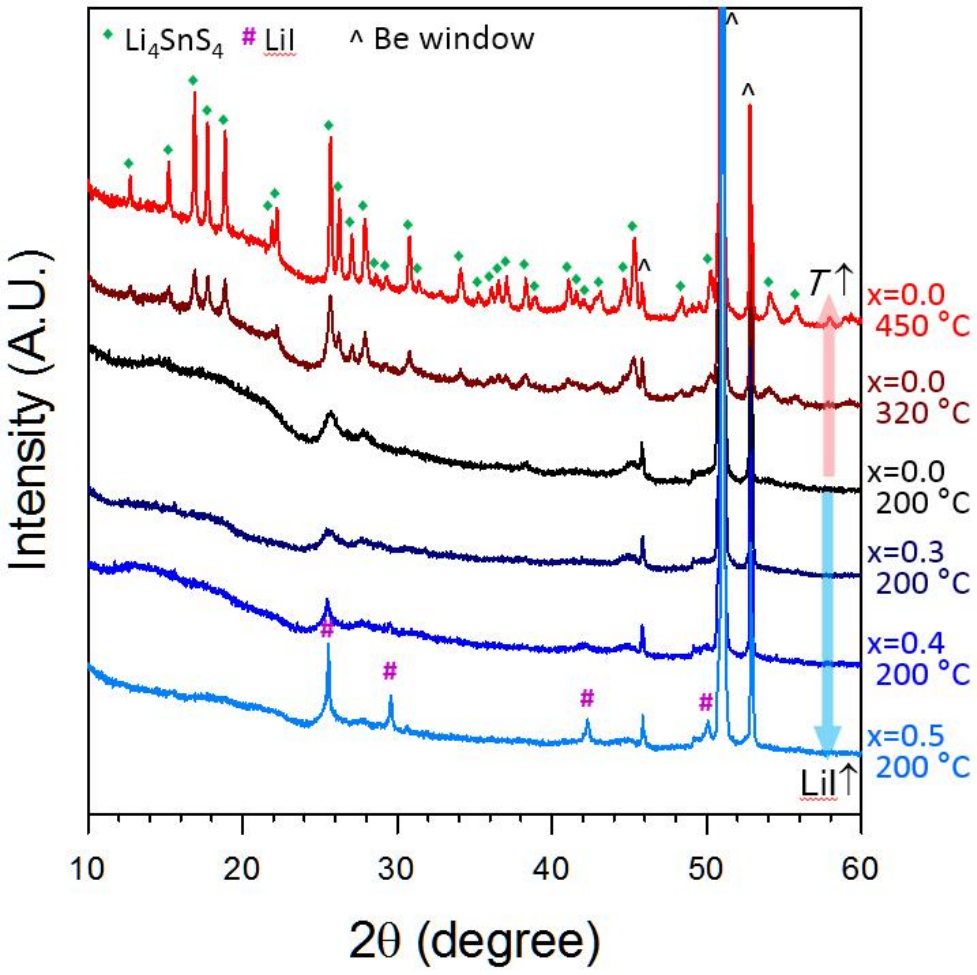

Figure 4. XRD patterns of xLiI-(1.0-x)Li_4SnS_4. The composition and preparation temperature are given.

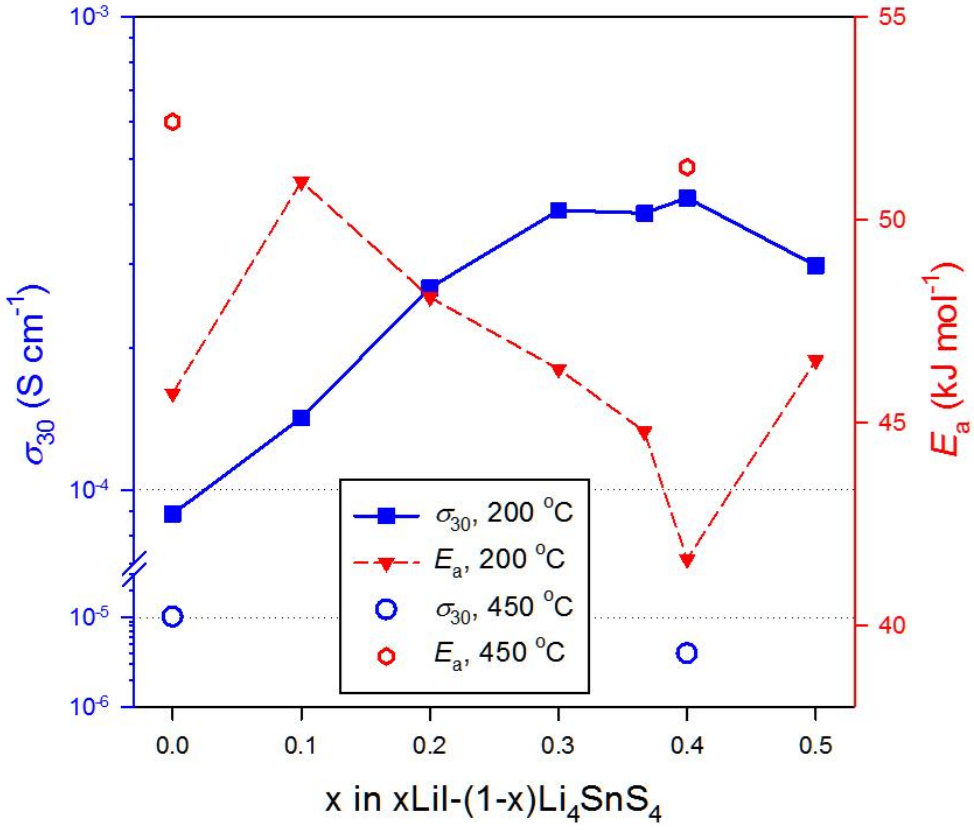

Figure 5. Conductivities of xLiI-(1.0x)Li_4SnS_4 at 30°C and activation energies as a function of x in xLiI-(1-x)Li_4SnS_4.

coated Al foil) by the AC impedance method (Nyquist and Arrhenius plots are shown in Figure 6). Li_4SnS_4 prepared at 450°C exhibits a conductivity of 1.0×10^{-5} S cm^{-1}. Surprisingly, decreasing the HT temperature leads to an increase in the conductivity (2.1×10^{-5} S cm^{-1} at 320°C and 8.9×10^{-5} S cm^{-1} at 200°C). Considering that a minimum temperature of 320°C is required for complete dehydration when using an aqueous solution,[44] the significantly enhanced conductivity at 200°C in this work highlights the exceptional benefit of using the low-boiling-point MeOH. As x in xLiI-(1-x)Li_4SnS_4 increases up to 0.4, the XRD-amorphous features are retained and the conductivity increases gradually, with the highest conductivity value reaching 4.1×10^{-4} S cm^{-1} and the lowest activation energy reaching 41.6 kJ mol^{-1}. Subsequently, the conductivity is decreased at x = 0.5, at which the segregated crystalline LiI (JCPDS No. 71-3746) is observed (Figure 5).

Apart from one exception (x = 0.0 *vs*. 0.1), the activation energies inversely follow the trend of ionic conductivities. The activation energy for Li hopping (E_a^{MN}) was obtained from motional narrowing (MN) ^{7}Li NMR data (Figure 7) by the following Equation.[112]

$$\Delta\nu(T) = \Delta\nu_R\left[1+\left(\frac{\Delta\nu_R}{B}-1\right)exp\left(-\frac{E_a^{MN}}{k_BT}\right)\right]^{-1}+D$$

where $\Delta\nu(T)$: line width (full width at half maximum (FWHM)), k_B: Boltzmann constant, T: absolute temperature, D: temperature independent line width, $\Delta\nu(T)_R$ and B:

fitting

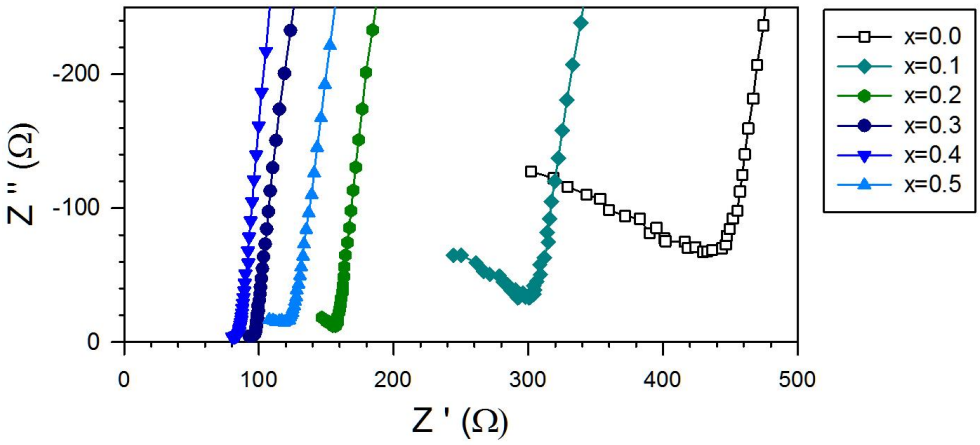

Figure 6. The nyquist plots for xLiI-(1.0-x)Li_4SnS_4 prepared at 200°C. Li-ion-blocking cells C-Al/SE/C-Al were used at 30°C

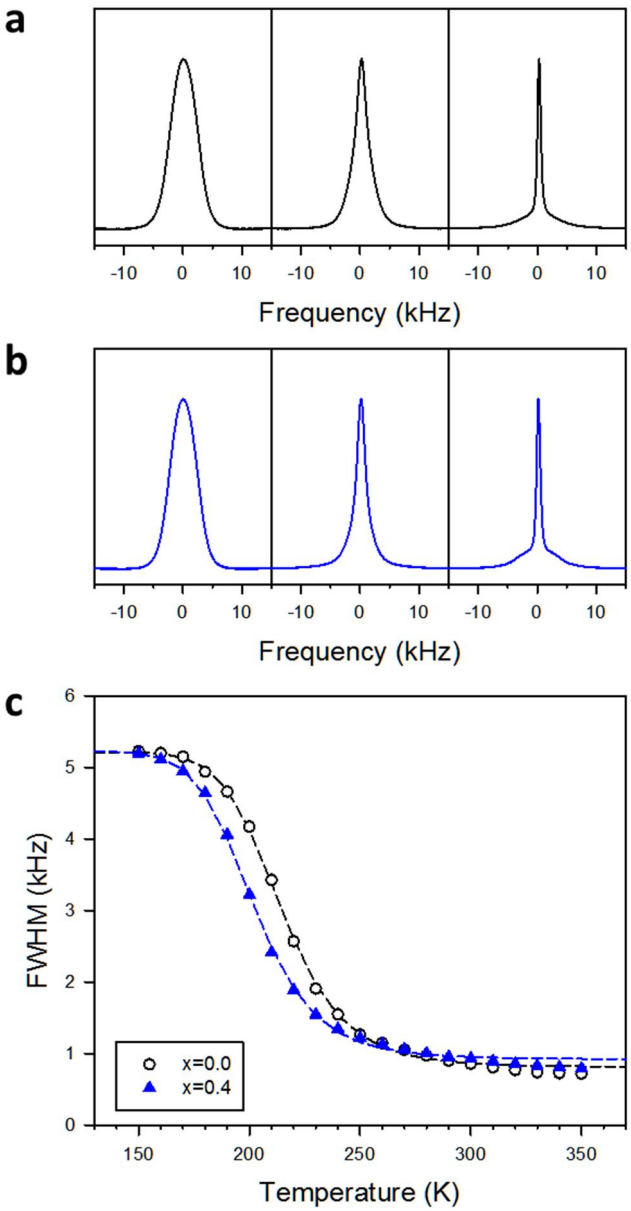

Figure 7. ^{7}Li NMR results for LiI-Li_4SnS_4. ^{7}Li NMR spectra for a, Li_4SnS_4 and b, 0.4LiI-0.6Li_4SnS_4 prepared at 200^{o}C measured at various temperatures. C, Motional narrowing of the ^{7}Li NMR linewidth of LiI-Li_4SnS_4. The short dashed lines are plotted by using the mathematical fitting.

parameters. The parameters used for obtaining the activation energies for Li_4SnS_4 and $0.4LiI\text{-}0.6Li_4SnS_4$ prepared at 200°C are provided in Table 1.Consistent with the results from the AC impedance method, the activation energy obtained from motional narrowing of the ^7Li nuclear magnetic resonance (NMR) data[112] also confirms the lower activation energy of 0.4LiI-0.6LSS-200 (24.7 kJ mol^{-1}) compared to that of LSS-200 (27.3 kJ mol^{-1}) (Figure 7). The difference in the activation energy values from the AC impedance and the ^7Li NMR stem from the different time windows of sensing.[113,114] While NMR is sensitive to local Li-ion hopping, AC impedance is sensitive to the overall contributions of Li-ion movements, such as grain boundary resistance. Increasing HT temperature for $0.4LiI\text{-}0.6Li_4SnS_4$ to 450°C resulted in the formation of SnI_4 and a decrease in conductivity (4.0×10^{-6} S cm^{-1}, Figure 8). Overall, it is evident that both the composition (the inclusion of LiI) and the structure (whether XRD-amorphous or crystalline as well as whether crystalline LiI is segregated or not) affect the ionic conductivities.

As the first step to elucidate the microstructures of $LiI\text{-}Li_4SnS_4$, high-resolution transmission electron microscopy (HRTEM) analyses were carried out. Figure 9 exhibit HRTEM images and their corresponding selected-area electron diffraction (SAED) patterns for LSS-200 and 0.4LiI-0.6LSS-200, respectively. Contrary to the XRD-amorphous feature in Figure 4, the LSS-200 here appears to consist of nanometre-sized crystallites. The lattice fringes and the SAED patterns in the inset of Figure 9a unequivocally indicates that the nanocrystallites belong to orthorhombic Li_4SnS_4.[44] In sharp contrast, the HRTEM image and the featureless SAED pattern in

Figure 9b reveal

Table 1. Parameters for motional narrowing ^{7}Li NMR data for LiI-Li_4SnS_4

xLiI-(1-x)Li_4SnS_4	[illegible]	[illegible]	[illegible]	[illegible]
0.0	4403	9.97×10^{-4}	809	0.28
0.4	4301	1.77×10^{-3}	918	0.26

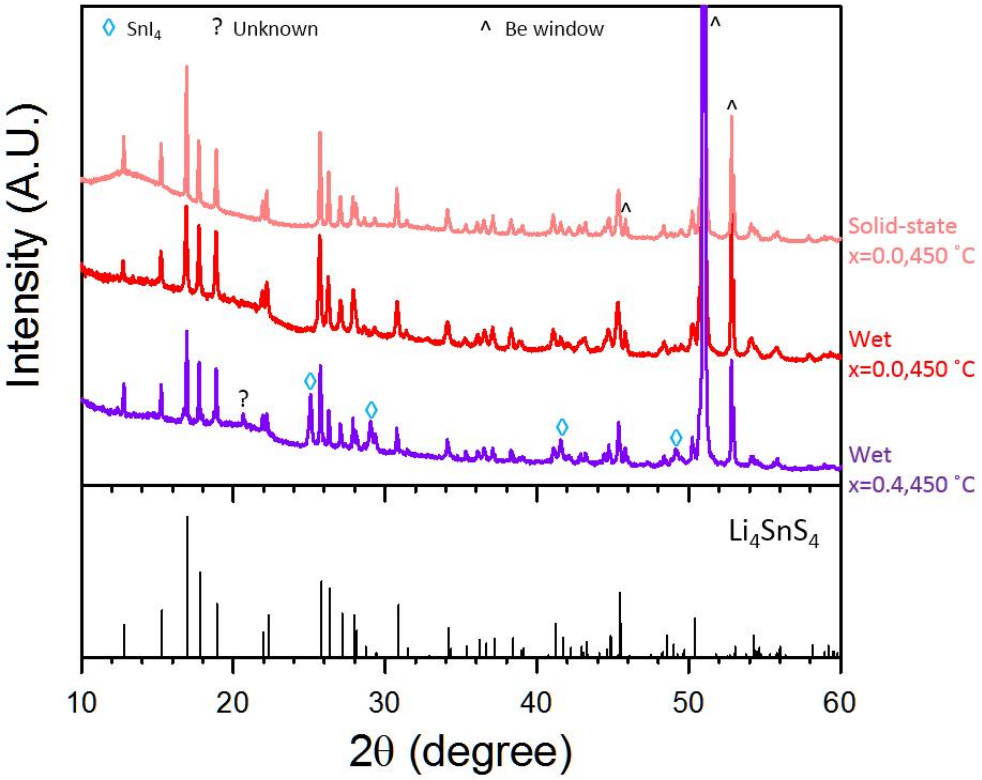

Figure 8. XRD patterns for $xLiI\text{-}(1\text{-}x)Li_4SnS_4$ prepared at 450°C. Peaks for the reference of orthorhombic Li_4SnS_4 are given at the bottom. Note the evolution of SnI_4 (JCPDS no. 06-0232) and the unknown peak for the solution-processed $0.4LiI\text{-}0.6Li_4SnS_4$ prepared at 450°C

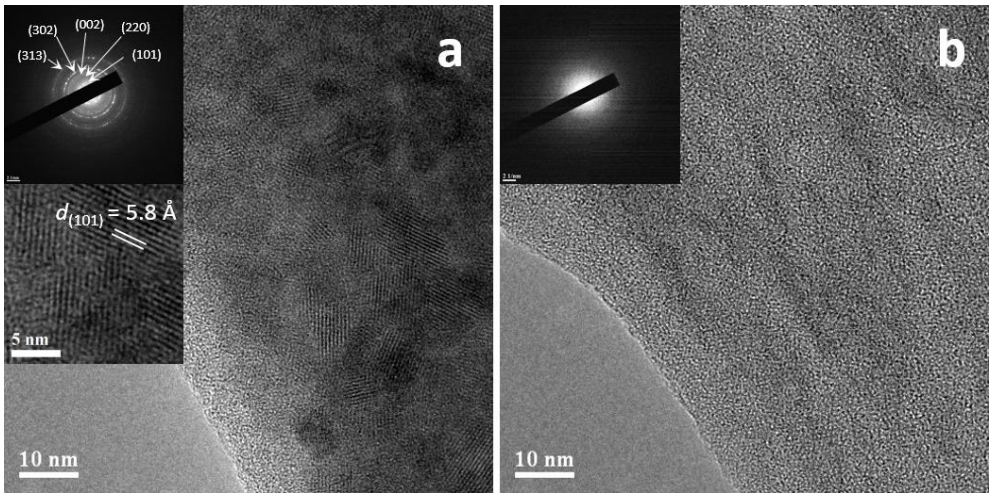

Figure 9. HRTEM images of a) Li_4SnS_4 and b) 0.4LiI-0.6Li_4SnS_4 prepared at 200°C

a completely amorphous structure for 0.4LiI-0.6LSS-200, indicating that the added LiI acts as the glass former by dissolving into Li_4SnS_4. The aberration-corrected scanning TEM image and its corresponding energy dispersive X-ray spectroscopy (EDXS) elemental maps of Sn, S, and I for 0.4LiI-0.6LSS-200 in Figures 10 show homogeneous composition all over the particle. The Raman spectra for LSS-450, LSS-200, and 0.4LiI-0.6LSS-200 (Figure 11) show the strong peaks centred at 345 cm^{-1} originating from SnS_4^{4-}.[57] This result implies that the SnS_4^{4-} polyanion is intact regardless of the HT temperature and the inclusion of LiI, which is also corroborated by the similar ^{119}Sn magic angle spinning (MAS) NMR signatures centred at ~59 ppm for LSS-200 and 0.4LiI-0.6LSS-200 (Figure 12).[44] Further, Sn K-edge extended X-ray absorption fine structure (EXAFS) spectra for LSS-450, LSS-200, 0.1LiI-0.9LSS-200, 0.3LiI-0.7LSS-200, and 0.4LiI-0.6LSS-200 exhibit the main peaks at an identical radial distance that are attributed to Sn-S bonds from SnS_4^{4-}(Figure 13). X-ray absorption near edge structure (XANES) spectra for Sn K-edge and I L-edge show no noticeable difference among the samples (Figure 14). However, a subtle difference between LSS-200 and 0.4LiI-0.6LSS-200 is observed in the 119Sn NMR signatures (Figure 12), where the 0.4LiI-0.6LSS-200 exhibits a slight negative shift in the peak at 59 ppm as compared to LSS-200, indicating the influence of iodide ions in the proximity of SnS_4^{4-}. From the combined spectroscopic analyses, the microstructure of the solution-processed LiI-Li_4SnS_4 prepared at 200^oC is considered to be a disordered matrix consisting of SnS_4^{4-} and I^- anions around which Li^+ cations.

Several factors can be considered to account for the enhancement in conductivity

after

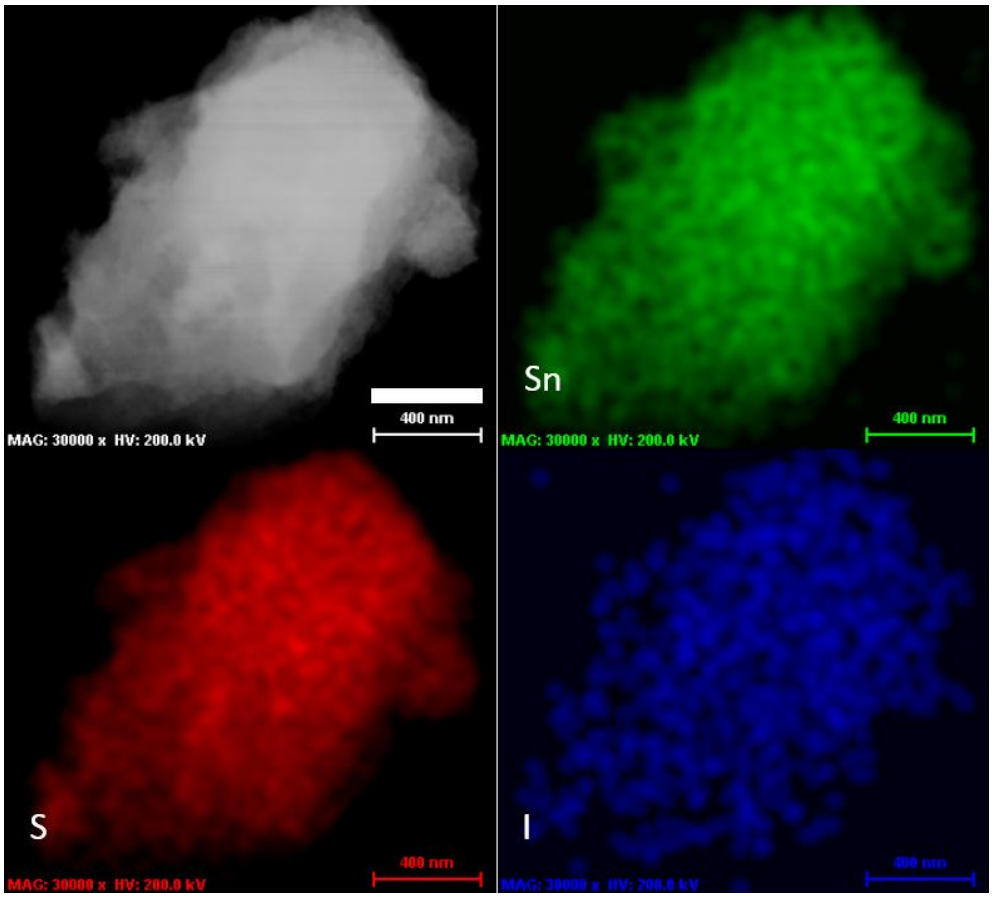

Figure 10. Aberration-corrected scanning TEM image and its corresponding EDXS elemental maps for 0.4LiI-0.6Li_4SnS_4 prepared at 200°C (0.4LiI-0.6LSS-200).

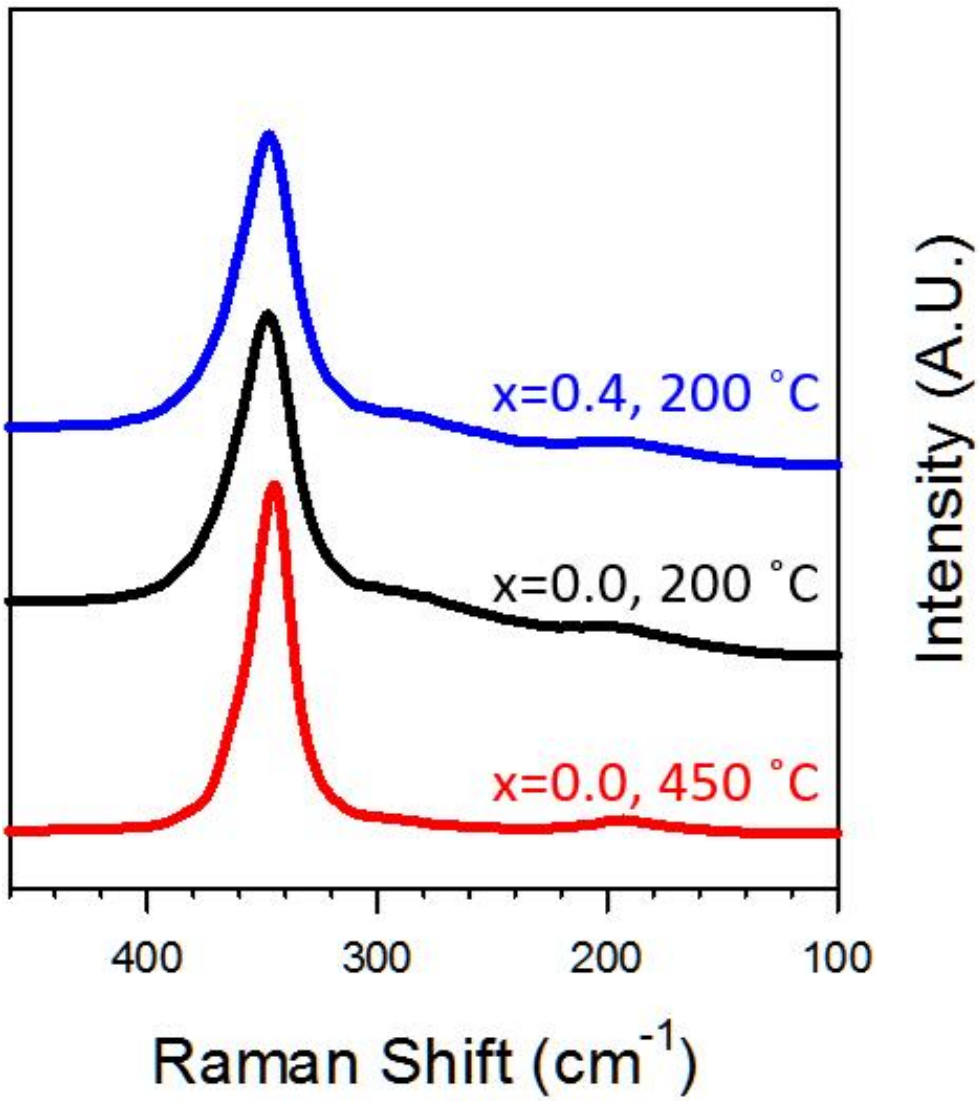

Figure 11. Raman spectra for LSS-450, LSS200, and 0.4LiI0.6LSS-200.

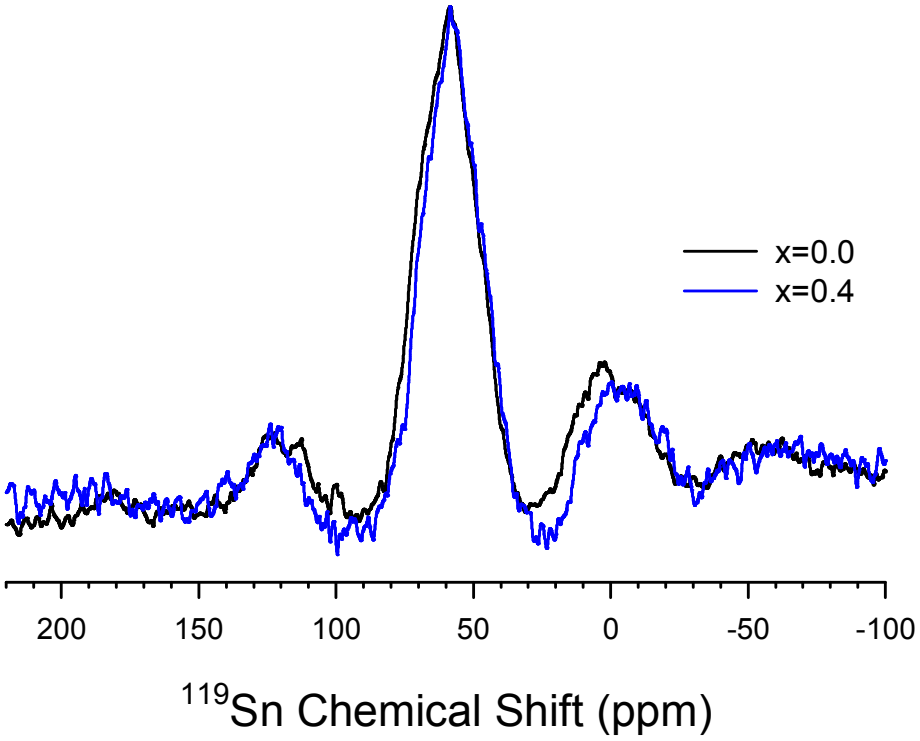

Figure 12. ^{119}Sn NMR spectra for Li_4SnS_4 and $0.4LiI\text{-}0.6Li_4SnS_4$ prepared at 200°C by solution process

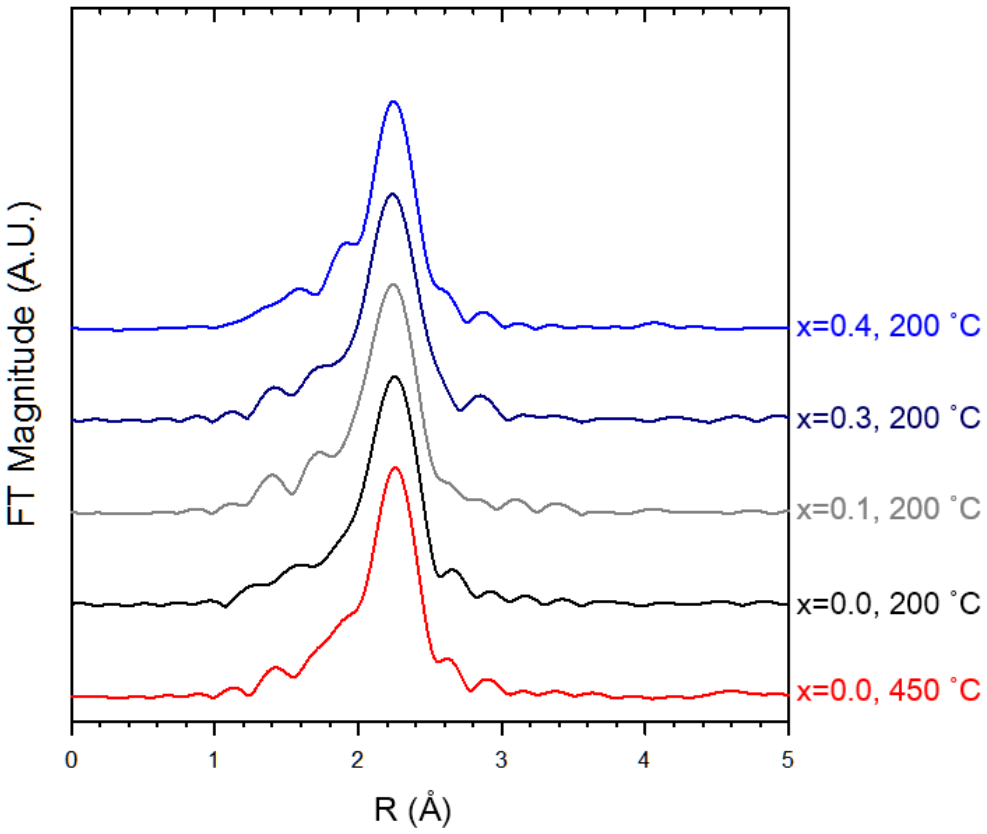

Figure 13. Sn K-edge EXAFS spectra for LSS-450, LSS-200, 0.1LiI-0.9LSS-200, 0.3LiI-0.7LSS-200, and 0.4LiI-0.6LSS-200.

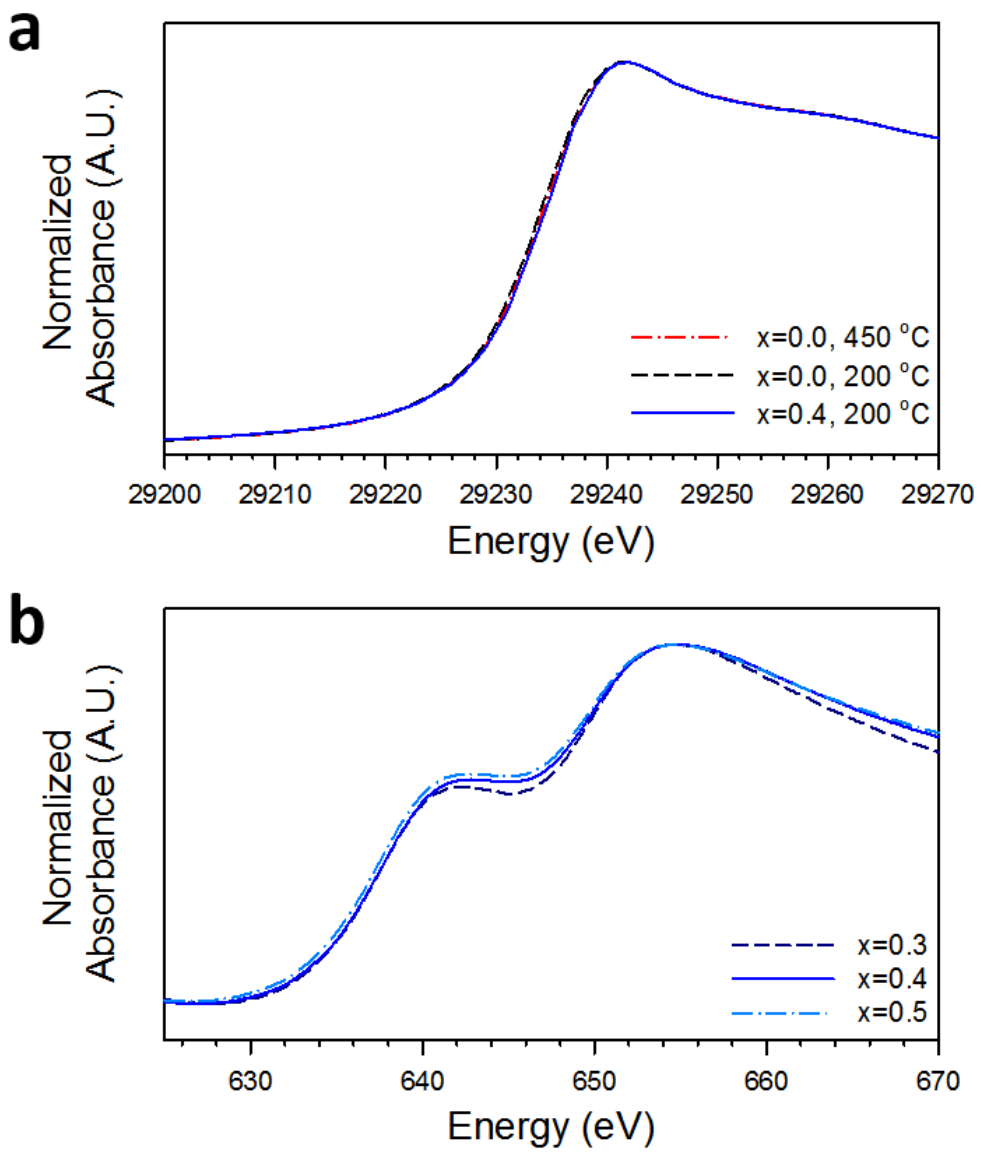

Figure 14. XANES spectra for xLiI-(1-x)Li_4SnS_4. a) Sn K-edge spectra for LSS-450, LSS-200, and 0.4LiI-0.6LSS-200. b) I L-edge spectra for 0.3LiI-0.7LSS-200, 0.4LiI-0.6LSS-200, and 0.5LiI-0.5LSS-200.

adding LiI to Li_4SnS_4 (0.4LiI-0.6LSS-200: 4.1×10^{-4} S cm^{-1} *vs*. LSS-200: 8.9×10^{-5} S cm^{-1}). As a naive consideration, the concentration of Li may be related to the conductivity.[115] However, the change in the concentration of Li from Li_4SnS_4 to $xLiI\text{-}(1\text{-}x)Li_4SnS_4$ is marginal (45.2 atomic % for x = 0.4 vs. 44.4 atomic % for x = 0.0). The increased conductivities at higher x in $xLiI\text{-}(1\text{-}x)Li_4SnS_4$ can be explained by highly open frameworks owing to the large ionic radii of iodide ions (0.206 nm)[116] and/or the lower energy barriers for Li-hopping due to the highly polarizable nature of iodide ions,[19,115] which is supported by the fact that the activation energy decreases as x increases from 0.1 to 0.4 (Figure 5). The decrease in conductivity by replacing the iodide ion by a smaller and less polarizable bromide ion ($0.4LiBr\text{-}0.6Li_4SnS_4$, r = 0.182 nm, 1.4×10^{-4} S cm^{-1}) is also in line with the aforementioned explanation. We also need to explain why the nanocrystalline Li_4SnS_4 prepared at 200°C exhibits much higher conductivity (8.9×10^{-5} S cm^{-1}) than the highly crystalline one prepared at 450°C (1.0×10^{-5} S cm^{-1}). Apart from bulk conductivity, the deformability of SEs could also account for the measured conductivity since it influences the grain boundary or interfacial contact resistances.[9]

Figure 15 show fracture cross-sectional images of the cold-pressed pellets of LSS-450 and LSS-200, and 0.4LiI-0.6LSS-200, respectively. For the highly crystalline LSS-450 pellet (Figure 15a), the particles are not deformed/merged well. Decreasing the HT temperature to 200°C (LSS-200) results in a smoothened cross-sectional surface (Figure 15b), indicating enhanced deformability. Therefore, the main source for the lower conductivity of LSS-450 compared to that of LSS-200 is considered to be the

poor

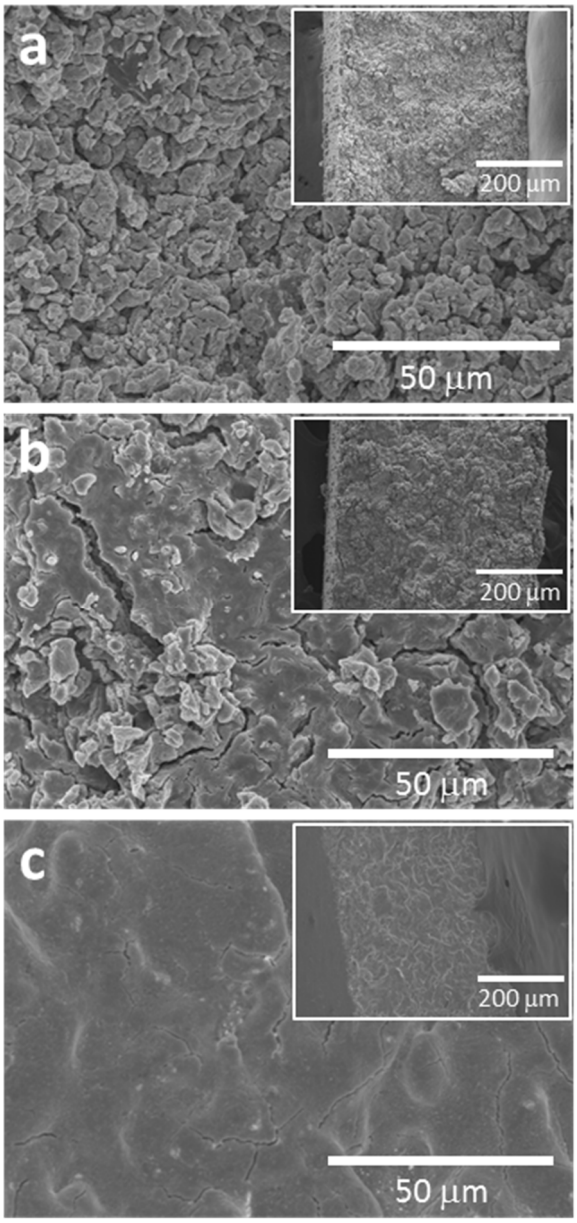

Figure 15. Fracture cross-sectional FESEM images of a) LSS-450, b) LSS-200, and c) 0.4LiI-0.6LSS-200.

interfacial contacts between the particles and grains. The low bond energy at the interfaces between nanocrystallites and/or the defect-rich nanostructures could be responsible for the superior deformation of nanocrystalline Li_4SnS_4 (LSS-200) compared to the highly crystalline one (LSS-450).[18,117] More importantly, for 0.4LiI-0.6LSS-200, an almost poreless fracture cross-sectional surface is observed (Figure 15c). The excellent deformability of 0.4LiI-0.6LSS-200 can be explained by its completely amorphous structure and the presence of iodide ions. Following Fajans' rule, the large size and the high polarizability of iodide ions lead to more covalent nature, resulting in the enhanced deformability.[18,116] The better deformability of 0.4LiI-0.6LSS-200 compared to that of LSS-200 is also confirmed by measurements of density and conductivity as a function of applied pressure. As shown in Figure 16, the density and the conductivity are saturated at far lower pressures for 0.4LiI-0.6LSS-200 than for LSS200. When the electrodes are prepared by mixing $LiCoO_2$ with 30 *wt*% of these SEs and assembled as $LiCoO_2$/Li-In cells, the variations in the electrochemical performances appear dramatic. Figure 17 show the voltage profiles at 0.11 mA cm^{-2} (0.1C) and the associated rate capabilities, respectively. The better performances of the lower overpotential and the higher capacity are achieved for the SEs in the order of 0.4LiI-0.6LSS-200, LSS-200, and LSS-450, thus highlighting the importance of both ionic conductivity and deformability. The excellent deformability of LiI-Li_4SnS_4 would also be advantageous for buffering the volume change of active materials upon repeated charge and discharge.[37] Further exploration on incorporation of other highly polarizable elements and alio-/iso-valent substitutions for Sn and S of Li_4SnS_4 along

with

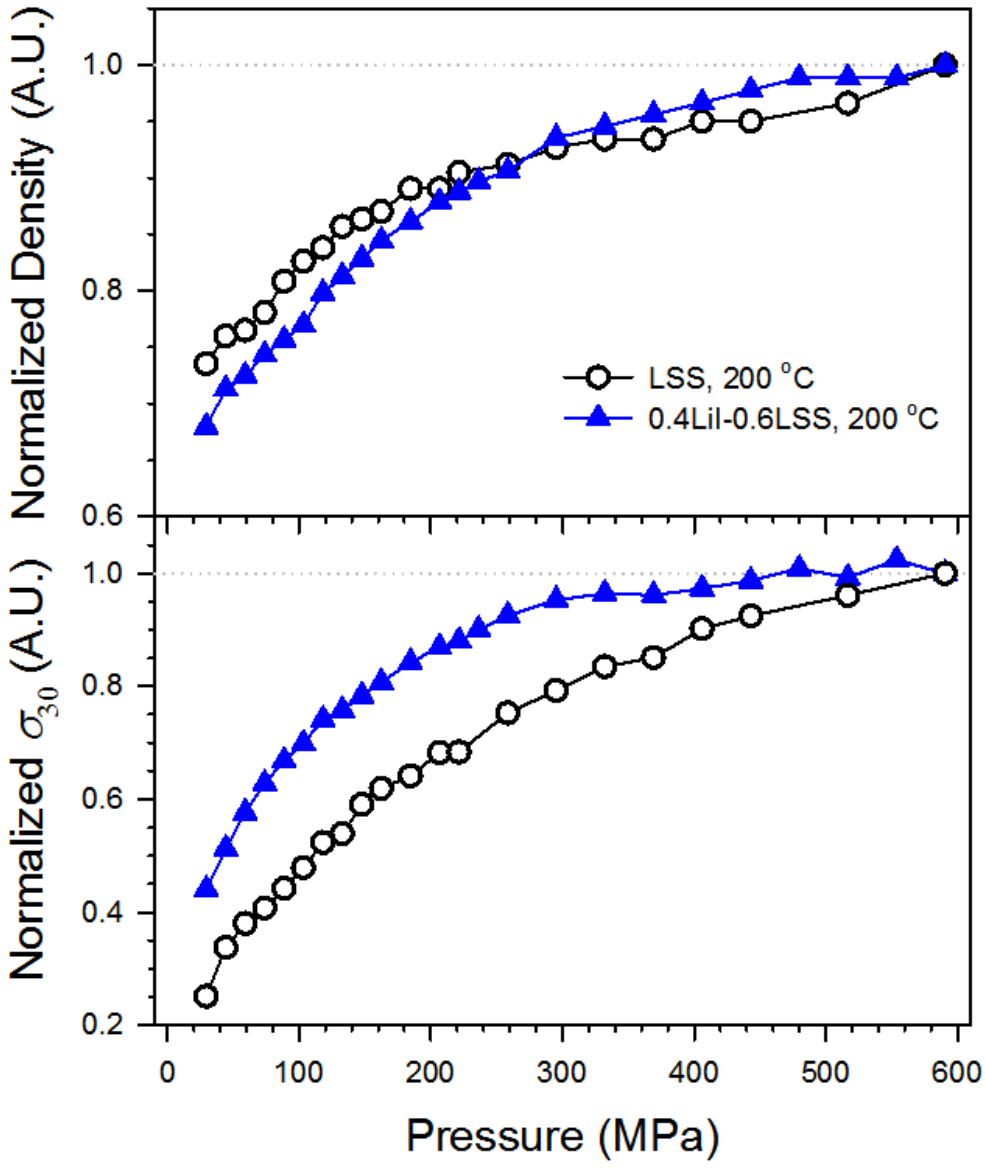

Figure 16. Normalized densities and conductivities at 30°C for LSS-200 and 0.4LiI-0.6LSS-200 as a function of pressure.

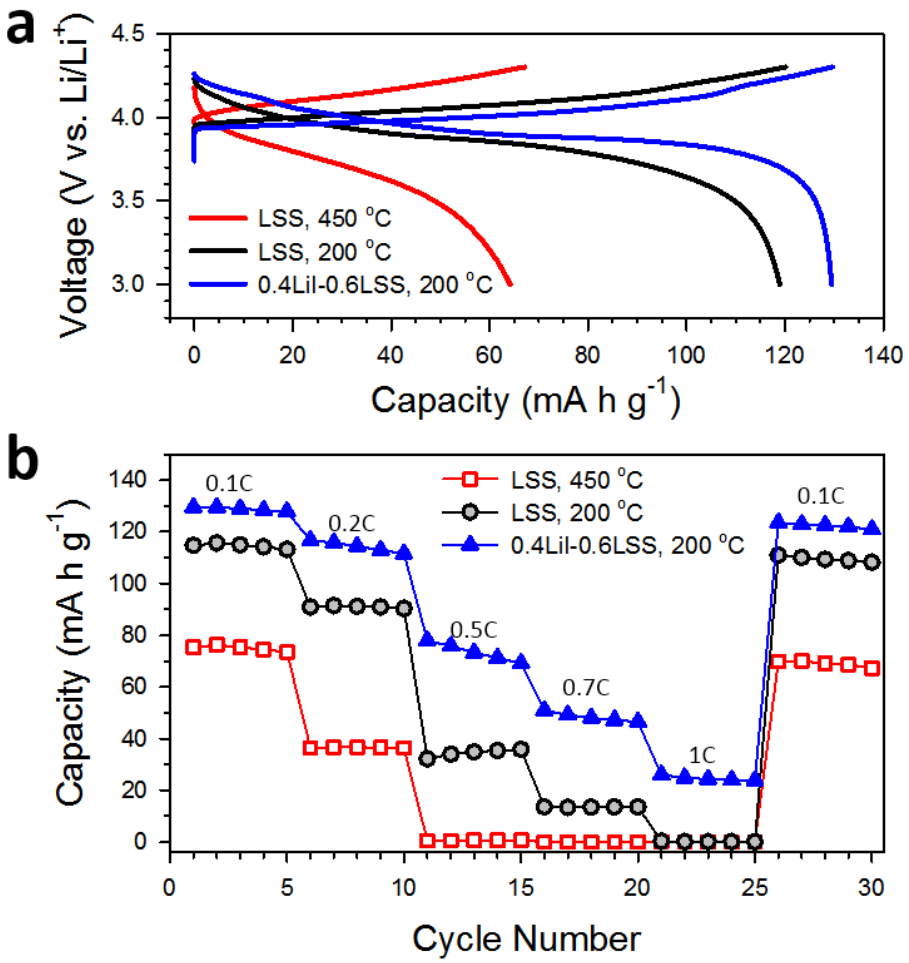

Figure 17. a) Voltage profiles at 0.1 C (0.11 mA cm^{-2}) and b) rate capabilities for $LiCoO_2$/Li-In cells in which the electrodes were prepared by mixing $LiCoO_2$ with LSS-450, LSS200, and 0.4LiI-0.6LSS-200 with a $LiCoO_2$:SE weight ratio of 70:30

fine control of microstructure by solution process may open opportunities to achieve higher conductivities (>10^{-3} S cm^{-1}) than that for 0.4LiI-0.6Li_4SnS_4.

4.1.2. All-solid-state Lithium Batteries using LiI-Li_4SnS_4 Superionic Conductor

0.4LiI-0.6Li_4SnS_4-coated $LiCoO_2$ powders were obtained from the LiI- and Li_4SnS_4-dissolved MeOH solution in the presence of $LiCoO_2$ particles. Since the SE precursor solution wets any exposed surfaces (even porous surfaces) of the $LiCoO_2$ particles and is solidified, it is possible to achieve direct ionic contacts comparable to those in the case of conventional LIBs using liquid electrolytes. Figure 18 shows an field-emission scanning electron microscopy (FESEM) image of the coated $LiCoO_2$ particle and its corresponding EDXS elemental maps, which confirm uniform SE coatings. Direct visualization of the SE coating layer was achieved by HRTEM using a focused ion beam (FIB) cross-sectioned sample as seen in Figure 19. An amorphous SE layer of approximately 100 nm thickness covers the $LiCoO_2$, which is also corroborated by an annular dark field (ADF) TEM image and its corresponding EDXS elemental maps (Figure 20). The direct coating of SEs on active materials offers significant advantages over the conventional mixture electrodes, such as intimate ionic contacts and better spatial distribution of SEs. Figure 21 show FESEM images of the surface of the $LiCoO_2$ composite electrodes prepared by cold-pressing a mixture of $LiCoO_2$ and 0.4LiI-0.6Li_4SnS_4 powders and that of the 0.4LiI-0.6Li_4SnS_4-coated $LiCoO_2$ electrode. While voids are seen between particles in the mixture electrode, the SE-coated $LiCoO_2$

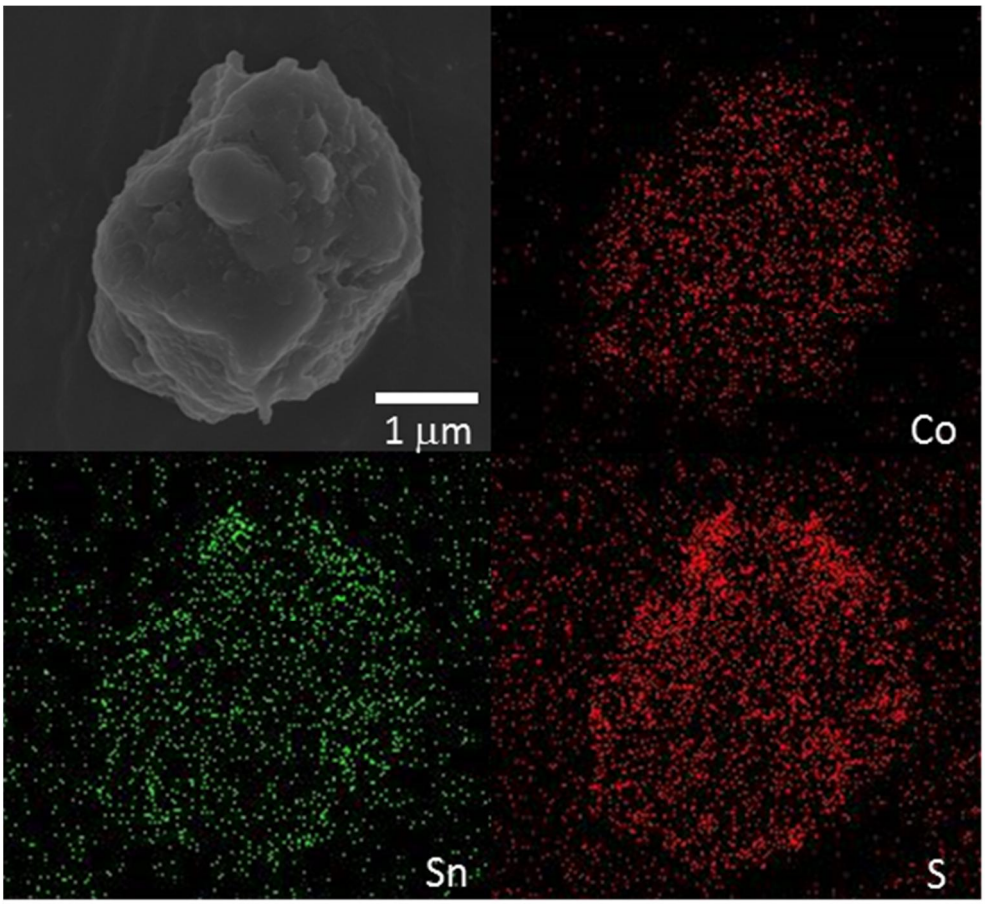

Figure 18. FESEM image of 0.4LiI-0.6Li_4SnS_4-coated $LiCoO_2$ particle and its corresponding EDXS elemental maps.

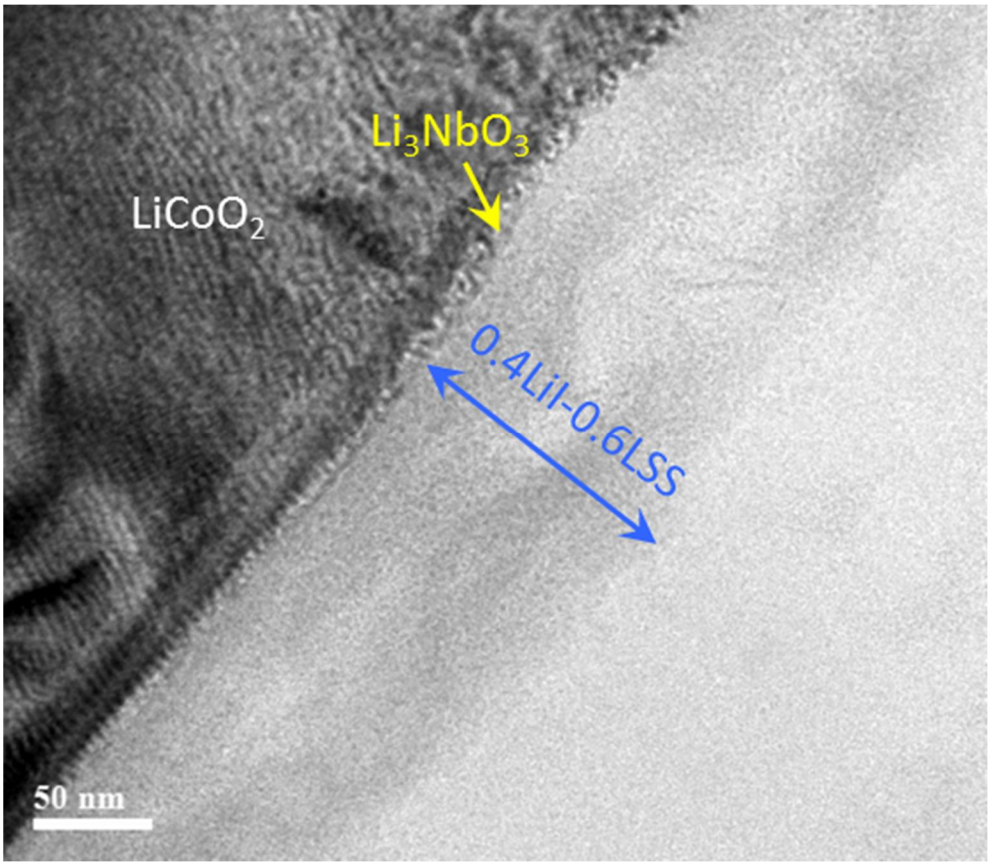

Figure 19. HRTEM image of FIB-cross-sectioned 0.4LiI-0.6Li_4SnS_4-coated $LiCoO_2$ particle.

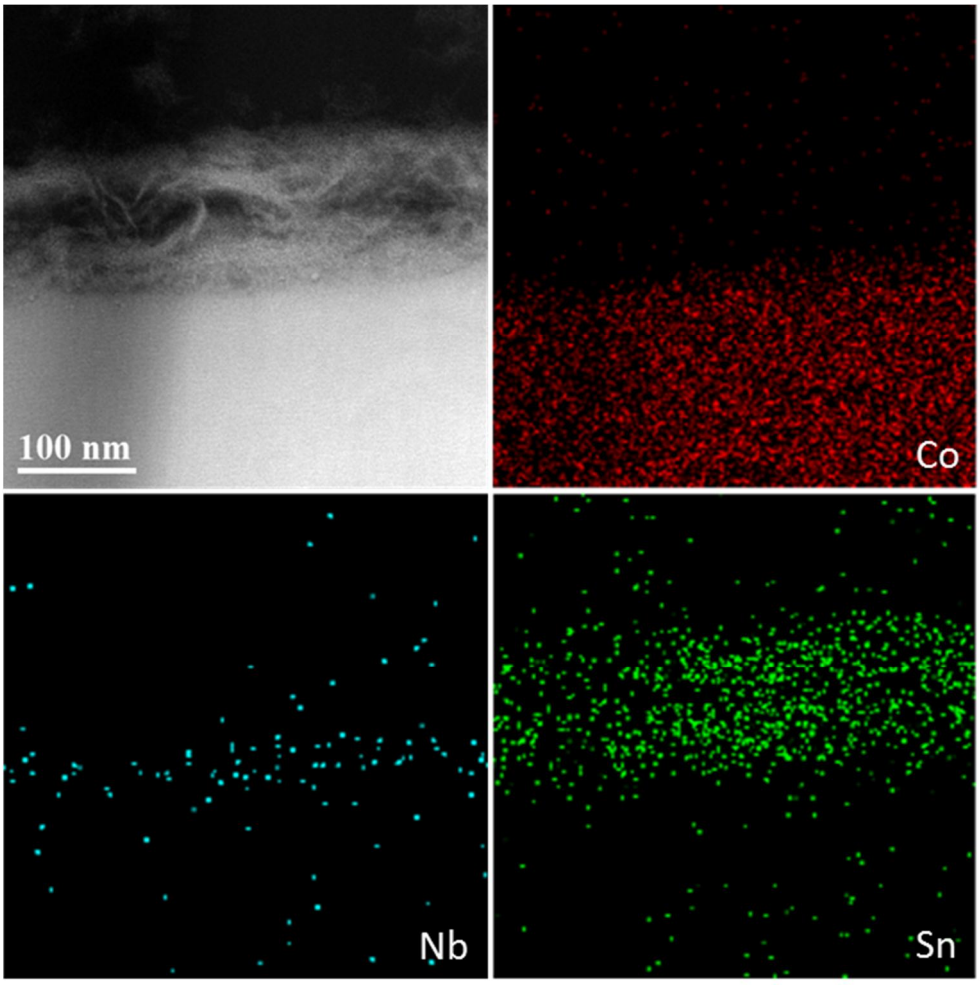

Figure 20. TEM results for FIB-cross-sectioned 0.4LiI-0.6Li_4SnS_4-coated $LiCoO_2$ particle. ADFTEM image and its corresponding EDXS elemental maps.

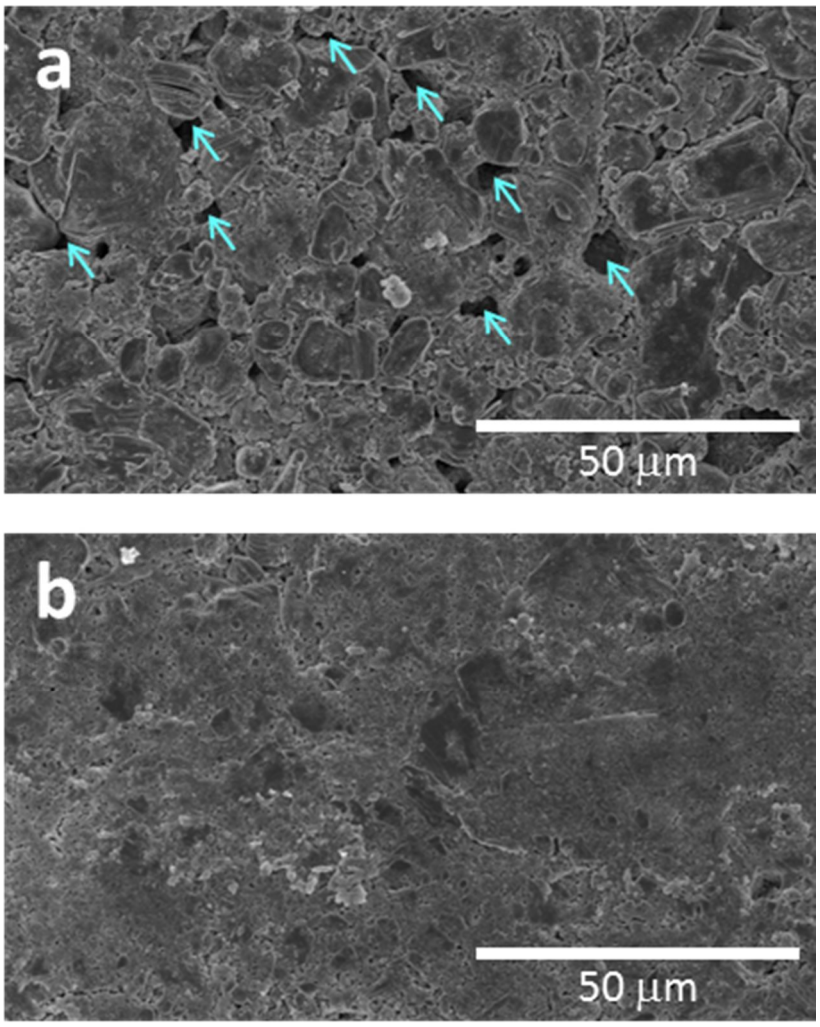

Figure 21. FESEM surface image of a)0.4LiI-0.6Li_4SnS_4/$LiCoO_2$ mixture electrode and b) 0.4LiI-0.6Li_4SnS_4-coated $LiCoO_2$ electrode.

electrode exhibits a smooth and flat surface. Upon cold-pressing, the soft SEs are deformed by the hard $LiCoO_2$ particles and are squeezed to fill the voids between the $LiCoO_2$ particles. The voids observed in the mixture electrode (Figure 21a) reflect poor spatial distribution of SEs and their limited contacts with $LiCoO_2$ particles (Figure 21b). In sharp contrast, a cross-sectioned FESEM and the corresponding EDXS elemental maps for the SE-coated $LiCoO_2$ electrode in Figure 22 show that the SEs are well distributed by filling the spaces between the $LiCoO_2$ particles without noticeable voids, thus implying excellent ionic conduction pathways. This is also consistent with much lower porosity for the 0.4LiI-Li_4SnS_4-coated $LiCoO_2$ electrode (7%) than that for the conventional mixture electrode (12%). The apparent densities of SE were measured by using Archimedes method.

The advantage in ionic contacts by SE coatings on active materials is evaluated by comparing the electrochemical performances of $LiCoO_2$/Li-In cells made of the 0.4LiI-0.6Li_4SnS_4-coated $LiCoO_2$ electrode with the ones made of the conventional mixture electrode. The weight fraction of SE was 15 *wt*%. A diagnostic electrochemical analysis was first carried out by comparing the electrochemical impedance spectroscopy responses for $LiCoO_2$/LPS/Li-In cells (Configuration is depicted in Figure 23a). The Nyquist plots in Figure 24 show one semicircle followed by the Warburg tail. The intercept values at the x-axis and the size of the semicircle are assigned as the resistance of LPS SE layer (~54 Ω) and the interfacial resistance, respectively.[38] The semicircle for SE-coated $LiCoO_2$ electrode (~16 Ω) is smaller than half that of the mixture electrode (~39 Ω), which can be explained by its much

superior ionic contacts. Figure 25 compares

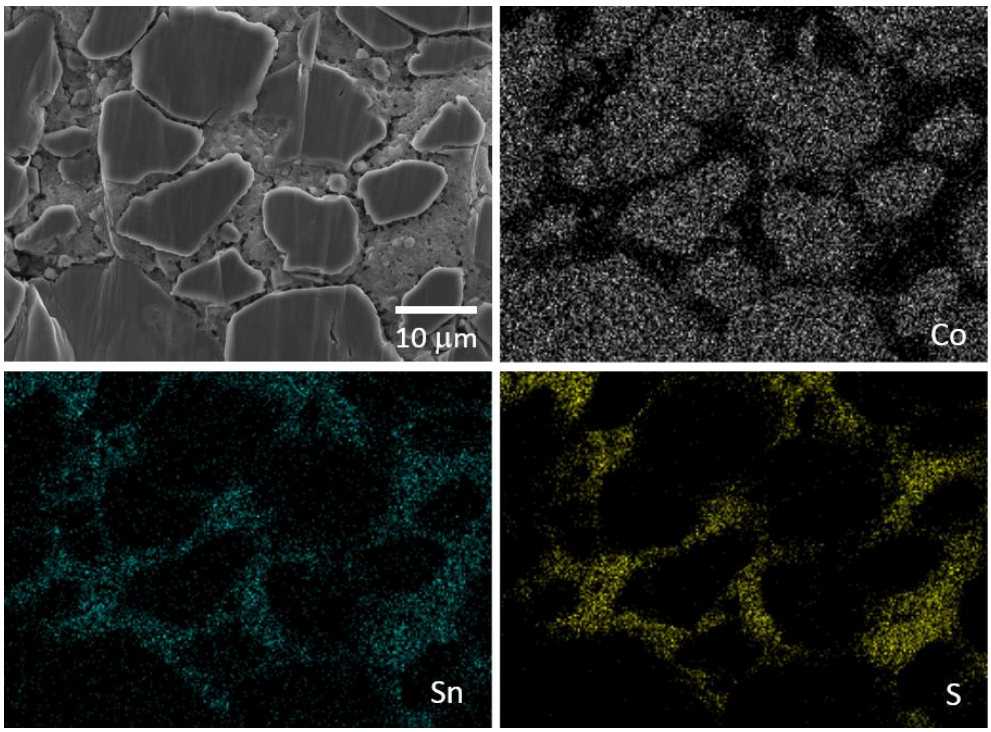

Figure 22. Cross-sectional FESEM image of $0.4LiI\text{-}0.6Li_4SnS_4$-coated $LiCoO_2$ electrode and the corresponding EDXS elemental maps. The $LiCoO_2$:SE weight ratio was 85:15.

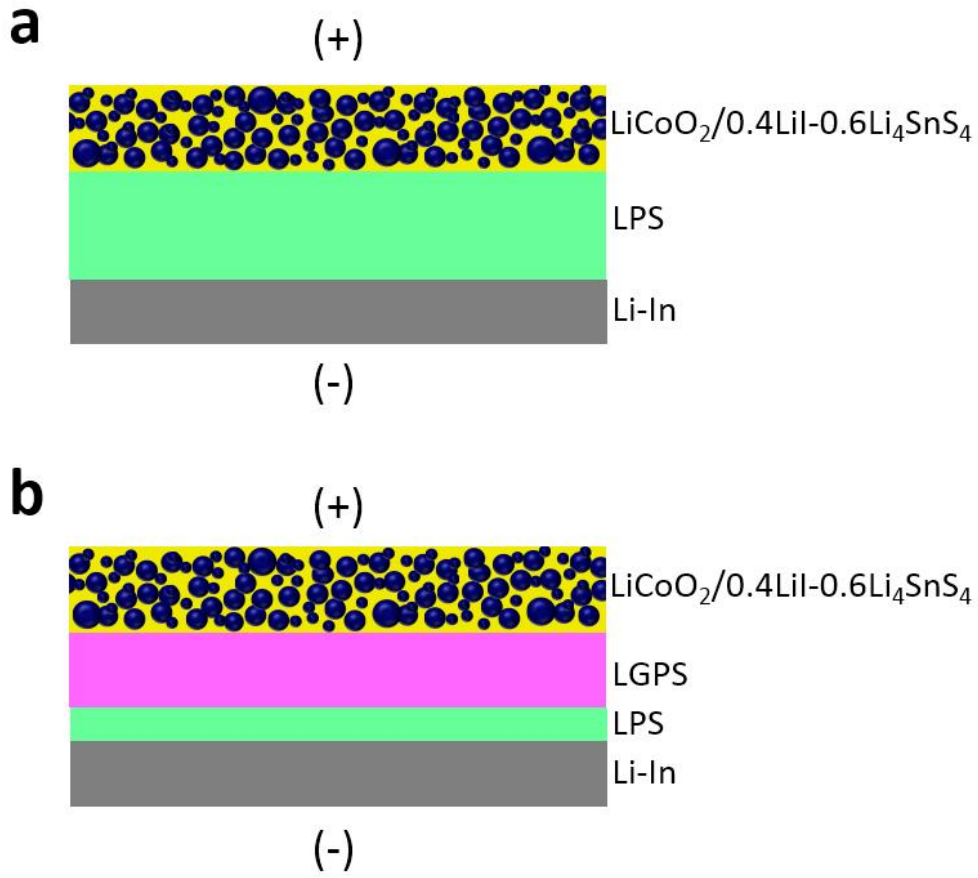

Figure 23. Schematic diagram of $LiCoO_2$/Li-In cells with different SE layers. a), $LiCoO_2$/LPS/Li-In cells and b)$LiCoO_2$/(LGPS/LPS)Li-in cells. The $LiCoO_2$ electrodes are either the mixture electrode or the $0.4LiI\text{-}0.6Li_4SnS_4$-coated $LiCoO_2$ electrode. Note the resistances of LPS layer in a) and LGPS/LPS bilayer in b) are ~54 Ω and ~13 Ω, respectively.

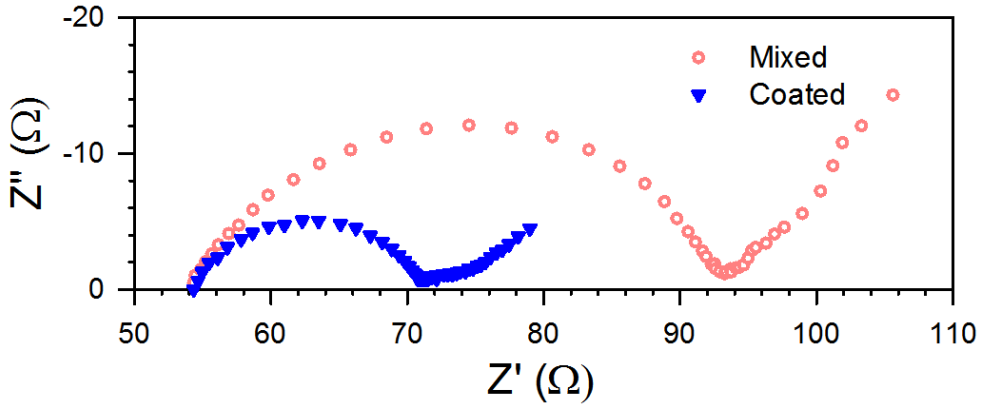

Figure 24. Nyquist plots for $LiCoO_2$/LPS/Li-In cells.

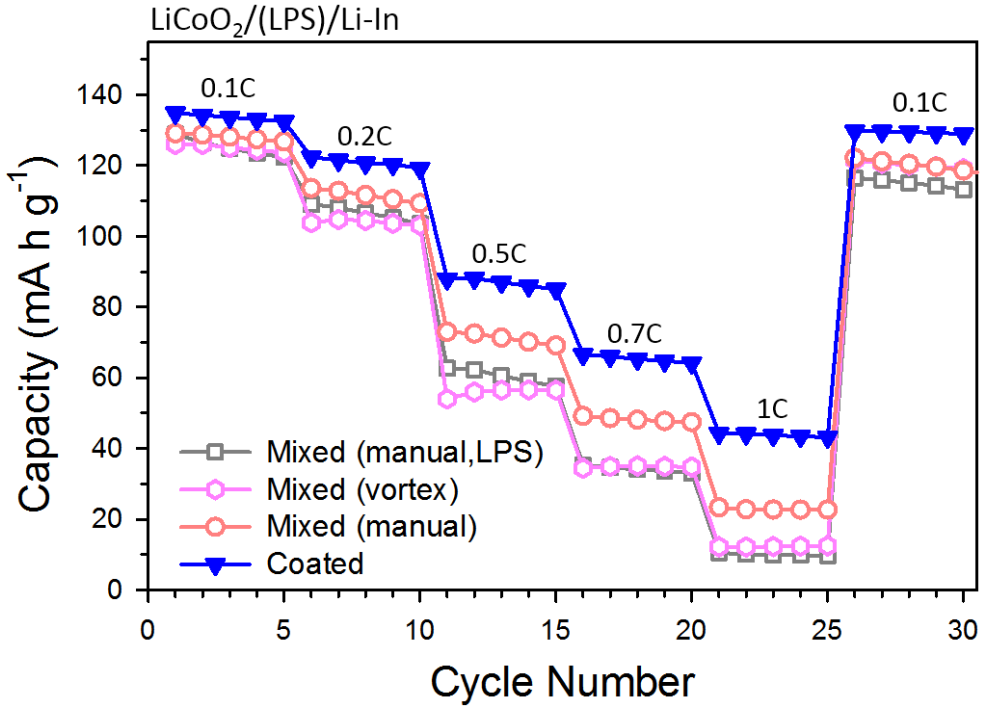

Figure 25. Rate capabilities of $LiCoO_2$/LPS/Li-In cells. Two mixture electrodes, one prepared by manual mixing and one using a vortex mixer, are compared.

the discharge capacities varied by the current densities for $LiCoO_2$/LPS/Li-In cells. Consistent with the EIS results in Figure 24, a pronounced improvement in the rate capability for the SE-coated $LiCoO_2$ electrode over the mixture electrode is observed. The performance of the mixture electrode is affected by mixing conditions. The mixture electrode obtained using a vortex mixer shows even inferior performance compared to the manually mixed electrode. This result indicates that the use of SE-coated active materials can lessen the need of process control for mixing during electrode fabrication. Considering the higher conductivity of LPS (1.0×10^{-3} S cm^{-1}) than that of 0.4LiI-0.6LSS-200 (4.1×10^{-4} S cm^{-1}), the poor performance of the $LiCoO_2$/LPS mixture electrode (open square) implies the importance of ionic contacts (and deformability) over conductivity on the overall performance of bulk-type ASLBs. When the LPS/LGPS bilayer having lower resistance (~13 Ω, LGPS: 6.0×10^{-3} S cm^{-1}) replaces the LPS SE layer (~54 Ω) (Configuration is depicted in Figure 23b.), a more dramatic improvement of the SE-coated $LiCoO_2$ electrode over the mixture electrode is achieved (Figure 26). The SE-coated $LiCoO_2$ electrode shows the capacity retention of 83.3% at 1C (113 mA h g^{-1}) as compared to the capacity at 0.1C (135 mA h g^{-1}) while the mixture electrode shows only 46.0% (60 mA h g^{-1}). In the discharge voltage profiles for the $LiCoO_2$/(LPS/LGPS)/Li-In cells in Figure 27, the SE-coated $LiCoO_2$ electrode shows a much lower polarization and the resulting higher capacities compared to the mixture electrode. Moreover, the 0.4LiI-0.6LSS-coated $LiCoO_2$ electrode also outperforms the $LiCoO_2$/LGPS mixture electrode (Figure 26). This result is surprising in that the conductivity of LGPS (6.0×10^{-3} S cm^{-1}) is more than one order

of magnitude higher than that for 0.4LiI-0.6LSS

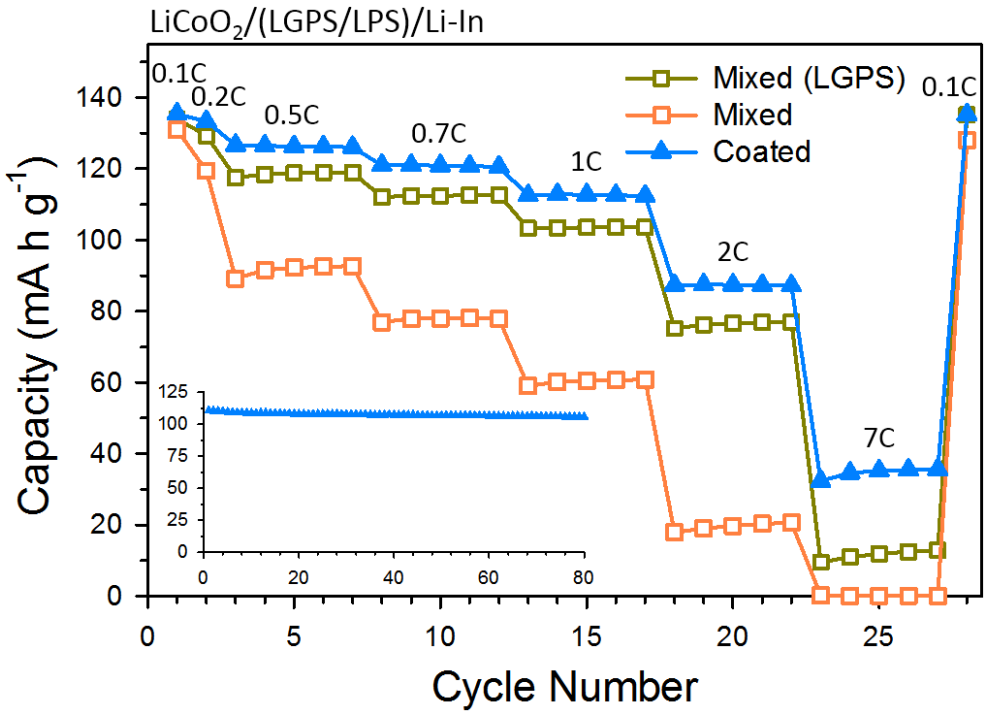

Figure 26. Rate capabilities of $LiCoO_2$/(LGPS/LPS)/Li-In cells. The LGPS/$LiCoO_2$ mixture electrode are shown for comparison. Cycle performance at 1 C for the 0.4LiI-0.6LSS-coated $LiCoO_2$ electrode is shown in the inset.

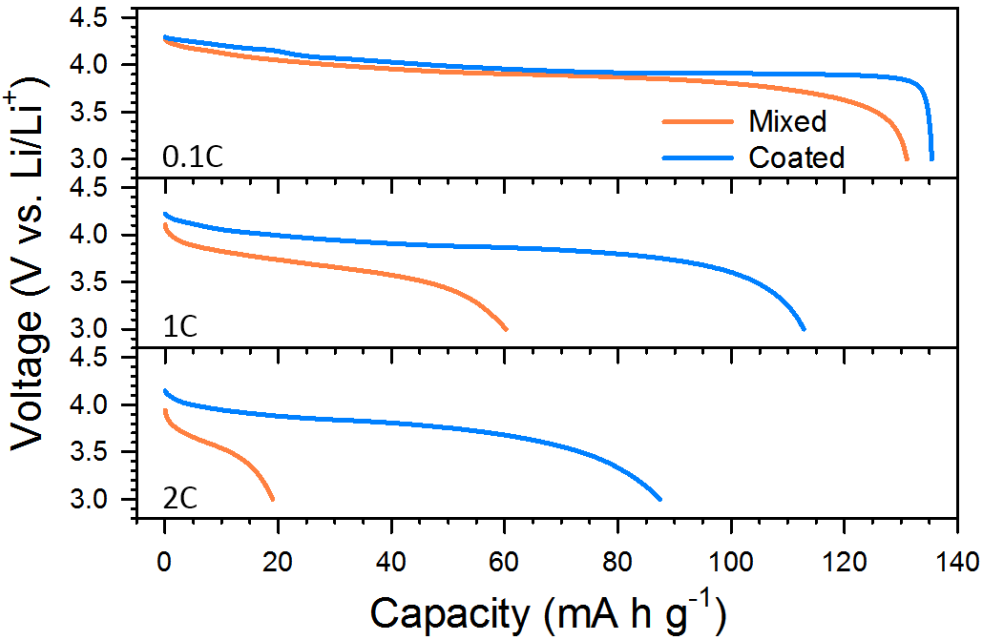

Figure 27. Discharge voltage profiles for $LiCoO_2$/(LGPS/LPS)/Li-In cell. 0.4LiI-0.6LSS-mixed and coated electrode are compared.

(4.1×10^{-4} S cm^{-1}), which again highlights the decisive role of intimate ionic contacts over ionic conductivity on the overall performance of bulk-type ASLBs. Further optimization of the rate performance would be possible by a combination of 0.4LiI-0.6LSS-coated $LiCoO_2$ and LGPS powders, which can synergize the intimate ionic contacts by the 0.4LiI-0.6LSS coating and the extremely fast ionic transport through the LGPS. This strategy will be next mission. As shown in the inset in Figure 26, the 0.4LiI-0.6LSS-coated $LiCoO_2$ electrode cycled at 1C also exhibits the excellent cycleability (Capacity retention of 95.7% after 80 cycles).

Finally, the galvanostatic intermittent titration technique (GITT) was employed to track the polarization.[118] Transient voltage profiles and polarization curves for $LiCoO_2$/LPS/Li-In cells are plotted in Figure 28. The whole range shows a higher polarization for the mixture electrode than that for the SE-coated $LiCoO_2$ electrode. Moreover, the interfacial contact areas between $LiCoO_2$ and the SEs were extracted by analysing the transient voltage profiles (Figures 28).[119] Interfacial contact area between $LiCoO_2$ and SE particles (S) are calculated by using the following equation for the transient voltage profile obtained by the GITT experiment.[119]

$$D = \frac{4}{\pi\tau}\left(\frac{m_{\mathrm{LCO}}V_{\mathrm{M}}}{M_{\mathrm{LCO}}S}\right)^2\left(\frac{\Delta E_{\mathrm{s}}}{\Delta E_{\mathrm{t}}}\right)^2$$

where D: chemical diffusion coefficient, S: contact area between electrolyte and sample = interfacial contact area, τ: pulse duration (60 s), ΔE_s : steady-state voltage

change, ΔE_t : transient voltage change, M_{LCO} : molecular weight of the host, CoO_2 (90.942 g mol^{-1}), m_{LCO} : mass of the host, CoO_2, in the sample (11.8 mg), V_M : molar volume of the sample ($LiCoO_2$, 19.56 cm^3 mol^{-1}). The chemical diffusion coefficient (D) of 4.0×10^{-12} cm^2 s^{-1} for $LiCoO_2$[120] was used. Notably, the surface coverage of SEs over the $LiCoO_2$ in the SE-coated $LiCoO_2$ electrode (81%) turns out to be 2.6 times higher than that in the mixture electrode (31%). Figure 29 shows schematic diagrams illustrating the uneven spatial distribution of SEs and the poor ionic contacts in the mixture electrode as compared to the SE-coated $LiCoO_2$ electrode, which is confirmed by the surface images of electrodes (Figure 21) and the porosity values (7% for the SE-coated $LiCoO_2$ electrode and 12% for the mixture electrode). These features are responsible for the resulting electrochemical behaviours shown in Figure 24-28. The improved performance by solution-processed coating on active materials was also demonstrated for Li_4SnS_4-coated $Li_4Ti_5O_{12}$ as the anode material (Figure 30). A 2.7 *wt*% coating of Li_4SnS_4 on $Li_4Ti_5O_{12}$ resulted in increase in the reversible capacity at 0.2C from 90 mA h g^{-1} to 140 mA h g^{-1}. Overall, all the electrochemical results unequivocally demonstrate the superiority of the electrode fabricated from the SE-coated active materials over the mixture electrode, thus revealing the importance of intimate ionic contacts in bulk-type ASLBs. Practical bulk-type ASLBs would require the inclusion of organic components, such as polymeric binders[121,122] and nonwoven scaffolds[38], that provide flexibility and/or better adhesion. However, ionic blockage by those organic components would result in a significant trade-off in the rate performance. The direct ionic contact between active materials and highly conductive

$0.4LiI\text{-}0.6Li_4SnS_4$ is thus expected to considerably

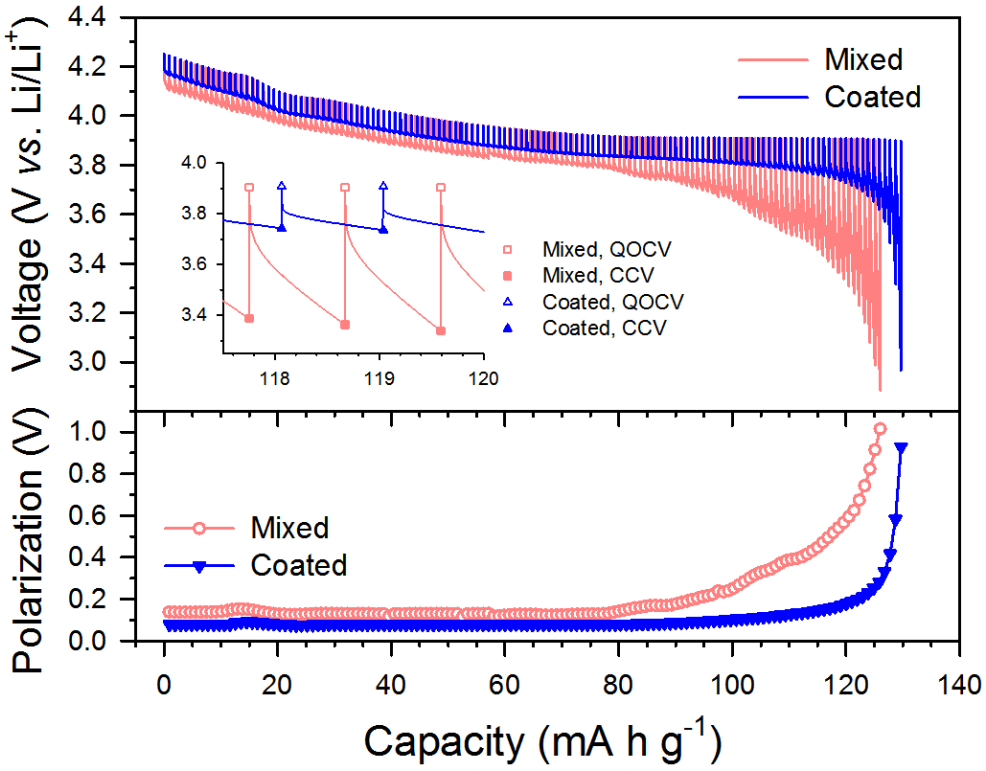

Figure 28. Transient discharge voltage profiles and their corresponding polarization plots obtained by GITT for $LiCoO_2$/LPS/Li-In cell. The enlarged view is shown in the inset. The polarization curves were plotted by subtracting CCV from QOCV in the transient voltage profiles. The $LiCoO_2$:SE weight ratio was 85:15

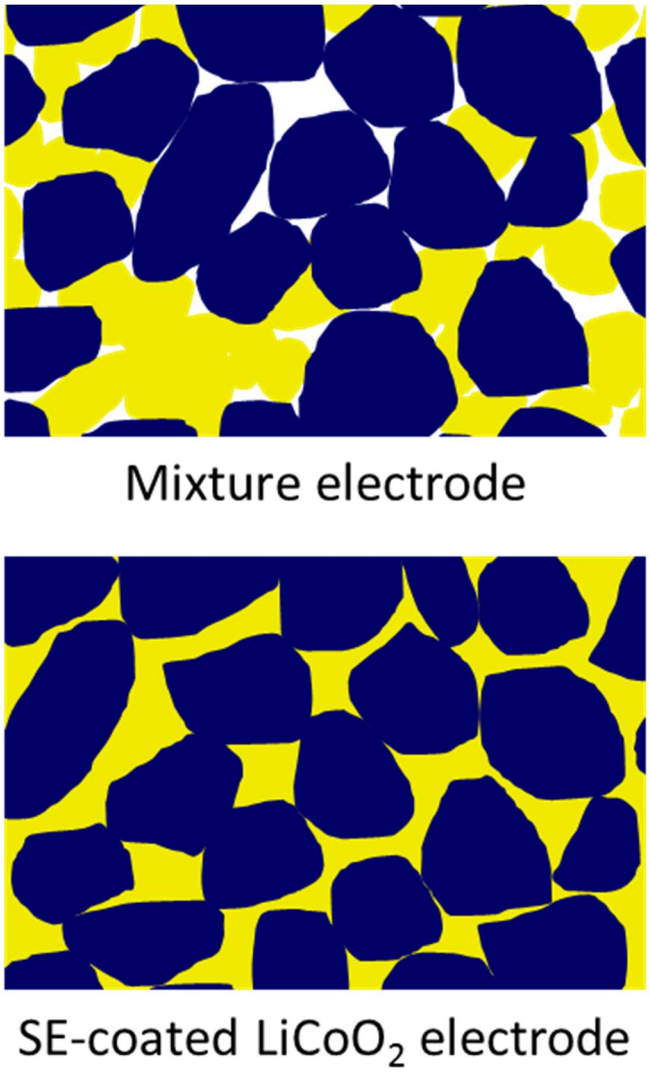

Figure 29. Schematic illustration of the mixture electrode and the 0.4LiI-0.6Li_4SnS_4-coated $LiCoO_2$ electrode. The dark blue and yellow regions indicate $LiCoO_2$ and SE, respectively.

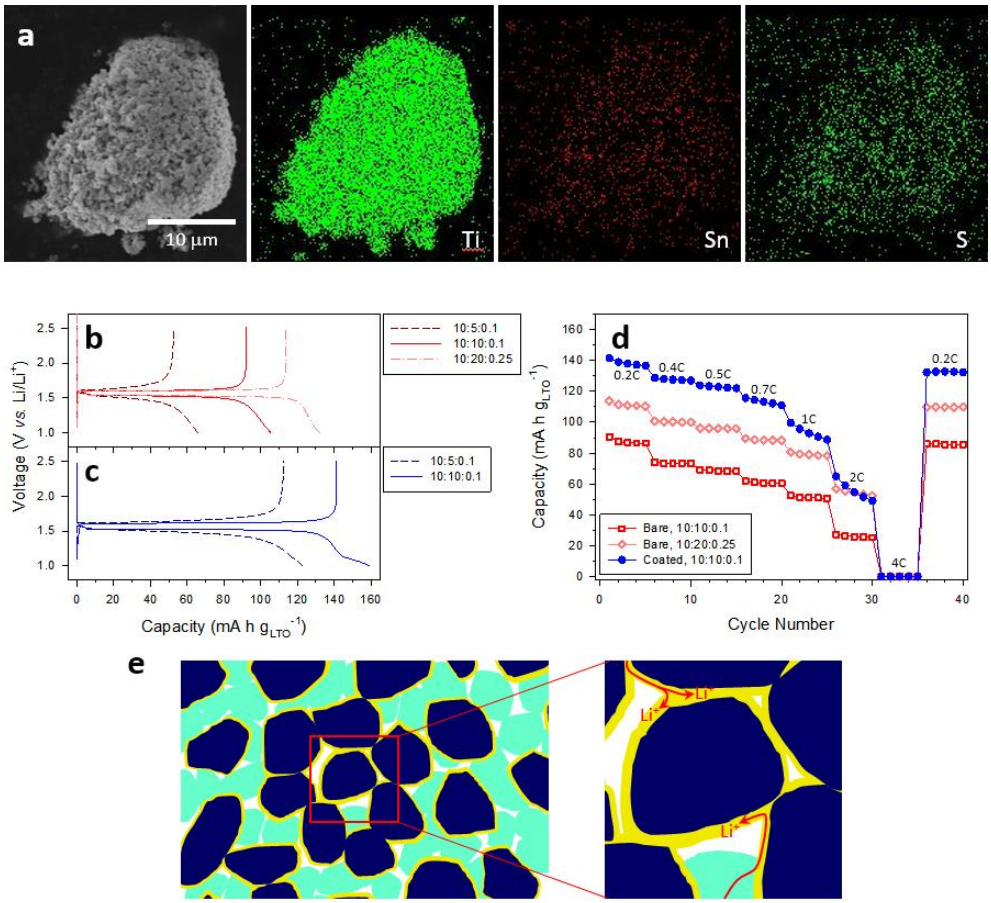

Figure 30. Results of Li_4SnS_4-coated $Li_4Ti_5O_{12}$. a) FESEM image and its corresponding EDXS elemental maps for $Li_4Ti_5O_{12}$ powders coated with 2.7 *wt*% Li_4SnS_4. The Li_4SnS_4 coating was performed using the MeOH solution process similar to the case for the $0.4LiI\text{-}0.6Li_4SnS_4$-coated $LiCoO_2$. The HT temperature was 200°C. Charge–discharge voltage profiles of $Li_4Ti_5O_{12}$/LPS/Li-In cells where composite electrode was prepared by mixing LPS with b) bare and c) Li_4SnS_4-coated $Li_4Ti_5O_{12}$ powders. The weight ratios of $Li_4Ti_5O_{12}$:SE:super P are shown. d) Rate capabilities of $Li_4Ti_5O_{12}$/LPS/Li-In cells. The 1C corresponds with 1.3 mA cm^{-2}. e) Schematic diagram showing composite electrode made by mixing Li_4SnS_4-coated $Li_4Ti_5O_{12}$ powders with LPS powders. The dark blue, yellow, and bright green regions indicate $Li_4Ti_5O_{12}$, Li_4SnS_4, and LPS, respectively. Carbon additives are not represented in the scheme. Note the favourable ionic conduction pathways facilitated by the Li_4SnS_4 coating layer.

affect the performance of practical bulk-type ASLBs.

Finally, the dry-air-stability of 0.4LiI-0.6Li_4SnS_4 was tested. The conductivity after exposing the 0.4LiI-0.6Li_4SnS_4 powders to dry air for 24 h at 30°C was still high (from 4.1×10-4 S cm^{-1} to 2.6×10-^{4} S cm^{-1}). This is in sharp contrast to the LPS powders, whose conductivity decreased by more than two orders of magnitude (from 1.0×10^{-3} S cm^{-1} to 8.0×10^{-6} S cm^{-1}) (Figure 31). The changes in the electrochemical performances of $LiCoO_2$/LPS/Li-In cells fabricated from the LPS/$LiCoO_2$ mixture electrodes and the 0.4LiI-0.6Li_4SnS_4-coated $LiCoO_2$ electrodes before and after exposure to dry air for 24 h at 30°C are also compared. When cycled at 0.11 mA cm^{-2} (0.1C), after exposure to dry air, the 0.4LiI-0.6Li_4SnS_4-coated $LiCoO_2$ electrode shows negligible decrease in capacity, whereas the LPS/$LiCoO_2$ mixture electrode exhibits significantly increased polarization and decreased capacity (Figure 32a, b), indicating that the solution-processable LiI-Li_4SnS_4 has potential compatibility with practical applications.[123] The inertness of 0.4LiI-0.6Li_4SnS_4 against dry air is confirmed by the negligible change in the Sn K-edge EXAFS signature (Figure 32c). The excellent stability of 0.4LiI-0.6Li_4SnS_4 is in line with the results of previous works for As-substituted Li_4SnS_4[22] and Li_2SnS_3,[124] and is explained by adopting the hard and soft acid and base (HSAB) theory.[22,35] The soft acid, Sn, is less vulnerable toward attack by the hard base, O, than the hard acid, P.

Similar to the case of LGPS, one drawback of Li_4SnS_4-based SEs is their poor reduction stability at <1 V (*vs*. Li/Li^+) because Sn acts as a reducing centre.[54,76,125] However, it does not neutralize the promising advantages of LiI-Li_4SnS_4. In contrast to

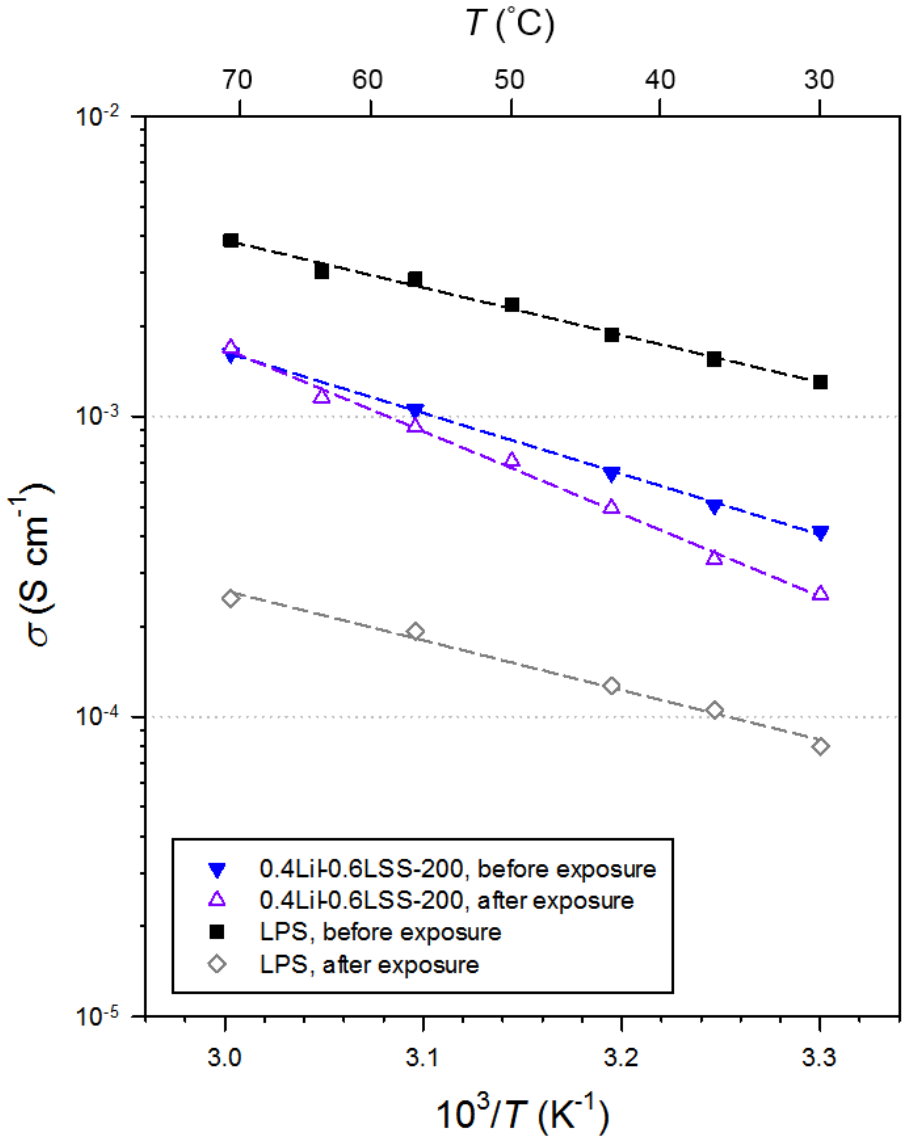

Figure 31. Air stability of 0.4LiI-0.6Li_4SnS_4 *vs*. LPS. Arrhenius plots for 0.4LiI-0.6Li_4SnS_4 *vs*. LPS before and after exposure to dry air. The conductivity was measured by using the c-Al/SE/c-Al cells in which the pristine or dry-air-exposed SE powders were used. The SE powders were exposed to flowing dry air at room temperature for 24 h.

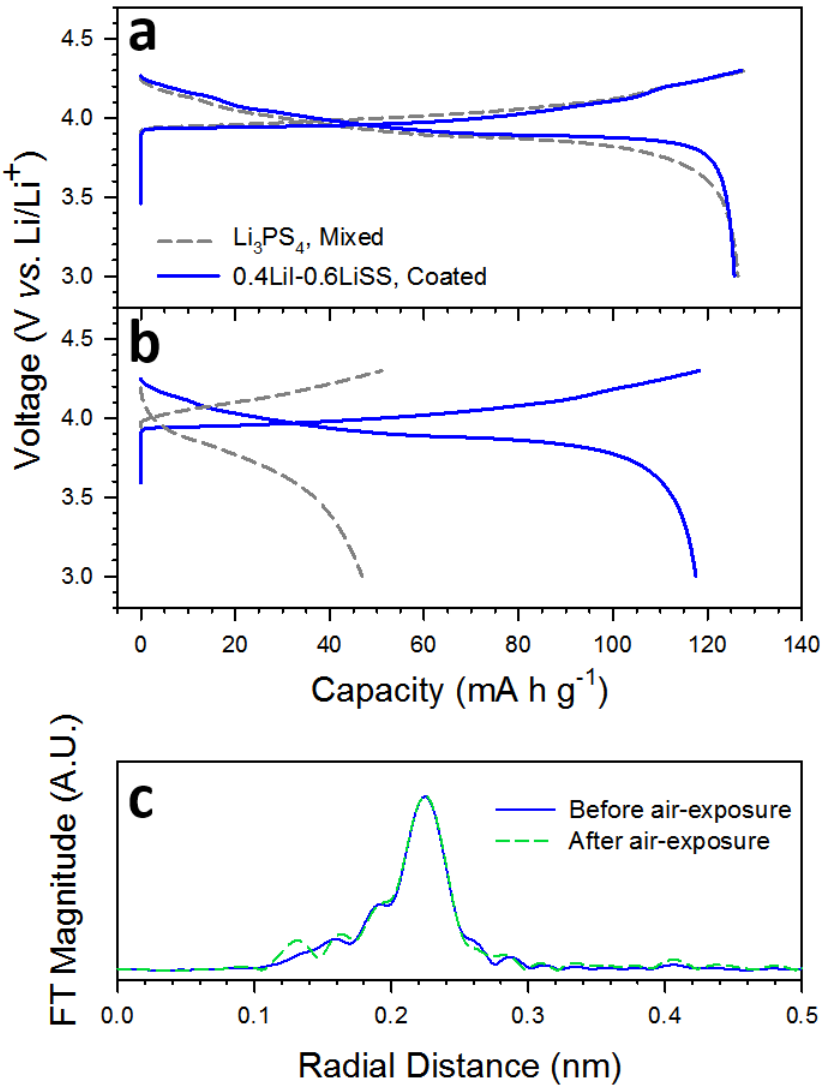

Figure 32. Dry-air stability of $0.4LiI\text{-}0.6Li_4SnS_4$. Voltage profiles of $LiCoO_2$/LPS/Li-In cells in which the $LiCoO_2$ composite electrodes are the LPS/$LiCoO_2$ mixture electrode or the $0.4LiI\text{-}0.6Li_4SnS_4$-coated $LiCoO_2$ electrode a) before and b) after exposure of the LPS powders and the $0.4LiI\text{-}0.6Li_4SnS_4$-coated $LiCoO_2$ powders to dry air for 24 h. The C-rate was 0.1 C (0.11 mA cm^{-2}). C) Sn K-edge EXAFS spectra for $0.4LiI\text{-}0.6Li_4SnS_4$-coated $LiCoO_2$ powders before and after exposure to dry air. The $LiCoO_2$:SE weight ratio was 85:15.

conventional LIBs using a single liquid electrolyte, configuring with more than one SE is a significant benefit for ASLBs. For example, $3LiBH_4 \cdot LiI$-coated As-substituted Li_4SnS_4 is operable with Li metal,[22] and TiS_2/(LGPS/LPS)/Li-In cell maximizes the rate capability with retaining reversibility.[38,76] The latter is also the case for the results of (0.4LiI-0.6LSS-coated $LiCoO_2$)/(LGPS/LPS)/Li-In cell shown in Figure 23, 26, 27.

4.2. Na_3SbS_4: Sodium Ionic Conductor

4.2.1. Properties of Na_3SbS_4

For the solid-state synthesis, Na_3SbS_4 powders were prepared from a stoichiometric mixture of Na_2S, Sb_2S_3, and sulfur powders at 550°C. Figure 33a represents the powder X-ray Rietveld refinement profile for Na_3SbS_4. All the peaks could be indexed with the tetragonal structure [a = 7.1453 Å and c = 7.2770 Å, Z = 2, P-421c (no.114), (Table 2)] without any noticeable impurities, which is isostructural with tetragonal Na_3PS_4[126] and slightly elongated from previously reported cubic Na_3SbS_4.[127] The unit cell structure consists of a body-centered-tetragonal sublattice of SbS_4^{3-} tetrahedra that are connected to neighboring tetrahedra via the sodium ions (Figure 33b, 34). The presence of SbS_4^{3-} was also confirmed from three distinct peaks in the Raman spectrum (Figure 35).[128] In the [010] view (Figure 33b), Na-ion diffusion channels are apparently seen perpendicular to the plane. It should be noted that such channels exist parallel to all three crystallographic axes (Figure 33b, 34a,b) to form orthogonal 3D networks (Figure 34c). For a better understanding of the Na-ion conduction pathways of Na_3SbS_4, the bond valence sum mapping (BVSM) method was utilized.[129] Figure 33c shows the BVS isosurfaces at ±0.3 v.u., clearly demonstrating the 3D network of the Na-ion conduction pathways along the a- (or b-) and c-axes, which implies the high ionic conductivity of Na_3SbS_4. It is also noted that the channels appear to have a bottleneck

along the c-axis,

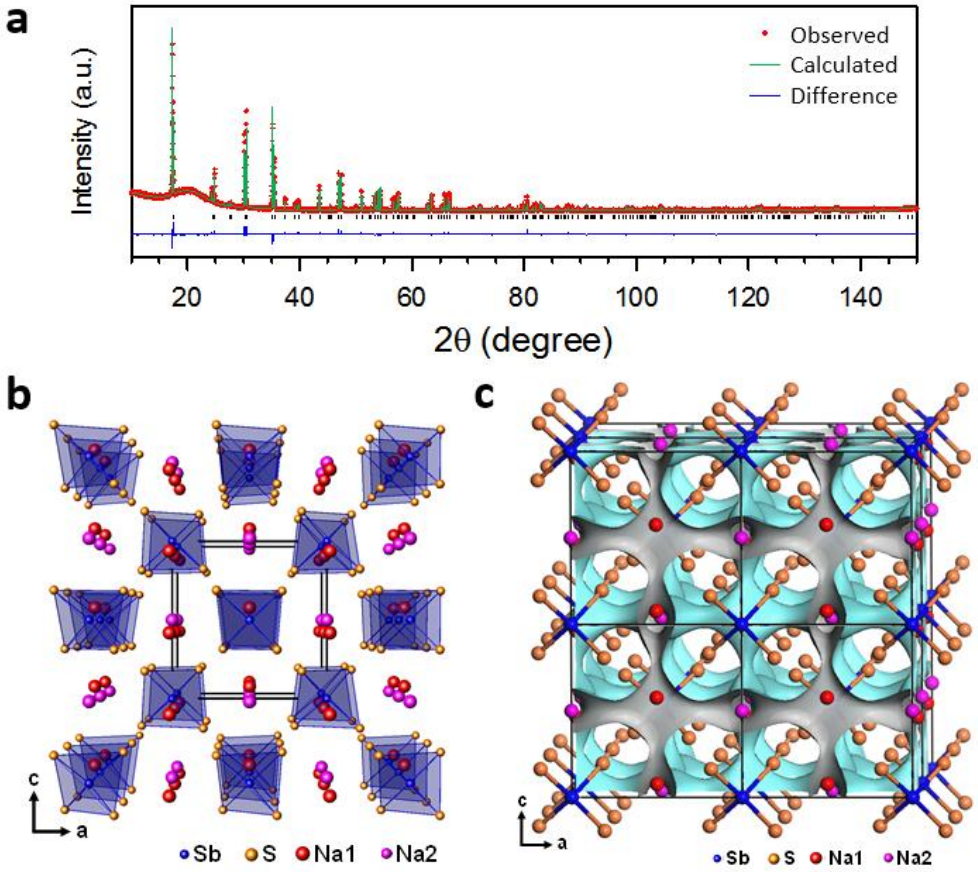

Figure 33. Structural analysis results of Na_3SbS_4. a) X-ray Rietveld refinement profile for the Na_3SbS_4 powders recorded at room temperature. b) Crystal structure of Na_3SbS_4 with the unit cell outlines. c) 3D bond valence map isosurfaces for Na_3SbS_4 with an isovalue of ± v.u.

Table 2. Crystallographic data and Rietveld refinement results for Na3SbS4 by powder XRD data: Atomic coordinates, Site Occupancies, Displacement Parameters ($Å^2 \times 10^2$) and Reliability Factors at Room Temperature.

Crystal System				Tetragonal		
Space Group				P -4 2_1 C (no. 114)		
Lattice Parameter, Volume, Z				a = 7.14524(3) Å, c = 7.27695(5) Å V = 371.52(1) $Å^3$, *Z* = 2		
Atoms	x	Y	z	Wyckoff	Occupancy	U_{iso}
Sb	0	0	0	2a	1.0	0.4
S	0.2954(4)	0.3292(4)	0.6802(4)	8e	1.0	1.4
Na1	0	0.5	0.4250(8)	4d	1.0	2.6
Na2	0	0	0.5	2b	1.0	2.5
	U11	U22	U33	U12	U13	U23
Sb	0.32(4)	0.35(4)	0.47(6)	0.0	0.0	0.0
S	1.7(2)	0.91(2)	1.76(19)	0.0(1)	0.25(17)	0.17(17)
Na1	2.0(4)	1.2(4)	4.5(4)	-0.1(6)	0.0	0.0
Na2	3.0(3)	3.0(3)	1.7(4)	0.0	0.0	0.0

*R_p = 0.083, R_{wp} = 0.125, R_{exp} = 0.093, $R(F^2)$ = 0.23284, χ^2 = 1.823, $U_{iso} = (U_{11} + U_{22} + U_{33}) / 3$.

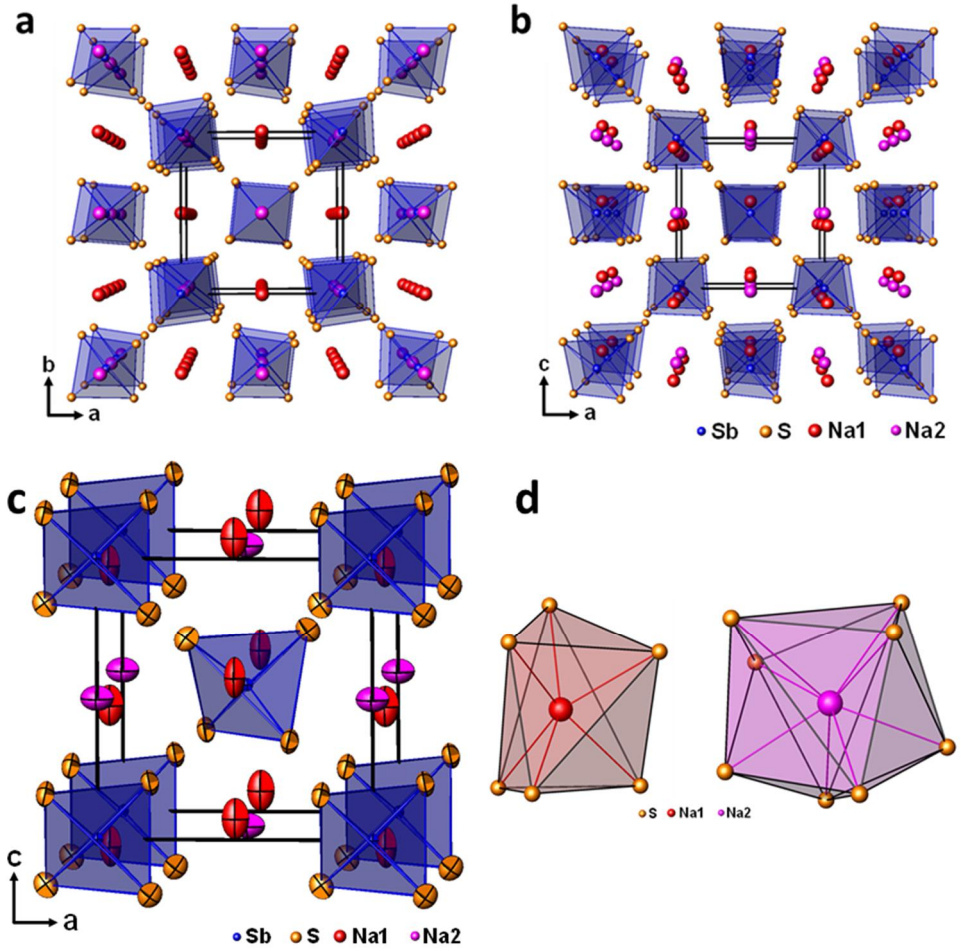

Figure 34. Crystal structure of Na_3SbS_4 viewed along a) [001] and b) [010] orientation. c) Unit cell structure with displacement ellipsoids drawn at the 90% probability level. d) The local environment around the Na atoms in Na_3SbS_4. The six-fold coordination of Na1, and the eight-fold coordination of Na2.

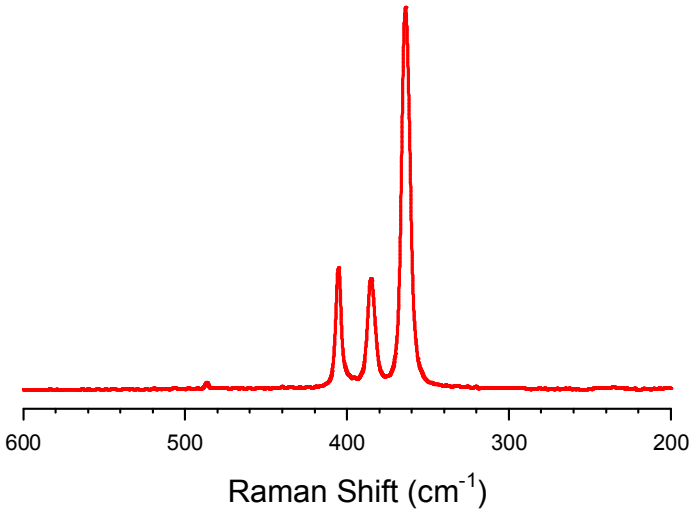

Figure 35. Raman spectra of Na_3SbS_4.

as indicated by the narrower isosurfaces between the Na ions than in the a–b, which might reflect the preferential 2D conduction.

The electronic conductivity of Na_3SbS_4 measured by the four probe method[95] was less than 10^{-8} S cm^{-1}. The electrical conductivity of Na_3SbS_4 measured by the AC method using Na-ion blocking cells, which is in turn interpreted as ionic conductivity, is shown in Figure 36 and Table 3. The conductivity value of 1.1×10^{-3} S cm^{-1} at 25°C and an activation energy of 0.20 eV for tetragonal Na_3SbS_4 is comparable to that for cubic Na_3PSe_4, which was the best result.[51] First, the high conductivity of Na_3SbS_4 is attributed to the open framework with 3D Na-ion channels (Figure 33b, 33c,34a,b).[130] Second, a trace amount of Na vacancies may also contribute to the high conductivity of Na_3SbS_4, although precise determination of the amount was beyond the experimental limits of X-ray refinement.[52]

The dry-air stability of Na_3SbS_4 was tested by exposing the SE powders to a flow of dry air for 24 h. After the exposure, only marginal degradation in conductivity and the same activation energy were observed (Figure 36). Also, the XRD pattern of Na_3SbS_4 after dry-air exposure did not differ from that before exposure (Figure 37a), indicating its good stability. In sharp contrast, the XRD pattern for NPS (Na_3PS_4) showed a noticeable unknown broad peak (‘*’ in Figure 37b) after dry-air exposure. Accordingly, the conductivity value decreased by approximately one order of magnitude (from 1.1×10^{-4} S cm^{-1} to 2.0×10^{-5} S cm^{-1}), confirming the instability of NPS in dry air. By adopting the hard and soft acid and base (HSAB) theory, Sb, which is a softer acid than P, likely has less affinity with the hard base, O, which explains far superior stability of

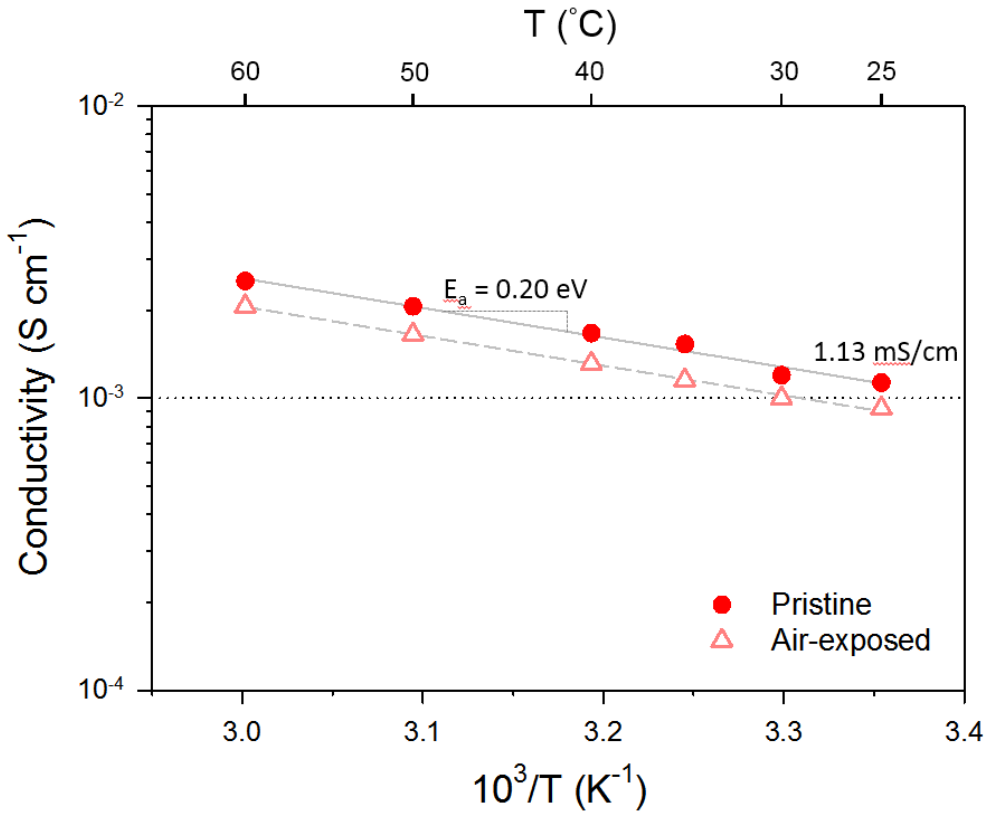

Figure 36. Conductivity of Na_3SbS_4 prepared by solid-state reaction at 550°C. Data after exposure to dry air for 24 h is also compared.

Table 3. Conductivity and activation energy values for Na_3SbS_4 prepared by solid-state reaction and the solution process using MeOH or H_2O.

Sample	Preparation	Temperature (°C)	σ (mS cm^{-1})	E_a (eV)
Na_3SbS_4	Solid-state	550	1.1	0.20
NSbS-M100	MeOH	100	0.23	0.37
NSbS-M200	MeOH	200	0.11	0.38
NsbS-W100	H2O	100	0.26	0.32
NSbS-W200	H2O	200	0.15	0.30

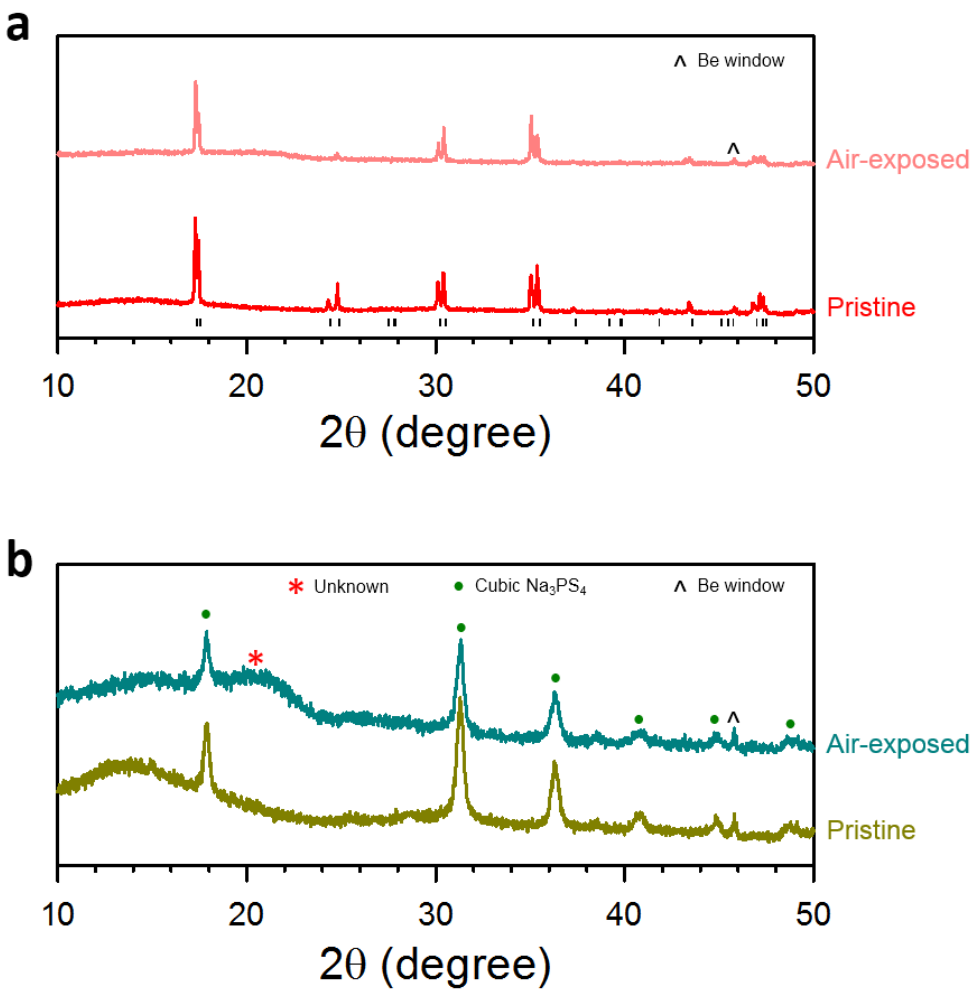

Figure 37. XRD patterns of a) Na_3SbS_4 and b) Na_3PS_4 (NPS) before and after dry-air exposure. The Bragg position for Na_3SbS_4 is marked in a.

Na_3SbS_4 in dry air to NPS.[22,35] However, Na_3SbS_4 appeared to change upon exposure to ambient air for 48 h, forming a hydrated compound ($Na_3SbS_4 \cdot 9H_2O$) (Figure 38). Interestingly, Na_3SbS_4 which showed 3.4×10^{-4} S cm^{-1} was recovered by heat-treatment of the hydrated form under vacuum at 200°C (Figure 38). Na_3SbS_4 also showed moderate stability upon exposure to CO_2 (Figure 39). After exposure to a flow of CO_2 for 24 h, no noticeable change in the XRD pattern (Figure 39b) and only slight decrease in conductivity (8.2×10^{-4} S cm^{-1}) were observed.

Importantly, Na_3SbS_4 showed excellent solubility in water and alcohol, from which solidification of the dissolved solutions has been attempted. After forming yellowish homogeneous solutions by dissolving the Na_3SbS_4 powders in MeOH or water, the solvents were removed by drying under vacuum at room temperature, followed by heat-treatment under vacuum. The results for MeOH and aqueous solution processes are shown in Figure 40 and 41, respectively. Hereafter, the MeOH and aqueous solution-processed samples heat-treated at a temperature of x (°C) are referred to as "NSbS-Mx" and "NSbS-Wx". Considering application of the solution process to SE coating on active materials further, a minimum temperature at which the solvents can be removed would be desirable in order to avoid any reaction between the electrode materials and the coated SEs. From thermogravimetric analysis (TGA) results (Figure 40b and 41b), heat-treatment temperatures of 100, 150, and 200°C were thus selected.

In all solution-processed samples, XRD patterns identical to that for solid-state-synthesized Na_3SbS_4 (Figure 33) with broadened peaks were observed (Figure 40c and 41c). The Raman spectra for the solution-processed samples also clearly showed strong

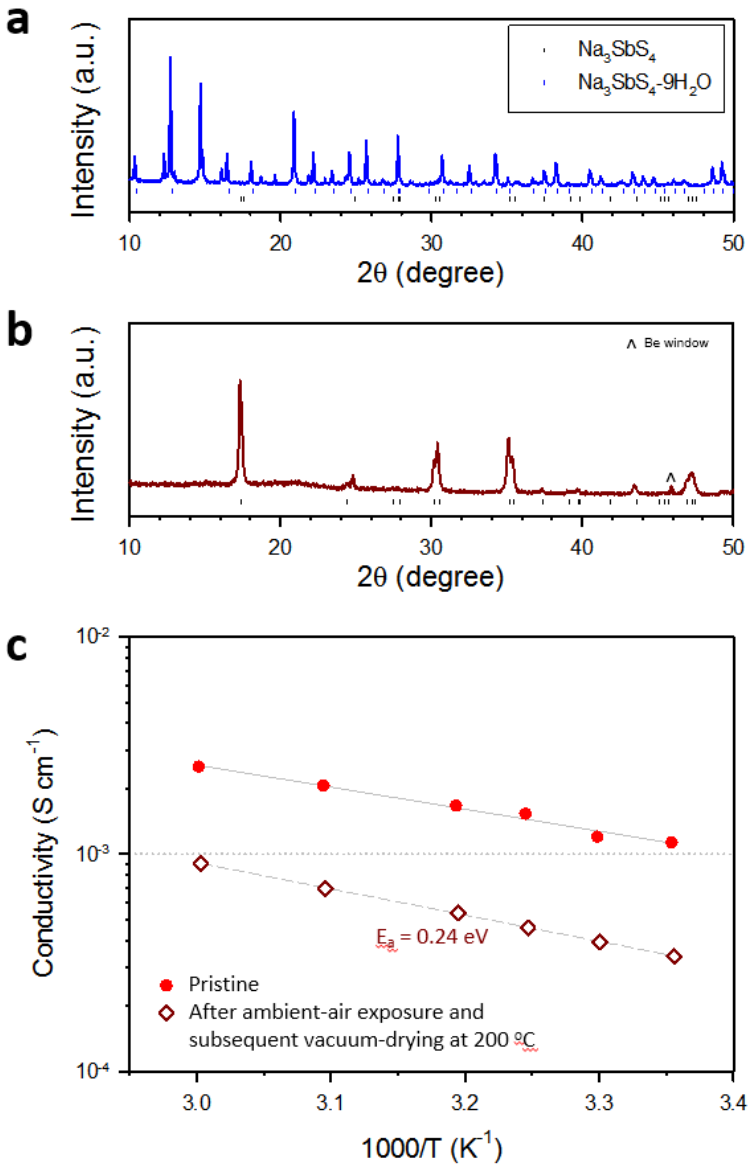

Figure 38. Results of Na_3SbS_4 after exposure to ambient air at room temperature. a) XRD pattern of Na_3SbS_4 powders after exposure to ambient air for 48 h. The relative humidity of ambient air was 35-45%. b) XRD pattern of the ambient-air exposed Na_3SbS_4 powders after heat-treatment at 200°C under vacuum. The Bragg positions for $Na_3SbS_4 \cdot 9H_2O$ (JCPDS no.01-75-1972) and tetragonal Na_3SbS_4 are marked. C) Conductivity of Na_3SbS_4 before and after ambient-air exposure and subsequent drying under vacuum at 200°C.

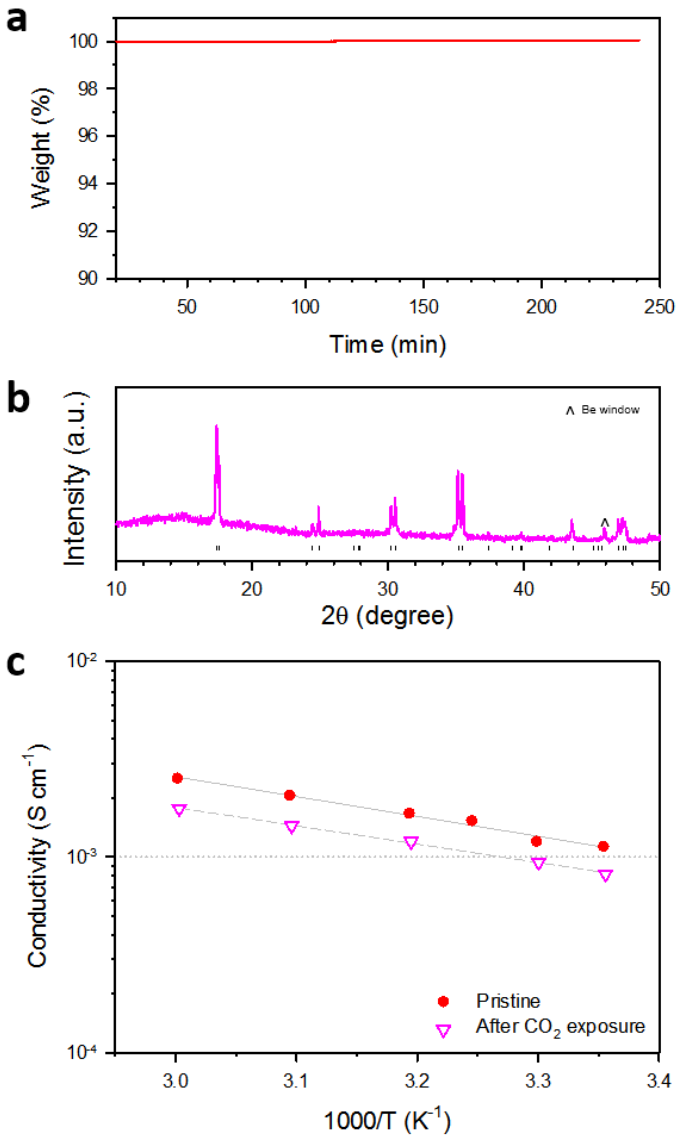

Figure 39. Results of Na_3SbS_4 after exposure to CO_2. a) Transient weight change of Na_3SbS_4 upon exposure to a flow of CO_2. b) XRD pattern of Na_3SbS_4 after exposure to a flow of CO_2 for 24h. The Bragg position for tetragonal Na_3SbS_4 is marked in b. c) Conductivity of Na_3SbS_4 before and after exposure to a flow of CO_2 for 24 h.

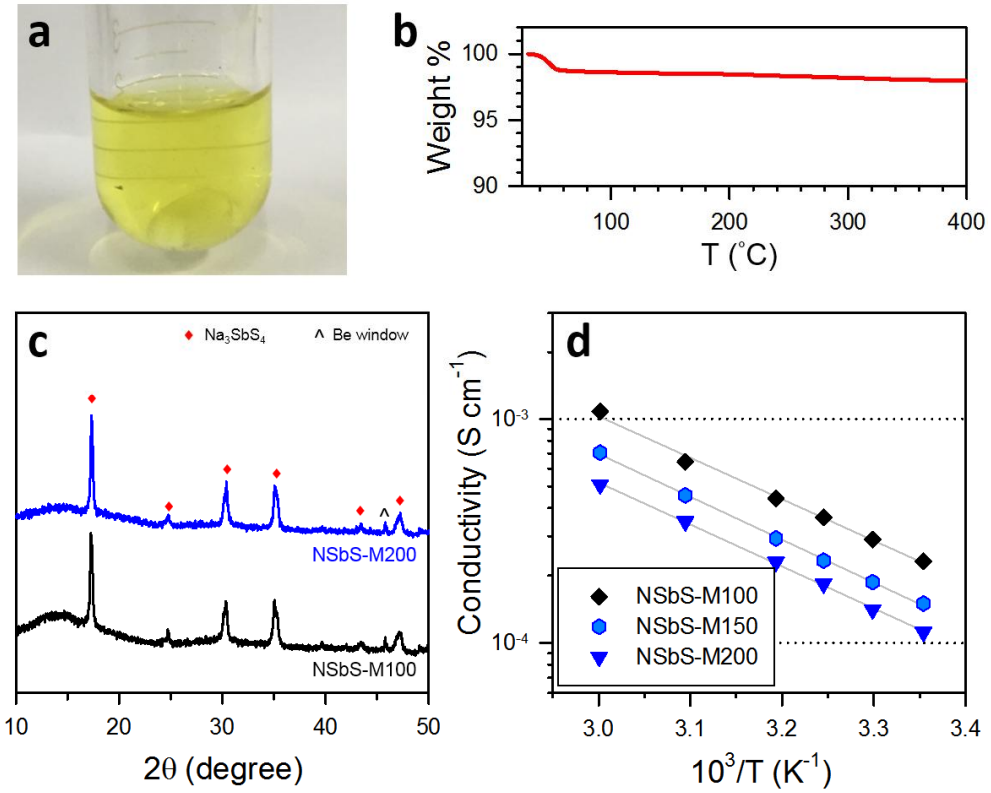

Figure 40. Preparation and characterization of solution Processable Na_3SbS_4. a) Photograph of Na_3SbS_4 dissolved in MeOH solution. b) TGA profile for the $Na_3SbS_4 \cdot xMeOH$ powders obtained by drying under vacuum at room temperature. c) XRD patterns and d) conductivities of Na_3SbS_4 processed in MeOH solution and prepared at different heat-treatment temperatures.

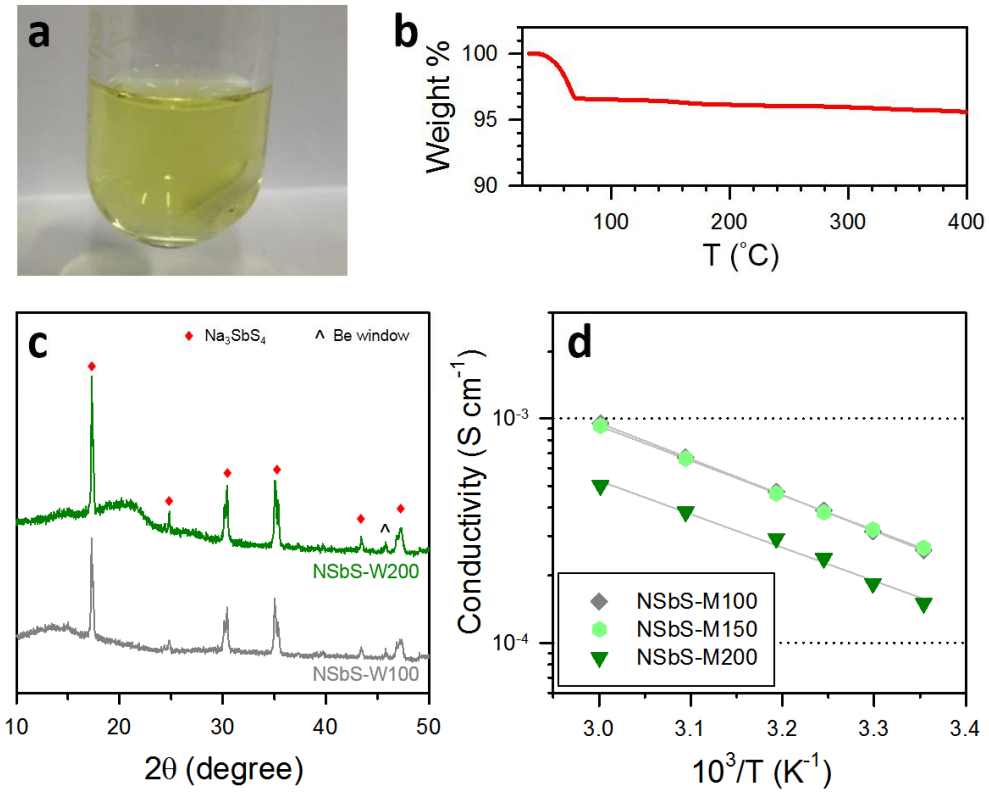

Figure 41. Preparation and characterization of aqueous-solution Processable Na_3SbS_4. a) Photo image of Na_3SbS_4-dissolved aqueous solution. b) TGA profile for the $Na_3SbS_4 \cdot H_2O$ powders obtained by drying under vacuum at room temperature. c) XRD patterns and d) conductivities of solution-processed Na_3SbS_4 prepared at different heat-treatment temperatures.

signatures for SbS_4^{3-} (Figure 42).[128] However, the samples heat-treated at 200°C (NSbS-M200 and NSbS-W200) exhibited additional broad peaks at approximately 320–220 cm^{-1} (Figures 42a,b). This might be related to the formation of trace amounts of surface impurities such as Sb_2S_3 or Sb_2S_5 (Figure 42c).[131,132] Importantly, high conductivity values of 0.1–0.3 mS cm^{-1} were achieved for all MeOH and aqueous solution-processed Na_3SbS_4 (Figure 40d, 41d, Table 3). The lower conductivities and higher activation energies for solution-processed Na_3SbS_4 than for solid-state-synthesized Na_3SbS_4 are the result of the low heat-treatment temperatures, which led to lowered crystallinity and/or to the formation of surface impurities. It is expected that further increases in conductivity may be possible by iso-/aliovalent substitution or by the addition of NaX (X: Cl, Br, I) for both solid-state-synthesized and solution-processable Na_3SbS_4, as demonstrated for Li-ion SE materials such as Li_4SnS_4.[22]

4.2.2. All-Solid-state Sodium Batteries using Na_3SbS_4 Superionic Conductor

A solution-processed coating of highly conductive Na_3SbS_4 was adopted on an electrode material, NCO ($NaCrO_2$). NCO was chosen because of its excellent reversibility for sodiation–desodiation, simple preparation method, and thermal stability.[47,48] NCO showed normal electrochemical behavior in liquid-electrolyte cells.[47,48] The solution-processed coating of Na_3SbS_4 on NCO was carried out by following the same MeOH solution process in the presence of NCO powders at a heat-

treatment temperature of 200°C. The MeOH solution process was applied because NCO is not stable in

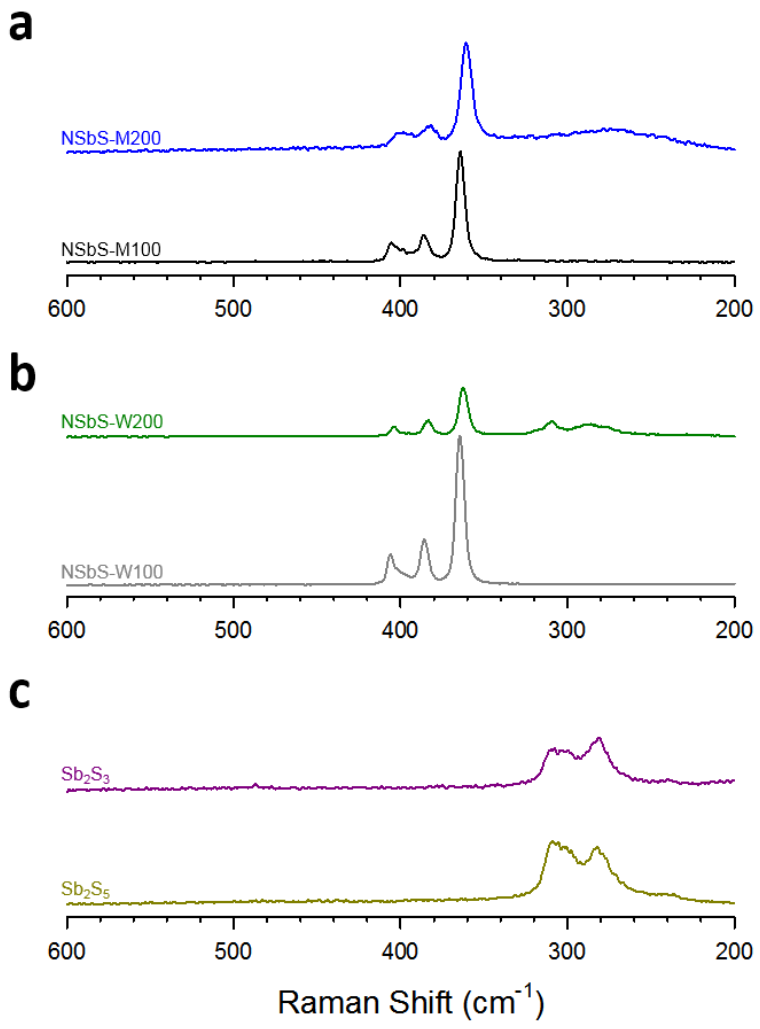

Figure 42. Raman spectra for the solution-processed Na_3SbS_4 by using a) MeOH and b) water. Raman spectra for c) Sb_2S_5 and Sb_2S_3 are shown in c.

water.[47,48,133] Moderate quality of Na_3SbS_4 coating onto NCO is observed by electron microscopy images (Figure 43). In the high-resolution transmission electron microscopy (HRTEM) image of a focused ion beam (FIB) cross-sectioned Na_3SbS_4-coated NCO and its corresponding energy dispersive X-ray spectroscopy (EDXS) elemental maps (Figure 43), an approximately 200-nm-thick coating of Na_3SbS_4 on NCO is clearly seen. Improvement of quality of the Na_3SbS_4 coating in terms of uniformity and surface coverage may be possible by elaborating the experimental conditions for the solution process and/or by applying spray-coating method.[6,97] The selected area electron diffraction (SAED) pattern for the Na_3SbS_4 coating (Figure 44) also agrees well with the XRD results (Figure 40c).

The electrochemical performance of all-solid-state NCO/Na–Sn cells using the as-prepared Na_3SbS_4-coated NCO was compared to that using a conventional mixture electrode. The weight fraction of SE (Na_3SbS_4) was 13 *wt*%. For the mixture electrode, Na_3SbS_4 prepared by solid-state synthesis showing a conductivity of 1.1×10^{-3} S cm^{-1} was used. No carbon additives were included in the electrodes, thus providing a simple system to investigate the effects of the SE coating. Figure 45 displays the initial charge–discharge voltage profiles at 50 μA cm^{-2} at 30°C. The mixture electrode shows a negligible discharge capacity. Increasing an applied pressure for fabricating the cells from 370 MPa to 590 MPa resulted in an increase of discharge capacity from 3 mA h g^{-1} (Figure 45) to 11 mA h g^{-1}, implying the importance of ionic contact. Surprisingly, the Na_3SbS_4-coated NCO shows a discharge capacity of 108 mA h g^{-1}, which is almost the same value as that for the liquid-electrolyte cell. A slight increase in the weight fraction

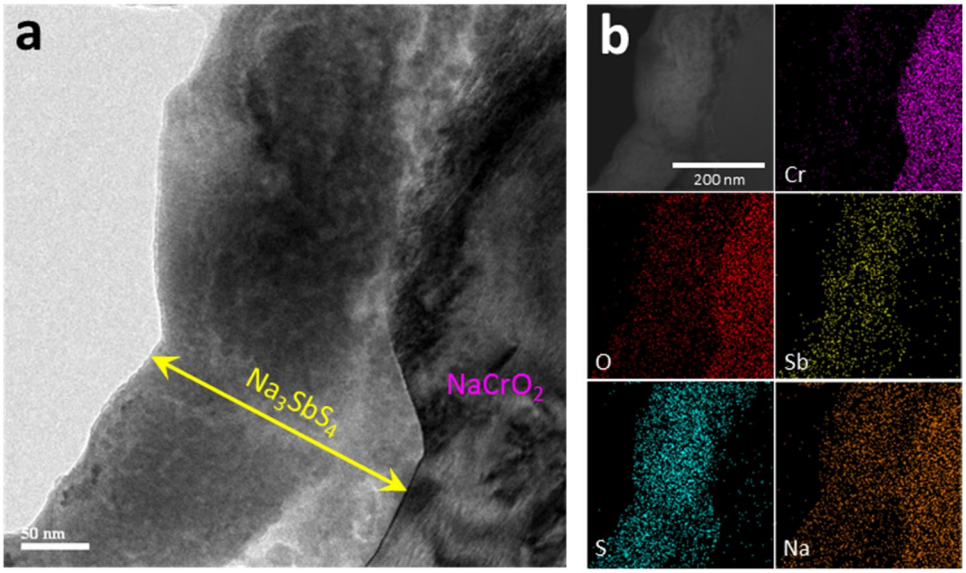

Figure 43. Results of Na_3SbS_4-coated $NaCrO_2$. a) HRTEM image of FIB-sectioned Na_3SbS_4-coated NCO. b) Annular dark-field (ADF) TEM image of FIB-sectioned Na_3SbS_4-coated NCO and its corresponding EDXS elemental maps.

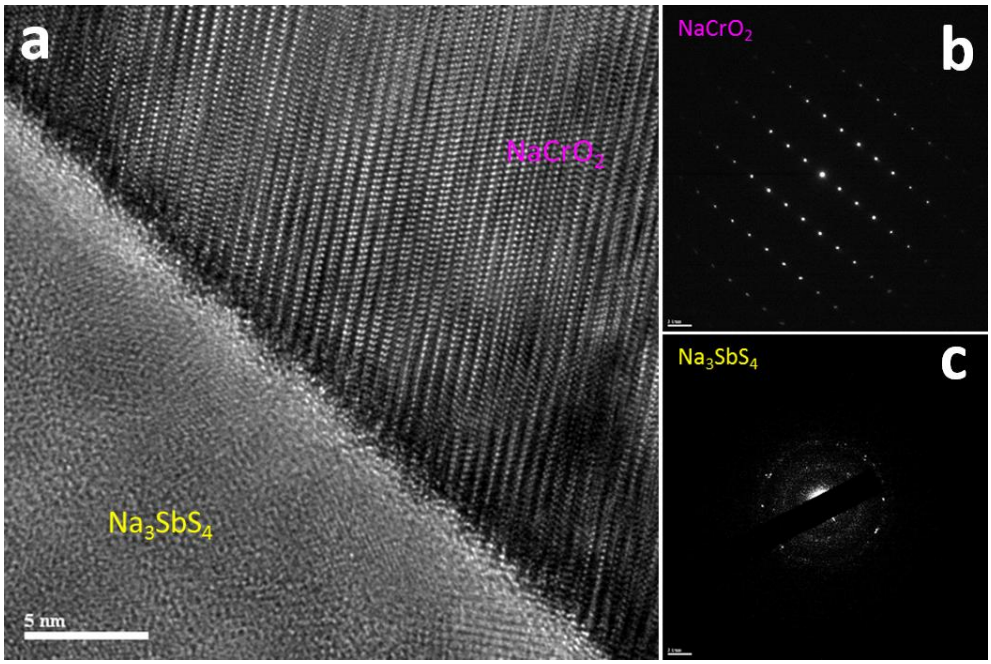

Figure 44. HRTEM image of Na3SbS4-coated $NaCrO_2$ a) and its corresponding SAED patterns for b) $NaCrO_2$ and c) Na_3SbS_4.

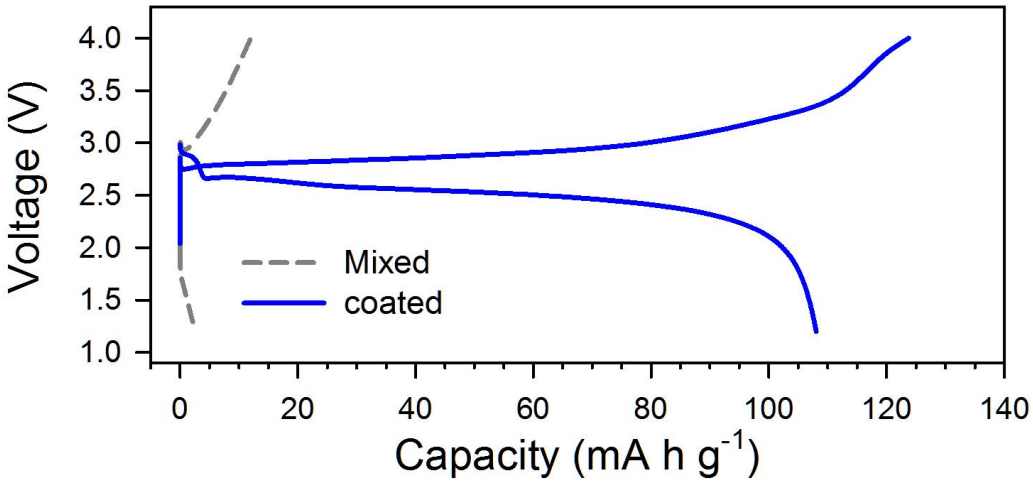

Figure 45. Initial charge-discharge voltage profiles of Na_3SbS_4-coated $NaCrO_2$ (50μA cm^{-2}, 30°C).

of SE to 15 *wt*% also resulted in a high capacity value of 104 mA h g^{-1}. The Nyquist plots in Figure 46 show that the amplitude of the semicircle for the mixture electrode, which corresponds to the charge transfer resistance at the SE–NCO interface,[76] is huge (~30 kΩ) in contrast to ~0.6 kΩ for the coated electrode.

Considering the one order of magnitude higher conductivity of Na_3SbS_4 (1.1×10^{-3} S cm^{-1}) used in the mixture electrode than NSbS-M200 (1.1×10^{-3} S cm^{-1}) for the SE-coated electrode, it is striking that the SE-coated NCO electrode outperforms the mixture electrode dramatically. This result is in line with previous result of $0.4LiI\cdot0.6Li_4SnS_4$-coated $LiCoO_2$ for all-solid-state lithium-ion batteries. The electrode from $LiCoO_2$ coated by $0.4LiI\cdot0.6Li_4SnS_4$ (4.1×10^{-4} S cm^{-1}) outperformed the mixture electrodes employing not only the same SE ($0.4LiI\cdot0.6Li_4SnS_4$) but also $Li_{10}GeP_2S_{12}$ showing much higher conductivity (6.0×10^{-3} S cm^{-1}). Voltage profiles for the conventional mixture electrode using NPS showing the same conductivity (1.1×10^{-4} S cm^{-1}) as the solution-processed Na_3SbS_4 (NSbS-M200) were also compared (Figure 47b). The NPS mixture electrode exhibits much higher overpotential and a correspondingly lower capacity (94 mA h g^{-1}) than the Na_3SbS_4-coated electrode. In order to clarify the origin for the dramatic improvement for the coated electrodes as compared to the mixture electrodes, electron microscopy analysis on composite structures was carried out. The field emission scanning electron microscopy (FESEM) images and their corresponding EDXS elemental maps for the electrode surfaces (Figure 48) and cross-sections (Figure 49) are compared between the Na_3SbS_4-coated

NCO electrode and the mixture electrode. First, a much more uniform spatial distribution

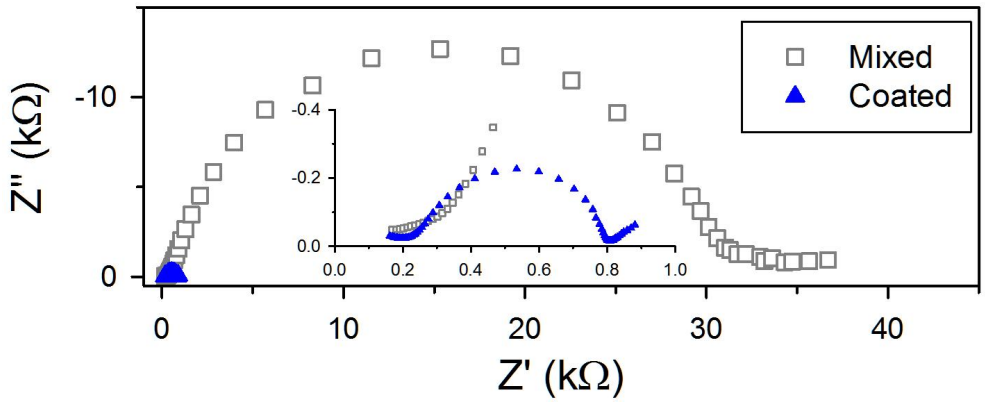

Figure 46. Nyquist plots of $NaCrO_2$/Na-Sn all-solid-state cells. The Na_3SbS_4-mixed and coated $NaCrO_2$ were compared.

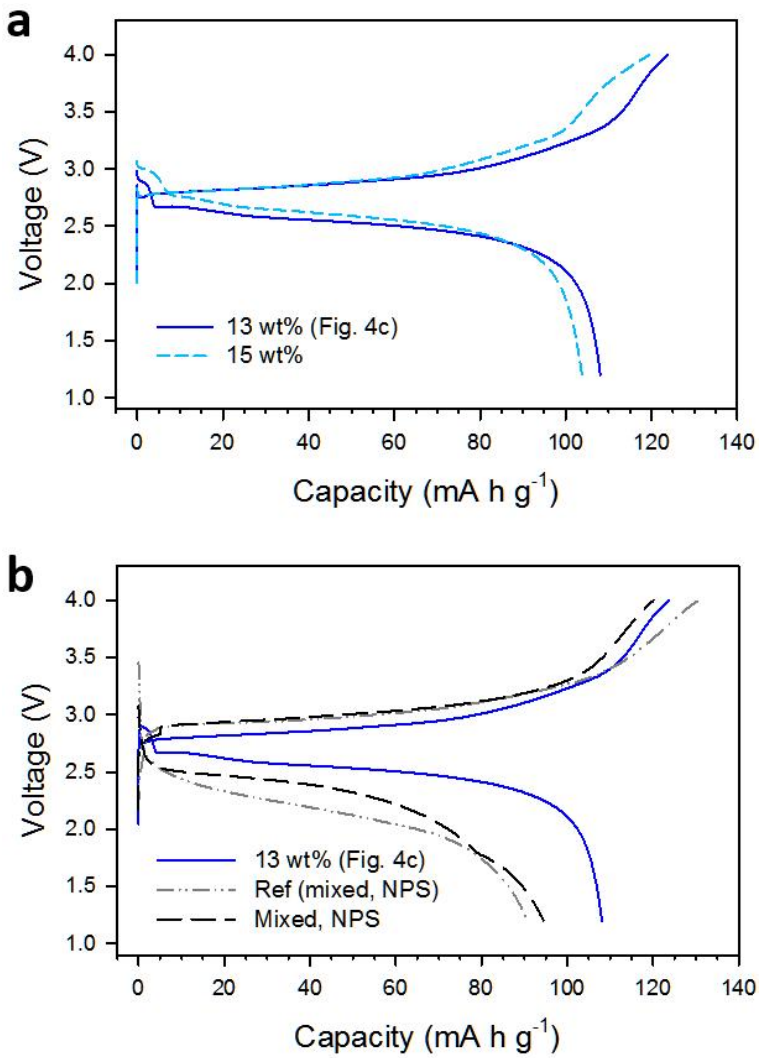

Figure 47. Initial voltage profiles of NCO/Na-Sn all-solid-state cells. a) Initial voltage profiles of NPS/NCO mixture electrodes. The NCO/NPS mixture electrode ('long dashed') consist of NCO:NPS:C with 80:20:1 weight ratio. The result from [49] is also compared. Note that the conductivity of NPS used in [49] was higher (0.46 mS cm^{-1} *vs*. 0.11 mS cm^{-1}), the higher weight fraction of NPS (The NCO:NPS:C=4:6:1 weight ratio, 55*wt*% *vs*. 20*wt*%) was used, and the lower current density of 13 μA cm^{-2} (*vs*. 50 μA cm^{-2} in this work) was applied.

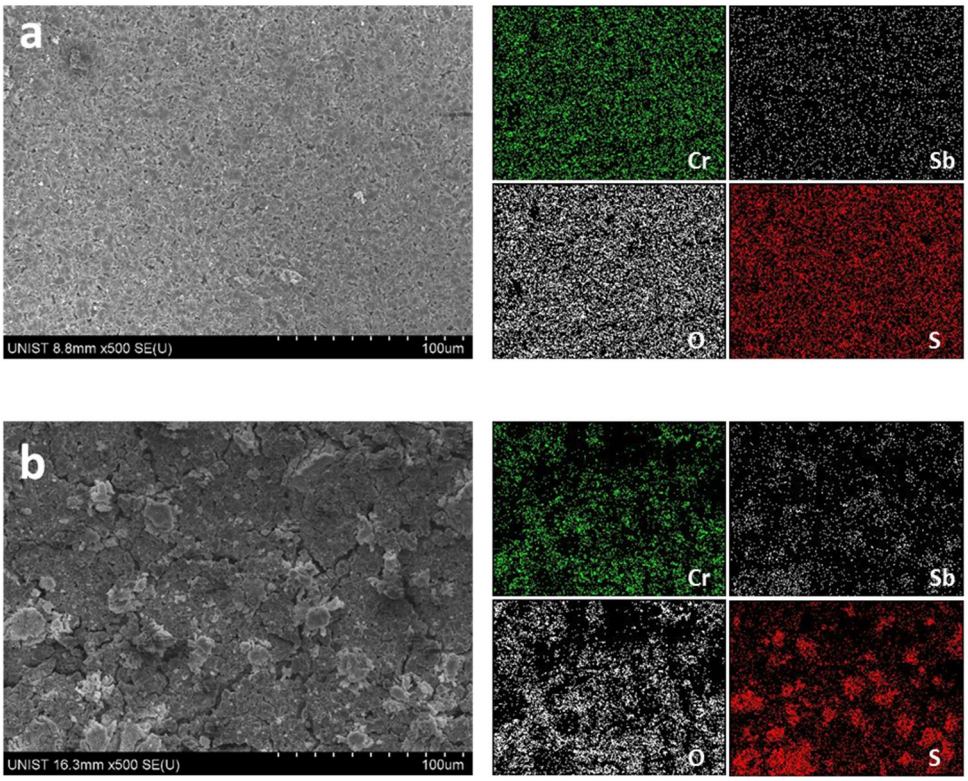

Figure 48. FESEM image of a) Na_3SbS_4-coated NCO electrode and b) Na_3SbS_4/NCO mixture electrode.

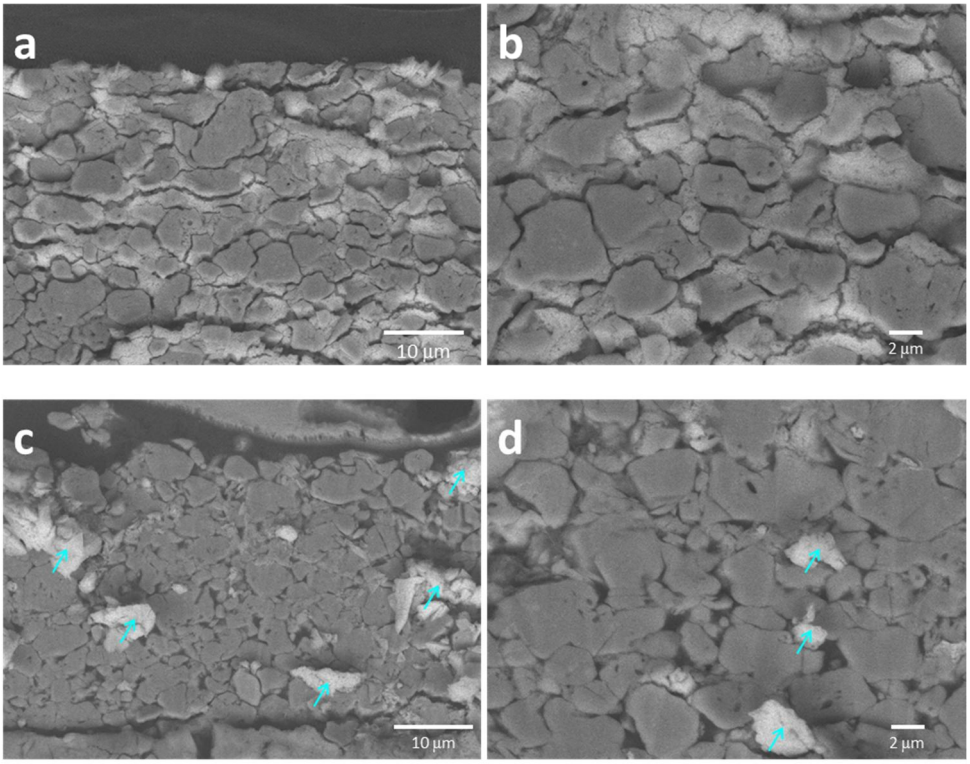

Figure 49. Cross-sectional FESEM image of a, b) the Na_3SbS_4-coated electrodes and c, d) the mixture electrodes. The arrow in c, d indicate SE, Na_3SbS_4.

of SEs and active materials for the coated electrode than for the mixture electrode is confirmed. Second, for the coated electrode, the SEs fills the voids between the NCO particles to form intimate contacts. In stark contrast, many voids between the NCO particles with the segregated SE regions are evident for the mixture electrode. These observations imply far superior ionic conduction and ionic contacts in the SE-coated electrode to in the mixture electrode, thus explaining the significantly improved electrochemical performances. Overall, all the results demonstrate the exceptional advantage of solution-processable SE, Na_3SbS_4, to satisfy the challenging requirements for all-solid-state batteries, intimate ionic contact and uniform spatial distribution of SEs.

Unfortunately, the NCO/Na-Sn all-solid-state cell using Na_3SbS_4-coated NCO showed gradual capacity fading upon repeated cycling (Figure 50), which could be explained by poor electrochemical stability of sulfide SEs,[33,76] chemical reaction between NCO and Na_3SbS_4,[10] space charge layer model,[134] and lattice mismatch.[134] It should be noted that the results in this work were obtained by using NCO powders without any protective coatings. Further improvements of the electrochemical performances could be possible by protective coating on cathode material as demonstrated well for surface-modified $LiCoO_2$ in all-solid-state lithium-ion batteries.[6,18,33,38]

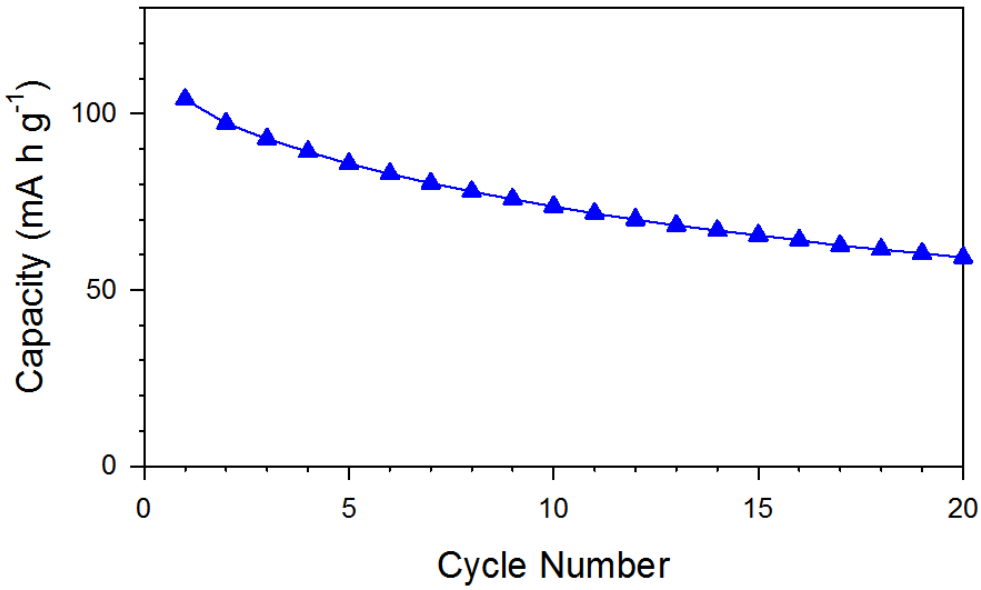

Figure 50. Cycling performance of NCO/Na-Sn employing Na_3SbS_4-coated NCO electrode at 50 μA cm^{-2} in the voltage range of 1.2-3.7 V at 30°C.

5. CONCLUSION

This research successfully demonstrated the application of a new, highly conductive, highly deformable, and dry-air-stable glass $0.4LiI\text{-}0.6Li_4SnS_4$ prepared at 200°C from a homogeneous MeOH solution for the scalable solution coating with intimate ionic contacts. The combined spectroscopic and electrochemical analyses revealed the importance of the microstructure and the inclusion of LiI on the properties of SEs (conductivity and deformability). Importantly, the comprehensive electron microscopy and electrochemical analyses revealed the significant impact of intimate ionic contacts between the active materials and SEs for the $0.4LiI\text{-}0.6Li_4SnS_4$-coated $LiCoO_2$ electrodes, as compared to the conventional mixture electrodes. The excellent capacity retention of the $0.4LiI\text{-}0.6Li_4SnS_4$-coated $LiCoO_2$ electrode upon exposure to dry air is also very promising for ASLB applications. It should be emphasized that this solution-processable $LiI\text{-}Li_4SnS_4$ unprecedentedly satisfies both high performance and high potential for practical applications. In other hand, a high conductivity of 1.1×10^{-3} S cm^{-1}, good dry-air stability, and scalable solution-processability using MeOH or water was successfully demonstrated for a new Na superionic conductor, tetragonal Na_3SbS_4. The structural refinement revealed 3D Na-ion diffusion channels, with the preference in 2D diffusion in the a–b plane. Finally, the high conductivity (1.1×10^{-4} S cm^{-1}), the intimate ionic contact with the active material, and well-percolated SEs, enabled by the solution-processed Na_3SbS_4, resulted in the dramatically improved electrochemical performance of NCO/Na-Sn ASNBs. I believe that these results will ignite interest in

materials design and synthesis for superionic conductors and advance all-solid-state technologies for commercialization.

REFERENCES

[1] Agura, T. and Tozawa, K., *Prog. Batt. Solar Cells,* **9**, 209-217 (1990)
[2] Goodenough, J. B. and Kim, Y., *Chem. Mater.,* **22**, 587-603 (2010)
[3] Tarascon, J.-M., *Phil. Trans. R. Soc. A,* **368**, 3227-3241 (2010)
[4] Whittingham, M. S., *Chem. Rev.,* **104**, 4271-4301 (2004)
[5] Xu, K., *Chemical Reviews,* **104**, 4303-4418 (2004)
[6] Kamaya, N., Homma, K., Yamakawa, Y., Hirayama, M., Kanno, R., Yonemura, M., Kamiyama, T., Kato, Y., Hama, S., Kawamoto, K. and Mitsui, A., *Nat. Mater.,* **10**, 682-686 (2011)
[7] Hayashi, A., Noi, K., Sakuda, A. and Tatsumisago, M., *Nat. Commun.,* **3**, 856 (2012)
[8] Adachi, G. Y., Imanaka, N. and Aono, H., *Adv. Mater.,* **8**, 127-135 (1996)
[9] Seino, Y., Ota, T., Takada, K., Hayashi, A. and Tatsumisago, M., *Energy Environ. Sci.,* **7**, 627-631 (2014)
[10] Sakuda, A., Hayashi, A. and Tatsumisago, M., *Chem. Mater.,* **22**, 949-956 (2010)
[11] Nagao, M., Kitaura, H., Hayashi, A. and Tatsumisago, M., *J. Power Sources,* **189**, 672-675 (2009)
[12] Nagao, M., Kitaura, H., Hayashi, A. and Tatsumisago, M., *J. Electrochem. Soc.,* **160**, A819-A823 (2013)
[13] Abe, T., Fukuda, H., Iriyama, Y. and Ogumi, Z., *J. Electrochem. Soc.,* **151**, A1120-A1123 (2004)
[14] Chiku, M., Tsujiwaki, W., Higuchi, E. and Inoue, H., *Electrochemistry,* **80**, 740-742 (2012)
[15] Wang, B., Bates, J. B., Hart, F. X., Sales, B. C., Zuhr, R. A. and Robertson, J. D., *J. Electrochem. Soc.,* **143**, 3203-3213 (1996)
[16] Bates, J. B., Dudney, N. J., Neudecker, B., Ueda, A. and Evans, C. D., *Solid State Ionics,* **135**, 33-45 (2000)
[17] Patil, A., Patil, V., Shin, D. W., Choi, J.-W., Paik, D.-S. and Yoon, S.-J., *Mat. Res. Bull.,* **43**, 1913-1942 (2008)
[18] Sakuda, A., Hayashi, A. and Tatsumisago, M., *Sci. Reports,* **3**, 2261 (2013)
[19] Kanno, R. and Murayama, M., *J. Electrochem. Soc.,* **148**, A742-A746 (2001)
[20] Mizuno, F., Hayashi, A., Tadanaga, K. and Tatsumisago, M., *Adv. Mater.,* **17**, 918-921 (2005)
[21] Lapp, T., Skaarup, S. and Hooper, A., *Solid State Ionics,* **11**, 97-103 (1983)
[22] Sahu, G., Lin, Z., Li, J., Liu, Z., Dudney, N. and Liang, C., *Energy Environ. Sci.,* **7**, 1053-1058 (2014)
[23] Knauth, P., *Solid State Ionics,* **180**, 911-916 (2009)
[24] Stramare, S., Thangadurai, V. and Weppner, W., *Chem. Mater.,* **15**, 3974-3990 (2003)
[25] Aono, H. and Sugimoto, E., *J. Electrochem. Soc.,* **136**, 590-591 (1989)
[26] Murugan, R., Thangadurai, V. and Weppner, W., *Angew. Chem. Int. Ed.,* **46**, 7778-

7781 (2007)
[27] Kotobuki, M., Munakata, H., Kanamura, K., Sato, Y. and Yoshida, T., *J. Electrochem. Soc.,* **157**, A1076-A1079 (2010)
[28] Kim, K. H., Iriyama, Y., Yamamoto, K., Kumazaki, S., Asaka, T., Tanabe, K., Fisher, C. A. J., Hirayama, T., Murugan, R. and Ogumi, Z., *J. Power Sources,* **196**, 764-767 (2011)
[29] Aboulaich, A., Bouchet, R., Delaizir, G., Seznec, V., Tortet, L., Morcrette, M., Rozier, P., Tarascon, J.-M. and Viallet, V., *Adv. Energy Mater.,* **1**, 179-183 (2011)
[30] Ohta, S., Seki, J., Yagi, Y., Kihira, Y., Tani, T. and Asoka, T., *J. Power Sources,* **265**, 40-44 (2014)
[31] Deiseroth, H.-J., Kong, S.-T., Eckert, H., Vannahme, J., Reiner, C., Zaiss, T. and Schlosser, M., *Angew. Chem. Int. Ed.,* **47**, 755-758 (2008)
[32] Maier, J., *Nature Materials,* **4**, 805-815 (2005)
[33] Jung, Y. S., Oh, D. Y., Nam, Y. J. and Park, K. H., *Israel Journal of Chemistry,* **55**, 472-485 (2015)
[34] Kitaura, H., Hayashi, A., Tadanaga, K. and Tatsumisago, M., *J. Electrochem. Soc.,* **156**, A114-A119 (2009)
[35] Oh, D. Y., Nam, Y. J., Park, K. H., Jung, S. H., Cho, S. J., Kim, Y. K., Lee, Y. G., Lee, S. Y. and Jung, Y. S., *Advanced Energy Materials,* **5**, 7 (2015)
[36] Ohta, N., Takada, K., Zhang, L., Ma, R., Osada, M. and Sasaki, T., *Adv. Mater.,* **18**, 2226-2229 (2006)
[37] Sakuda, A., Hayashi, A., Ohtomo, T., Hama, S. and Tatsumisago, M., *Electrochem. Solid-State Lett.,* **13**, A73-A75 (2010)
[38] Nam, Y. J., Cho, S. J., Oh, D. Y., Lim, J. M., Kim, S. Y., Song, J. H., Lee, Y. G., Lee, S. Y. and Jung, Y. S., *Nano Letters,* **15**, 3317-3323 (2015)
[39] Wang, Y., Liu, Z., Zhu, X., Tang, Y. and Huang, F., *J. Power Sources,* **224**, 225-229 (2013)
[40] Liu, Z., Fu, W., Payzant, E. A., Yu, X., Wu, Z., Dudney, N. J., Kiggans, J., Hong, K., Rondinone, A. J. and Liang, C., *J. Am. Chem. Soc.,* **135**, 975-978 (2013)
[41] Rangasamy, E., Liu, Z. C., Gobet, M., Pilar, K., Sahu, G., Zhou, W., Wu, H., Greenbaum, S. and Liang, C. D., *Journal of the American Chemical Society,* **137**, 1384-1387 (2015)
[42] Teragawa, S., Aso, K., Tadanaga, K., Hayashi, A. and Tatsumisago, M., *J. Power Sources,* **248**, 939-942 (2014)
[43] Yubuchi, S., Teragawa, S., Aso, K., Tadanaga, K., Hayashi, A. and Tatsumisago, M., *Journal of Power Sources,* **293**, 941-945 (2015)
[44] Kaib, T., Haddadpour, S., Kapitein, M., Bron, P., Schroeder, C., Eckert, H., Roling, B. and Dehnen, S., *Chem. Mater.,* **24**, 2211-2219 (2012)
[45] Muramatsu, H., Hayashi, A., Ohtomo, T., Hama, S. and Tatsumisago, M., *Solid State Ionics,* **182**, 116-119 (2011)
[46] Dunn, B., Kamath, H. and Tarascon, J. M., *Science,* **334**, 928-935 (2011)
[47] Hong, S. Y., Kim, Y., Park, Y., Choi, A., Choi, N.-S. and Lee, K. T., *Energy Environ. Sci.,* **6**, 2067-2081 (2013)

[48] Yabuuchi, N., Kubota, K., Dahbi, M. and Komaba, S., *Chemical Reviews,* **114**, 11636-11682 (2014)
[49] Hayashi, A., Noi, K., Tanibata, N., Nagao, M. and Tatsumisago, M., *J. Power Sources,* **258**, 420-423 (2014)
[50] Tanibata, N., Noi, K., Hayashi, A. and Tatsumisago, M., *Rsc Advances,* **4**, 17120-17123 (2014)
[51] Zhang, L., Yang, K., Mi, J. L., Lu, L., Zhao, L. R., Wang, L. M., Li, Y. M. and Zeng, H., *Advanced Energy Materials,* **5**, 5 (2015)
[52] Bo, S. H., Wang, Y., Kim, J. C., Richards, W. D. and Ceder, G., *Chemistry of Materials,* **28**, 252-258 (2016)
[53] Richards, W. D., Tsujimura, T., Miara, L. J., Wang, Y., Kim, J. C., Ong, S. P., Uechi, I., Suzuki, N. and Ceder, G., *Nature Communications,* **7**, 8 (2016)
[54] Mo, Y., Ong, S. P. and Ceder, G., *Chem. Mater.,* **24**, 15-17 (2012)
[55] Kuhn, A., Koehler, J. and Lotsch, B. V., *Phys. Chem. Chem. Phys.,* **15**, 11620-11622 (2013)
[56] Ong, S. P., Mo, Y., Richards, W. D., Miara, L., Lee, H. S. and Ceder, G., *Energy Environ. Sci.,* **6**, 148-156 (2013)
[57] Bron, P., Johansson, S., Zick, K., auf der Guenne, J. S., Dehnen, S. and Roling, B., *J. Am. Chem. Soc.,* **135**, 15694-15697 (2013)
[58] Hayashi, A., Hama, S., Minami, T. and Tatsumisago, M., *Electrochem. Commun.,* **5**, 111-114 (2003)
[59] Tatsumisago, M., Mizuno, F. and Hayashi, A., *J. Power Sources,* **159**, 193-199 (2006)
[60] Mizuno, F., Hayashi, A., Tadanaga, K. and Tatsumisago, M., *Solid State Ionics,* **177**, 2721-2725 (2006)
[61] Minami, K., Mizuno, F., Hayashi, A. and Tatsumisago, M., *Solid State Ionics,* **178**, 837-841 (2007)
[62] Hayashi, A., Minami, K., Ujiie, S. and Tatsumisago, M., *J. Non-Cryst. Solids,* **356**, 2670-2673 (2010)
[63] Kowada, Y., Tatsumisago, M., Minami, T. and Adachi, H., *J. Non-Cryst. Solids,* **354**, 360-364 (2008)
[64] Mizuno, F., Hayashi, A., Tadanaga, K. and Tatsumisago, M., *Solid State Ionics,* **177**, 2731-2735 (2006)
[65] Minami, K., Hayashi, A. and Tatsumisago, M., *J. Non-Cryst. Solids,* **356**, 2666-2669 (2010)
[66] Boulineau, S., Courty, M., Tarascon, J.-M. and Viallet, V., *Solid State Ionics,* **221**, 1-5 (2012)
[67] Boulineau, S., Tarascon, J.-M., Leriche, J.-B. and Viallet, V., *Solid State Ionics,* **242**, 45-48 (2013)
[68] Zhang, Z. M. and Kennedy, J. H., *Solid State Ionics,* **38**, 217-224 (1990)
[69] Sakamoto, R., Tatsumisago, M. and Minami, T., *J. Phys. Chem. B,* **103**, 4029-4031 (1999)
[70] Mercier, R., Malugani, J. P., Fahys, B. and Robert, G., *Solid State Ionics,* **5**, 663-

666 (1981)
[71] Kennedy, J. H. and Zhang, Z., *J. Electrochem. Soc.,* **135**, 859-862 (1988)
[72] Kennedy, J. H. and Zhang, Z., *solid State Ionics,* **28**, 726-728 (1988)
[73] Minami, T., Hayashi, A. and Tatsumisago, M., *solid State Ionics,* **177**, 2715-2720 (2006)
[74] Ribes, M., Barrau, B. and Souquet, J. L., *J. Non-Cryst. Solids,* **38-9**, 271-276 (1980)
[75] Wada, H., Menetrier, M., Levasseur, A. and Hagenmuller, P., *Mat. Res. Bull.,* **18**, 189-193 (1983)
[76] Shin, B. R., Nam, Y. J., Oh, D. Y., Kim, D. H., Kim, J. W. and Jung, Y. S., *Electrochim. Acta,* **146**, 395-402 (2014)
[77] Shin, B. R. and Jung, Y. S., *J. Electrochem. Soc.,* **161**, A154-A159 (2014)
[78] Sakuda, A., Kitaura, H., Hayashi, A., Tadanaga, K. and Tatsumisago, M., *J. Electrochem. Soc.,* **156**, A27-A32 (2009)
[79] Trevey, J. E., Jung, Y. S. and Lee, S.-H., *Electrochim. Acta,* **56**, 4243-4247 (2011)
[80] Murphy, D. W., Carides, J. N., Salvo, F. J. D., Cros, C. and Waszczak, J. V., *Mat. Res. Bull.,* **12**, 825-830 (1977)
[81] Kim, Y. and Goodenough, J. B., *Electrochem. Solid-State Lett.,* **12**, A73-A75 (2009)
[82] Girishkumar, G., McCloskey, B., Luntz, A. C., Swanson, S. and Wilcke, W., *J. Phys. Chem. Lett.,* **1**, 2193-2203 (2010)
[83] Ji, X. L., Lee, K. T. and Nazar, L. F., *Nat. Mater.,* **8**, 500-506 (2009)
[84] Aurbach, D., Zinigrad, E., Cohen, Y. and Teller, H., *Solid State Ionics,* **148**, 405-416 (2002)
[85] Nagao, M., Hayashi, A., Tatsumisago, M., Kanetsuku, T., Tsuda, T. and Kuwabata, S., *Phys. Chem. Chem. Phys.,* **15**, 18600-18606 (2013)
[86] Nagao, M., Hayashi, A. and Tatsumisago, M., *Electrochemistry,* **80**, 734-736 (2012)
[87] Ohtomo, T., Hayashi, A., Tatsumisago, M. and Kawamoto, K., *Electrochemistry,* **81**, 428-431 (2013)
[88] Okada, K., Machida, N., Naito, M., Shigematsu, T., Ito, S., Fujiki, S., Nakano, M. and Aihara, Y., *Solid State Ionics,* **255**, 120-127 (2014)
[89] Kitaura, H., Hayashi, A., Tadanaga, K. and Tatsumisago, M., *Electrochim. Acta,* **55**, 8821-8828 (2010)
[90] Mizuno, F., Hayashi, A., Tadanaga, K., Minami, T. and Tatsumisago, M., *J. Power Sources,* **124**, 170-173 (2003)
[91] Machida, N., Maeda, H., Peng, H. and Shigematsu, T., *J. Electrochem. Soc.,* **149**, A688-A693 (2002)
[92] Takada, K., Ohta, N., Zhang, L., Xu, X., Bui Thi, H., Ohnishi, T., Osada, M. and Sasaki, T., *Solid State Ionics,* **225**, 594-597 (2012)
[93] Mizuno, F., Hayashi, A., Tadanaga, K., Minami, T. and Tatsumisago, M., *Solid State Ionics,* **175**, 699-702 (2004)
[94] Jung, Y. S., Cavanagh, A. S., Dillon, A. C., Groner, M. D., George, S. M. and Lee,

S. H., *J. Electrochem. Soc.,* **157**, A75-A81 (2010)
[95] Jung, Y. S., Cavanagh, A. S., Riley, L. A., Kang, S. H., Dillon, A. C., Groner, M. D., George, S. M. and Lee, S. H., *Adv. Mater.,* **22**, 2172-2176 (2010)
[96] Jung, Y. S., Lu, P., Cavanagh, A. S., Ban, C., Kim, G. H., Lee, S. H., George, S. M., Harris, S. J. and Dillon, A. C., *Adv. Energy Mater.,* **3**, 213-219 (2013)
[97] Ohta, N., Takada, K., Sakaguchi, I., Zhang, L., Ma, R., Fukuda, K., Osada, M. and Sasaki, T., *Electrochem. Commun.,* **9**, 1486-1490 (2007)
[98] Woo, J. H., Trevey, J. E., Cavanagh, A. S., Choi, Y. S., Kim, S. C., George, S. M., Oh, K. H. and Lee, S.-H., *J. Electrochem. Soc.,* **159**, A1120-A1124 (2012)
[99] Yada, C., Ohmori, A., Ide, K., Yamasaki, H., Kato, T., Saito, T., Sagane, F. and Iriyama, Y., *Adv. Energy Mater.,* doi: 10.1002/aenm.201301416 (2014)
[100] Takada, K., *Langmuir,* **29**, 7538-7541 (2013)
[101] Takada, K., Ohta, N., Zhang, L., Fukuda, K., Sakaguchi, I., Ma, R., Osada, M. and Sasaki, T., *Solid State Ionics,* **179**, 1333-1337 (2008)
[102] Sakuda, A., Nakamoto, N., Kitaura, H., Hayashi, A., Tadanaga, K. and Tatsumisago, M., *J. Mater. Chem.,* **22**, 15247-15254 (2012)
[103] Xu, X., Takada, K., Fukuda, K., Ohnishi, T., Akatsuka, K., Osada, M., Bui Thi, H., Kumagai, K., Sekiguchi, T. and Sasaki, T., *Energy Environ. Sci.,* **4**, 3509-3512 (2011)
[104] Whittingham, M. S., *Science,* **192**, 1126-1127 (1976)
[105] Shin, B. R., Nam, Y. J., Kim, J. W., Lee, Y.-G. and Jung, Y. S., *Sci. Reports,* **4**, 5572 (2014)
[106] Trevey, J. E., Stoldt, C. R. and Lee, S.-H., *J. Electrochem. Soc.,* **158**, A1282-A1289 (2011)
[107] Yersak, T. A., Trevey, J. E. and Lee, S. H., *J. Power Sources,* **196**, 9830-9834 (2011)
[108] Yersak, T. A., Yan, Y., Stoldt, C. and Lee, S.-H., *ECS Electrochem. Lett.,* **1**, A21-A23 (2012)
[109] Yersak, T. A., Macpherson, H. A., Kim, S. C., Le, V.-D., Kang, C. S., Son, S.-B., Kim, Y.-H., Trevey, J. E., Oh, K. H., Stoldt, C. and Lee, S.-H., *Adv. Energy Mater.,* **3**, 120-127 (2013)
[110] Kim, Y., Arumugam, N. and Goodenough, J. B., *Chem. Mater.,* **20**, 470-474 (2008)
[111] Sakuda, A., Taguchi, N., Takeuchi, T., Kobayashi, H., Sakaebe, H., Tatsumi, K. and Ogumi, Z., *Solid State Ionics,* **262**, 143-146 (2014)
[112] Hendrickson, J. R. and Bray, P. J., *Journal of Magnetic Resonance,* **9**, 341-357 (1973)
[113] Heitjans, P. and Indris, S., *Journal of Physics-Condensed Matter,* **15**, R1257-R1289 (2003)
[114] Deng, Y., Eames, C., Chotard, J. N., Lalere, F., Seznec, V., Emge, S., Pecher, O., Grey, C. P., Masquelier, C. and Islam, M. S., *Journal of the American Chemical Society,* **137**, 9136-9145 (2015)
[115] Saienga, J. and Martin, S. W., *Journal of Non-Crystalline Solids,* **354**, 1475-1486

(2008)
[116] Huheey, J. E. K., R.L. Keriter *Inorganic Chemistry: Principles of Structure and Reactivity, 4th ed.*, HarperCollins College Publishers, New Tork, USA (1993)
[117] Benedictus, R., Bottger, A. and Mittemeijer, E. J., *Physical Review B,* **54**, 9109-9125 (1996)
[118] Jung, Y. S., Lee, K. T., Ryu, J. H., Im, D. and Oh, S. M., *Journal of the Electrochemical Society,* **152**, A1452-A1457 (2005)
[119] Weppner, W. and Huggins, R. A., *Journal of the Electrochemical Society,* **124**, 1569-1578 (1977)
[120] Levi, M. D., Salitra, G., Markovsky, B., Teller, H., Aurbach, D., Heider, U. and Heider, L., *Journal of the Electrochemical Society,* **146**, 1279-1289 (1999)
[121] Inada, T., Kobayashi, T., Sonoyama, N., Yamada, A., Kondo, S., Nagao, M. and Kanno, R., *J. Power Sources,* **194**, 1085-1088 (2009)
[122] Ito, S., Fujiki, S., Yamada, T., Aihara, Y., Park, Y., Kim, T. Y., Baek, S.-W., Lee, J.-M., Doo, S. and Machida, N., *J. Power Sources,* **248**, 943-950 (2014)
[123] Zhao, J., Lu, Z. D., Liu, N. A., Lee, H. W., McDowell, M. T. and Cui, Y., *Nature Communications,* **5**, 8 (2014)
[124] Brant, J. A., Massi, D. M., Holzwarth, N. A. W., MacNeil, J. H., Douvalis, A. P., Bakas, T., Martin, S. W., Gross, M. D. and Aitken, J. A., *Chemistry of Materials,* **27**, 189-196 (2015)
[125] Han, F. D., Gao, T., Zhu, Y. J., Gaskell, K. J. and Wang, C. S., *Advanced Materials,* **27**, 3473-3483 (2015)
[126] Jansen, M. and Henseler, U., *Journal of Solid State Chemistry,* **99**, 110-119 (1992)
[127] Graf, H. A. and Schafer, H., *Zeitschrift Fur Anorganische Und Allgemeine Chemie,* **425**, 67-80 (1976)
[128] Mikenda, W. and Preisinger, A., *Spectrochimica Acta Part a-Molecular and Biomolecular Spectroscopy,* **36**, 365-370 (1980)
[129] Sale, M. and Avdeev, M., *Journal of Applied Crystallography,* **45**, 1054-1056 (2012)
[130] Bruce, P. G., *Solid State Electrochemistry*, Cambridge University Press, Cambridge (1995)
[131] Long, G. G. and Bowen, L. H., *Inorganic & Nuclear Chemistry Letters,* **6**, 837-& (1970)
[132] Juarez, B. H., Rubio, S., Sanchez-Dehesa, J. and Lopez, C., *Advanced Materials,* **14**, 1486-+ (2002)
[133] Yu, C. Y., Park, J. S., Jung, H. G., Chung, K. Y., Aurbach, D., Sun, Y. K. and Myung, S. T., *Energy & Environmental Science,* **8**, 2019-2026 (2015)
[134] Haruyama, J., Sodeyama, K., Han, L. Y., Takada, K. and Tateyama, Y., *Chemistry of Materials,* **26**, 4248-4255 (2014)

국문 초록

용액공정이 가능한 리튬 및 소듐 고체전해질을 이용한 전고체전지

박 건 호

서울대학교 대학원

화학생물공학부

황화물계 고체전해질을 사용하는 벌크형 전고체 전지는 기존의 리튬이차전지가 가지고 있는 안전성 문제를 해결할 수 있는 대안으로 기대되고 있다. 그러나 전고체 전지의 핵심이라 할 수 있는 고체전해질은 이온전도도, 대량 합성, 활물질과의 접촉문제, 공기와의 반응성 등 여러 측면에서 문제를 가지고 있다. 특히 고체전해질은 고체의 특성상, 활물질 사이의 접촉을 충분히 이루기 힘들기 때문에 전극내 이온전달이 어렵게 되고 결과적으로 전지 성능의 저하로 이어진다.본 연구에서는 용매공정이 가능한 고체전해질을 이용해 이 문제를 해결하고자 했다. 이를 위해 높은 이온전도도(4.1×10^{-4} S cm^{-1} at $30^{o}C$)를 가지는 $0.4LiI\text{-}0.6Li_4SnS_4$ 글래스를 개발하고 화학적, 전기화학적 성능을 분석했다. 크고 큰 분극도를 가질 수 있는 요오드 이온이 Li_4SnS_4 에서 리튬이온의 이동을 쉽게한다. 특히

고체전해질 용액을 이용해 활물질에 이온전도층을 균일하게 도입할 수 있었고 이를 통해 전고체 전지의 성능을 획기적으로 개선할 수 있었다.

한편 낮은 가격을 강점으로 가지는 나트륨이온전지가 널리 연구되고 있지만 전고체 나트륨 전지에 대한 연구는 아직 부족한 실정이다. 가장 큰 이유로는 나트륨 이온 전도체의 낮은 이온전도도를 들 수 있다. 이에 대한 해결책으로 Na_3SbS_4 를 합성하고 1.1×10^{-3} S cm^{-1} 의 높은 이온전도도를 가지는 것을 확인했다. 더 중요한 것은 물과 메탄올에 녹은 뒤에도 적당한 수준의 이온전도도를 유지할 수 있어 활물질에 이온전도성 코팅층을 도입하는데 이용할 수 있었다. 본 연구를 통해 전고체 전지의 전극내 이온전달경로 형성의 중요성을 확인하고 고성능 전고체 전지 개발에 다가갈 수 있을 것으로 생각한다.

키워드: 이온전도체, 전고체 전지, 고체전해질, 용매공정, 리튬 전지, 나트륨 전지

학 번: 2011-22916